TÉCNICO LISBOA

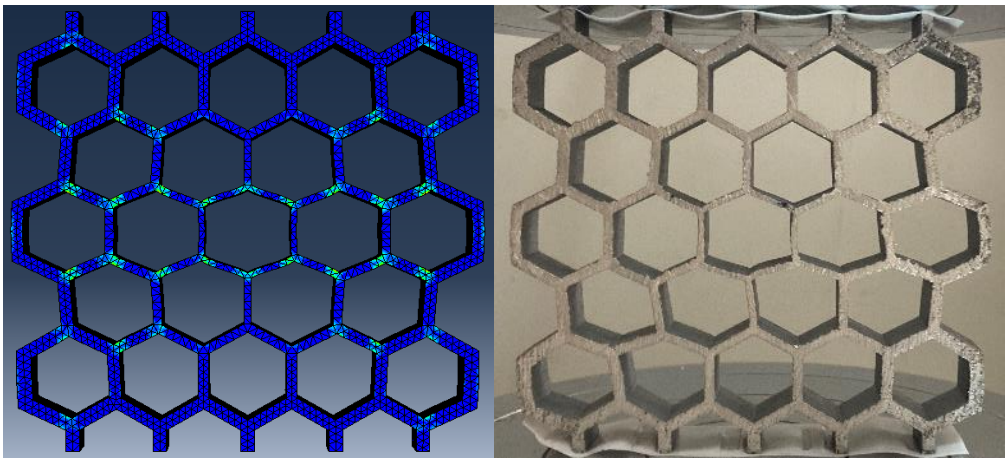

Modeling and Characterization of Honeycomb Structures with Density Gradient Produced by Additive Manufacturing Technologies

Bernardo Capelo Coelho

Thesis to obtain the Master of Science Degree in

Materials Engineering

Supervisors: Prof. Augusto Manuel Moura Moita de Deus

Prof. Maria de Fátima Reis Vaz

Examination Commitee

Chairperson: Prof. Alberto Eduardo Morão Cabral Ferro

Supervisor: Prof. Augusto Manuel Moura Moita de Deus

Member of the Committee: Prof. Maria Beatriz Cipriano de Jesus Silva

November 2022

Acknowledgments

Firstly, I would like to show my appreciation towards Professor Augusto Moita de Deus and Professor Maria Fátima Vaz, my supervisors in the present study. For the availability, guidance and advice in this last chapter on the path of becoming a fully fledged engineer, I am truly grateful, as I feel I am both a better professional and person after the last months.

Secondly, I would like to thank Instituto Superior Técnico and all its elements, which greatly influenced and allowed this project to flourish. I would also like to show my gratitude towards Professor Etienne Copin from IMT Mines Albi, for showing interest in the present project and being available to manufacture and send the graded aluminium specimens in such short notice.

I would like to leave a word of appreciation regarding Professor Maria Amélia Almeida and Professor José Carlos Pereira, not only for the concern and attention with which they approached every student while teaching, but for instilling important values that I still hold in high regard.

Last but not least, I wish to thank my family and friends for the unconditional support in this chapter of my life.

To my parents, thank you for being there every day and elevating me to my true potential, I could not have done it without you. To my sister, thank you for being my right hand and being a safe place in which I could always rest. To my grandparents, uncles and aunt, thank you for always being the pillars of my life.

To my friends, who have seen the worse and the best of me, thank you for the constant support. In my first home, Bruno, Barão, Guedes, David, Diogo, Mike, Suga, Pereira and Lima, please keep doing the okay job of being the family I chose. In my second home, I would like to start by leaving a special thank you to Froes, for accompanying me in the highest and the lowest points of the last five years. The next chapter awaits. To João, one of the truest and most dedicated friends I ever had, thank you. To the survivors and all the cool people I was lucky enough to meet during my higher education, which will remain anonymous, thank you. Lastly, to the ones which at some point were, but no longer are beside me, thank you for helping to soften the rocky path I had to walk to reach this conclusion.

Resumo

Muitos dos avanços tecnológicos surgiram na sequência duma observação atenta da natureza, sendo as estruturas celulares um claro exemplo disso. As estruturas favo-de-mel, subsecção das estruturas celulares, têm sido gradualmente implementadas em vários dos sectores industriais devido ao seu elevado rácio rigidez/peso e boas propriedades de absorção de energia, tornando-as alternativas eficientes relativamente a materiais maciços. Recentemente verificou-se um aumento no número de estudos relativos a estruturas favo-de-mel funcionais, incluindo com gradientes de densidade. O presente trabalho surge como uma investigação complementar relativamente a estas estruturas, sendo o seu principal objetivo a caracterização mecânica de estruturas favo-de-mel regulares e com gradiente de densidade. Amostras produzidas através de manufatura aditiva foram submetidas a ensaios experimentais de compressão, suplementarmente desenvolvendo um modelo computacional destes ensaios através do método dos elementos finitos (FEM). A rigidez e energia absorvida especificas foram analisadas, bem como a variação destas propriedades com a densidade relativa e área aparente.

De modo geral, as estruturas com gradiente demonstraram um desempenho mecânico superior comparativamente às estruturas regulares. Relativamente à orientação de carregamento fora-do-plano, as estruturas com gradiente apresentaram valores de rigidez superiores, sendo o principal fator de influência a área aparente. Relativamente à orientação dentro-do-plano, as estruturas com gradiente demonstraram valores de absorção de energia superiores aos das estruturas regulares, sendo a densidade relativa o elemento geométrico mais impactante. Os resultados numéricos dentro-do-plano demostraram uma correlação próxima relativamente aos resultados experimentais, com uma correspondência satisfatória referente à deformação permanente e subsequente fratura.

Palavras-chave: Materiais Celulares Funcionais; Estruturas Favo-de-mel; Método dos Elementos Finitos; Teste de Compressão; Manufatura Aditiva; Gradiente de Densidade.

Abstract

Many technological advances have come from a close observation of nature, with cellular structures being a clear example of this. Honeycomb structures, a subsection of cellular materials, have gradually been implemented in many industrial sectors, as the associated high stiffness-to-weight ratio and energy absorption properties make them efficient lightweight alternatives to bulk materials. As a response to recent demands, an increase in studies regarding functional materials has surfaced, namely with density gradients being the highlighted tailorability factor regarding honeycomb structures. The present work is therefore a complementary investigation regarding functionally graded cellular materials, with its main objective being the mechanical characterization of regular and density graded honeycomb structures. Physical samples obtained via additive manufacturing were experimentally submitted to compression testing, along with a computational model of the test being developed using the finite element method (FEM). Specific stiffness and absorbed energy were analysed, with the variation of these properties with relative density and apparent area also being recorded.

Overall, the functionally graded structures showed better mechanical performance when compared to their regular counterparts. In terms of out-of-plane testing, graded structures showed higher values for stiffness, with the main influence factor being the apparent area. In terms of in-plane testing, graded structures exhibited superior energy absorption than their regular counterparts, with relative density being the main driver. The in-plane numerical results showed an acceptable correlation with the experimental results, with satisfactory matching in plastic deformation and failure.

Keywords: Functionally Graded Cellular Structures; Honeycomb Structures; Finite Element Method; Compression Testing; Additive Manufacturing; Density Gradient.

List of Contents

List of Figures

List of Tables

Nomenclature

List of Variables

$\overline{\rho}$	Relative density
ρ^*	Density of cellular material
ρ_s	Density of solid material
V_s	Volume of solid material
V_T	Total volume
$\frac{V_s}{V_T}$	Volume fraction
m_s	Mass of solid material
A_s	Solid area
A_T	Total area/Apparent area
η	Porosity of a material
l	Cell length
t	Cell thickness
$\frac{t}{l}$	Thickness-to-length ratio
h	Core cell height
L_1	Length
H_1	Height
W_1	Width
x_i	Length from centre cell's most distant wall thickness to end of i cell
L^*	Length from centre cell's most distant wall thickness to side of structure
d_i	In-plane thickness of an i cell
G	Shear modulus

E	Young's modulus
E_1^*	Young's modulus parallel to X_1 direction
E_2^*	Young's modulus parallel to X_2 direction
E_3^*	Young's modulus parallel to X_3 direction
E_s	Young's modulus of the solid material
$\bar{E}$	Material's expected Young's modulus
σ^*	Plateau stress
σ_R	True stress
σ_N	Nominal stress
$\sigma_{y,N}$	Nominal yield stress
$\sigma_{U,N}$	Nominal ultimate strength
$\sigma_{T,R}$	True stress at breaking
$\sigma_{M,max}$	Maximum von Mises stress
ε_R	True strain
ε_N	Nominal strain
$\varepsilon_{T,N}$	Nominal elongation at break/Nominal total strain
$\varepsilon_{pl,R}$	True strain's plastic component
$\varepsilon_{el,R}$	True strain's elastic component
R	Gradient parameter
$\overline{\sigma}_{M,i}$	Average von Mises stress for mesh i
$\overline{\sigma}_{M,i-1}$	Average von Mises stress for mesh $i-1$
Ea	Absorbed energy
$\overline{Ea}$	Specific absorbed energy
K	Stiffness
$\overline{K}$	Specific stiffness

Variations

$l \approx$ L	Cell length
$h \approx$ H	Core cell height

List of units

ºC	Degrees Celsius
μm	Micrometre
mm	Millimetre
m/s	Metres per second
g/cm^3	Grams per cubic centimetre
N	Newton
kN	Kilonewton
MPa	Megapascal
GPa	Gigapascal
J	Joule
mJ	Millijoule

Glossary

2D	Bidimensional
3D	Tridimensional
AM	Additive Manufacturing
ASTM	American Society for Testing and Materials
CAD	Computer Aided Design
CS	Cellular Structures
CSV	Comma-Separated Values
DIN	Deutsches Institut für Normung (German Institute for Standardization)
EL	Elastic
EP	Elastoplastic
EXP	Experimental
FEA	Finite Element Analysis
FEM	Finite Element Method
FGCM	Functionally Graded Cellular Materials
FGM	Functionally Graded Materials
HOBE	Honeycomb Before Extrusion
IGS	Initial Graphics Exchange
SL	Stereolithography
SLM	Selective Laser Melting
NUM	Numerical
NUM_EL	Numerical Elastic
NUM_EP	Numerical Elastoplastic
TPU	Thermoplastic Polyurethane
UV	Ultraviolet

Chapter 1: Introduction

Mankind has taken inspiration from nature for centuries, with cellular materials being one of the many examples. In the case of cellular materials, honeycomb structures have been extensively studied, and adapted into a wide variety of structural applications due to their high stiffness-to-weight ratio and energy absorption, allowing the substitution of bulk materials for lighter structures, and consequent savings in both materials and weight, increasing both efficiency and profitability. Although honeycomb structures are mainly implemented as composite sandwich panel cores, making use of their high stiffness and strength in the out-of-plane orientation, there is a continuously expanding interest in the development of honeycomb structures with the intent of taking advantage of their in-plane mechanical properties, such as energy absorption.

The emergence of additive manufacturing techniques allowed for the production of more complex structures, and paved the way for the use of functionally graded structures for more specific applications. Some examples can be found in the biomedical industries with functionally graded structures imitating bone tissue [1] or in the aeronautical and defence engineering with radar absorbing functionally graded structures implemented in stealth aircrafts [2].

In terms of functionally graded honeycomb structures, the vast majority of studies have been associated to the tailorability of these structures in terms of energy absorption in high strain rate scenarios, like dynamic crushing and impact [3-5]. This tailorability revolves greatly around the implementation of density gradients, variating the structure's relative density along its dimensions, obtaining lighter functionally graded final parts with more appropriate energy absorption and stiffnesses when compared to their regular counterparts, concerning each particular application.

The present thesis aims at characterizing the out-of-plane and in-plane mechanical properties of regular and functionally graded aluminium honeycomb structures produced by additive manufacturing processes. This mechanical characterization is performed via the experimental compression testing of both regular and graded honeycomb structures, with the development of a Finite Element Method (FEM) model of the same compression testing apparatus to serve as prediction of the mechanical behaviour of the experimental samples. The failure mechanisms and fracture were also analysed to better understand the implications of additive manufacturing processes in the production of honeycomb structures. This study gives sequence to a previous Master of Science degree thesis by Tiago Rua [6], in which the presently tested regular and graded structures were designed and sequentially analysed regarding their out-of-plane numerical and experimental compression behaviour.

The primary objectives of the present study were defined as:

- Studying the influence of geometrical parameters in the out-of-plane and in-plane mechanical properties of regular and functionally graded honeycomb structures in compression testing.

- Comparing the mechanical performance of the functionally graded honeycomb structures with their regular counterparts.

- Confirming the accuracy of the developed computational model (FEM) regarding the physical testing of the samples, mainly through the results obtained for the mechanical properties and the predicted failure of the structures.

1.1 Thesis Outline

The present study is divided into five separate chapters:

- Chapter 1, the present chapter, in which an introduction to the study is presented, consisting of a brief outline of the background and objectives.

- Chapter 2, in which a description of the state-of-the-art concerning the topic of the work is presented.

- Chapter 3, in which the experimental work and the designed computational model are described, as well as any related calculations or specifications.

- Chapter 4, in which the obtained results are presented and discussed.

- Chapter 5, in which final conclusions regarding the obtained results are presented, as well as suggestions for future work.

Chapter 2: State of the art

2.1 Cellular materials

Cellular materials can be found in various forms throughout nature, as in wood or radiolarian shells, and have served as inspiration for countless technological advances [7], [8]. As defined by Gibson et al. [7], cellular materials consist in an arrangement of cells with solid faces/edges which occupy space. Bhate et al. [8] later added that these heterogeneous materials could be identified by the presence of a unit cell and the regular or irregular repetition of these unit cells.

As cellular materials started to progressively be more used and recognized by the scientific community, an effort to catalogue the different unit cells was performed. This effort culminated in the creation of three different levels in order to define unit cells: the division of space into repeating independent volumes (Tessellation), the shape of the material included in each independent volume (Elements) and the way in which each independent volume connects with its neighbours (Connectivity) [9], as shown in Figure 2.1.

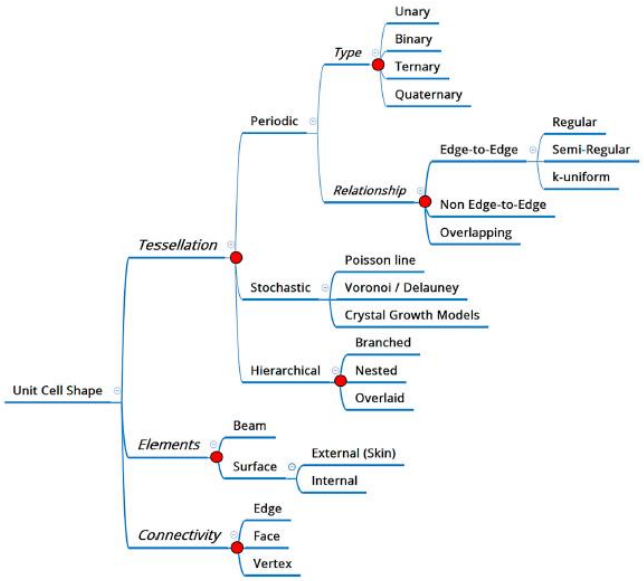

Figure 2.1: Classification of cellular materials unit cell based on three levels as proposed by Bhate [9]

Cellular materials can also be categorized into two-dimensional and three-dimensional [7], with the tessellation level allowing for the separation into more palpable categories:

- 2D **periodic** tessellation refers to the repetition of one or more polygonal shapes to fill a planar area, and the resulting geometries are named honeycombs (inspirated by beehive honeycombs). If the previous geometries are rotated 90º about their horizontal axis, they become prismatic, as observed in Figure 2.2 (a) and (b), respectively [7], [10].
- 3D **periodic** tessellation adds one domain of movement, with more complex geometries named lattice structures being attainable. Zhu et al. [11] join these various geometries into truss (different struts joined in nodal points) and textile (wires weaved into different layers), as demonstrated in Figure 2.2 (c).

- **Stochastic** tessellation refers to aperiodic cellular materials, commonly designated as foams, in which the shape and distribution of unit cells must be approximated statistically with random probability distributions, as demonstrated in Figure 2.2 (d) and (e) [12], [13].
- **Hierarchical** tessellation (Figure 2.2 (f)), as the name suggests, is based on a hierarchical development of unit cells. Commonly found in nature, they are not as present in engineering.

As a final means of categorizing, cellular materials can be classified as closed-cell or open-cell (with the possibility of creating a partially open and closed material [7]). The first one identifies cellular materials in which there is no direct connection between each individual cell space, creating an impermeable and non-porous structure. The latter identifies cellular materials in which exists a framework, with no solid material closing the cell spaces [14].

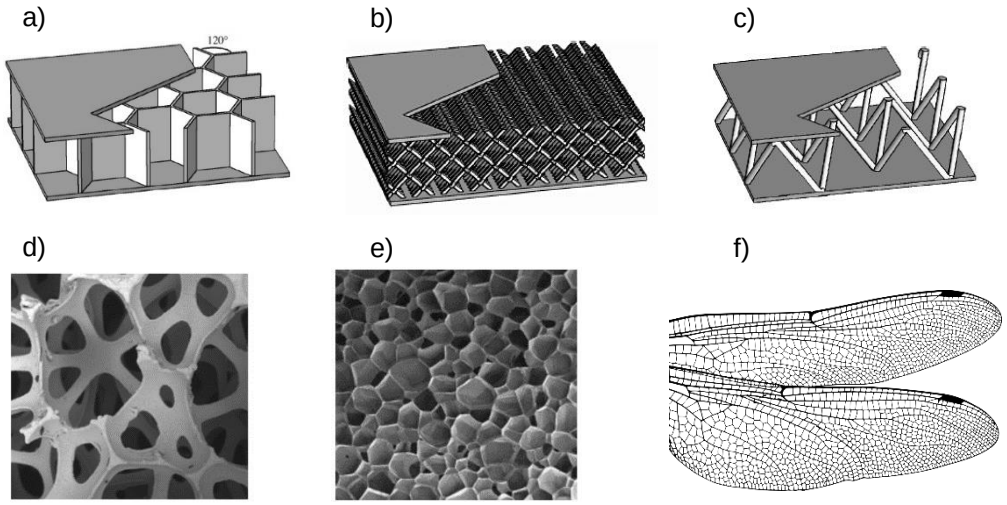

Figure 2.2: (a) Honeycomb core structure; (b) Prismatic geometry structure; (c) Lattice structure; (d) Open-cell foam; (e) Closed-cell foam; (f) Example of hierarchical tessellation in nature. Adapted from [10], [15], [16]

The main advantage of cellular materials is how it allows for higher structural efficiency, meaning they are capable of supporting the same load as their homogeneous counterparts with considerably less mass involved. The prospect of reliable results with reduced material and financial spending, paired with the possibility of locally controlling the cellular structure of component parts (adding multifunctionality), pushed the interest in this type of materials even further [17]. Through the fine-tuning of the cellular structure, a variety of benefits is obtainable for each multifunctional components (vibration and energy absorption, heat insulation, higher stiffness-to-weight ratio, among others) [18].

The multivalence of cellular structures, paired with the ongoing development in manufacturing processes (like additive manufacturing technologies), makes it possible to introduce cellular materials in most areas of use, varying from structural applications in the biomedical, automotive and aerospace industries, to functional applications (e.g., acoustic control, filtration, aid in catalytic activity) [19].

2.2 Honeycomb Structures

As the sole geometry studied in the present work, the hexagonal honeycomb will be discussed in greater detail.

As perceivable by its name, honeycomb structures are inspired by the bee's hexagonal honeycomb geometry, which has fascinated human minds as far as 2000 years ago [20]. It was remarkable how these insects would divide space into equal discrete sections, minimizing the use of wax in cell walls and maximizing the storage of honey. Influenced by this observation, a roman scholar named Marcus Terentius Varro firstly proposed the famous *Honeycomb Conjecture* (later confirmed by mathematician Thomas C. Hales), which states that "any partition of the plane into regions of equal area has perimeter at least that of the regular hexagonal honeycomb tiling" [21], [22]. This said, as illustrated in Figure 2.3, a hexagonal honeycomb structure is a 2D regular distribution of identical cells with hexagonal shape.

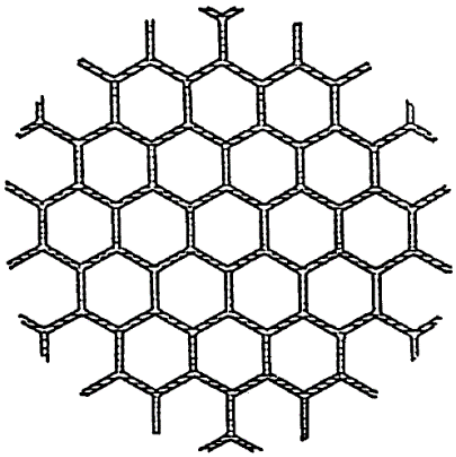

Figure 2.3: Typical regular hexagonal honeycomb structure [22]

Hexagonal honeycomb structures can presently be encountered in every class of materials [23], ranging from metals (as studied in the present work) to polymers, ceramics and composites (sandwich panels) [7], [24]. As other cellular solids, hexagonal honeycomb structures are preferably used in structural applications in which their structural efficiency can be exploited to the fullest, but new studies keep proving the existence of multifunctional applications [25]. For example, Sunami et al. [26] studied the use of microscopic hexagonal honeycomb films to enhance protein adsorption and mediate cellular growth, while Afzal et al. [27] implemented hexagonal honeycomb structures as part of a heat transfer enhancement network in a hydrogen storage system.

In order to characterize honeycomb structures and their mechanical behaviour, as performed in the present study, it is important to mention a particular set of properties:

- Relative density
- Mechanical Properties (both out-of-plane and in-plane), e.g. stiffness.

2.2.1 Relative Density

As described by Gibson and Ashby (1997) [7], the relative density ($\bar{\rho}$) of a cellular solid is its most significant property, being obtained by dividing the density of the cellular material (ρ^*) by the density of the material out of which the cell walls are composed of (ρ_s), and allowing for a better comparison between cellular solids of different porosities and structures. It is further stated by Gibson and Ashby [1] that the relative density can be translated into a volume fraction ($\frac{V_s}{V_T}$), where V_s stands for the volume of solid material and (V_T) for the total volume. This is demonstrated in Equation 2.1, in which m_s stands for the mass of the solid material:

$$\bar{\rho} = \frac{\rho^*}{\rho_s} = \frac{(m_s/V_T)}{(m_s/V_s)} = \frac{m_s}{V_T} \times \frac{V_s}{m_s} = \frac{V_s}{V_T} \tag{2.1}$$

As honeycomb structures are characterized as 2D structures, further simplification is possible. By eliminating the cellular structure's depth, a superficial geometry remains, as demonstrated previously in Figure 4. By doing this, the volume fraction is reduced to an area fraction (Equation 2.2), with A_s standing for the solid area and A_T, which is the total area or apparent area.

$$\bar{\rho} = \frac{\rho^*}{\rho_s} = \frac{V_s}{V_T} = \frac{A_s}{A_T} \tag{2.2}$$

The porosity of a solid material (η) is also obtainable through the relative density, with the volume fraction being complementary (difference to unity) to porosity. This said, materials are characterized as true cellular solids if $\bar{\rho} < 0.3$ or as a material containing isolated pores if $\bar{\rho} \geq 0.3$ [7].

2.2.2 Mechanical Properties

With relation to loading, the mechanical properties of hexagonal honeycomb structures can be divided into two planar orientations, as shown in Figure 2.4.

- In-plane, with loading being applied in the X_1-X_2 plane.
- Out-of-plane, with loading occurring along the X_3 direction.

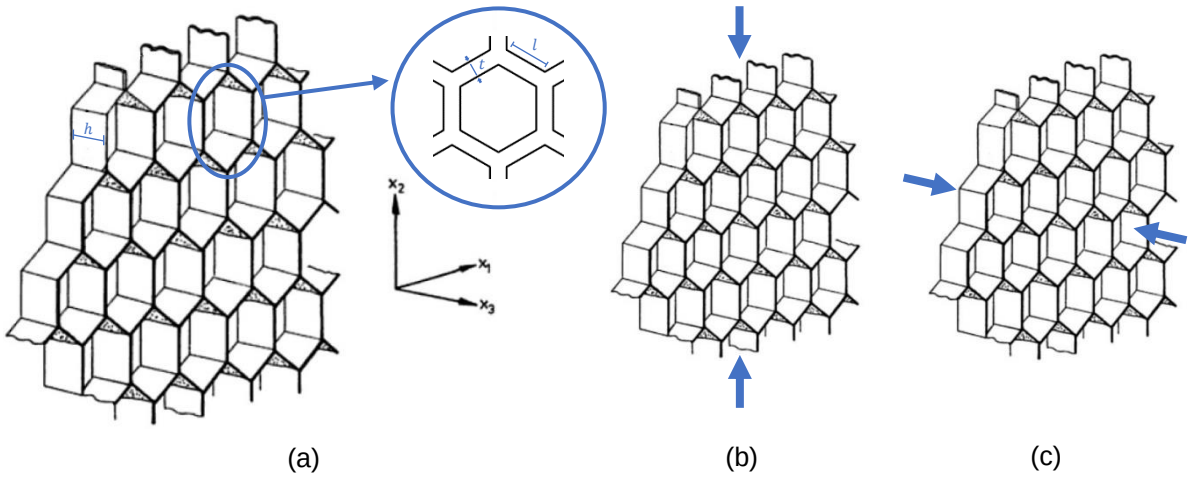

(a) (b) (c)

Figure 2.4: Schematic of a honeycomb structure with: (a) unit cell with geometric variables. h: core cell height; t: cell thickness; l: cell length; (b) in-plane and (c) out-of-plane loading orientations. Adapted from [7].

It is important to mention that the expressions for mechanical properties described below are under the assumption that all cell lengths (l) are equal, as well as having constant thickness (t) throughout the structure. Gibson and Ashby [7] derived that the thickness-to-length ratio ($\frac{t}{l}$) obtained using these two measurements was to some extent proportional to the relative density, and so a low relative density, and consequent $t \ll l$, is also assumed in order to simplify calculations. If all these criteria are met, then in-plane properties are isotropic. They are also relatively similar between different materials, with slight changes due to different deformation mechanisms [7].

If the structure is under compressive load, the stress-strain curve begins linearly, as the cell walls bend elastically. Cells then begin to collapse as a critical stress is reached, with the curve stabilizing at a plateau, as shown in Figure 2.5 (a-c). In elastomeric materials (a), the plateau stress is maintained due to elastic buckling of the cells; in elastoplastic materials (b), this behaviour is associated with the yielding of the cell's material, generating plastic hinges where bending is maximum (normally triple junctions), as seen in Figure 5 (h); in brittle materials (c), the plateau stress is prolonged due to the brittle fracture of cell walls. Finally, with the number of collapsed cells increasing considerably, stress values increase exponentially due to the compressing of the packed material in a step named *densification* [7].

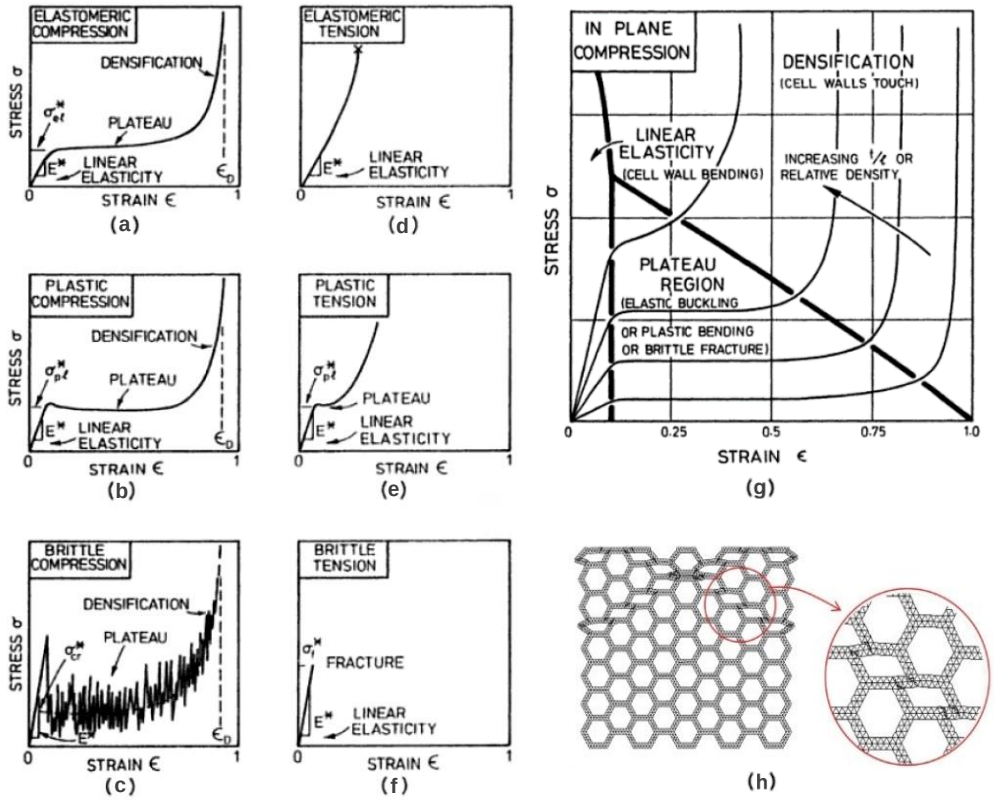

Figure 2.5: (a-c) Typical elastomeric, plastic and brittle compression stress-strain curves, respectively; (d-f) Typical elastomeric, plastic and brittle tensile compression stress-strain curves, respectively; (g) Effect of relative density in in-plane compression stress-strain curves; (h) Typical plastic hinge deformation. Adapted from [7], [28]

In the case of tensile loading, initial cell wall bending is translated into a linear elastic curve with identical slope as the elastic region in the compression curve. For elastomeric materials (d), cell walls will later rotate in the loading direction with increasing stiffness; elastoplastic honeycombs (e) will behave similarly as in compression, with a plateau stress being reached as plastic hinges begin to develop; finally, brittle honeycombs (f) fracture prematurely due to the propagation of defects [7].

Relative density influences the in-plane mechanical behaviour of honeycomb structures. An increase in relative density translates into a higher thickness-to-length ratio, meaning cell walls will withstand higher loads without collapsing, but also that *densification* will occur earlier due to the earlier contact between cell wall material. Ultimately, as seen in Figure 2.5 (g), higher Young's modulus and plateau stress are perceived, as well as *densification* occurring at lower strain values [7].

According to Gibson and Ashby [7], [29], regular honeycomb structures can be described elastically (in-plane) using the Young's modulus (E), the shear modulus (G) and a single value of plateau stress (σ^*). For the present work, only the Young's modulus is explored, which the mentioned authors describe as the geometrical relation between the cell wall thickness (t) and length (t) presented in Equation 2.3 (strictly for regular hexagonal geometries), with E_1^* and E_2^* being the Young's modulus parallel to the X_1 and X_2 directions, respectively, and E_s the Young's modulus of the solid material:

$$\frac{E_1^*}{E_s} = \frac{E_2^*}{E_s} = \frac{4}{\sqrt{3}} \frac{t^3}{l^3} \tag{2.3}$$

When loading occurs out-of-plane (along the X_3 direction), values for stiffness and strength are much higher than in in-plane, with the reason being the different deformation occurring in cell walls. While cell walls bend when loaded in the X_1-X_2 directions, they are extended or compressed along the cell axis (X_3) in out-of-plane deformation, meaning the loading bore by the structure and its collapse stresses are much higher [7].

Considering the same geometrical restrictions as before (constant l and t, with $t \ll l$), the behaviour under out-of-plane compressive load is similar to the in-plane. The stress-strain curve begins with an initial linear-elastic region, with much higher slope, until a plateau stress is reached as buckling begins to occur. Finally, as higher strains are reached, the cell walls fail by tearing or crushing. In tension, the stress-strain curve is mainly linear as the honeycomb deforms elastically until it fails. Examples for both curves are presented in Figure 2.6.

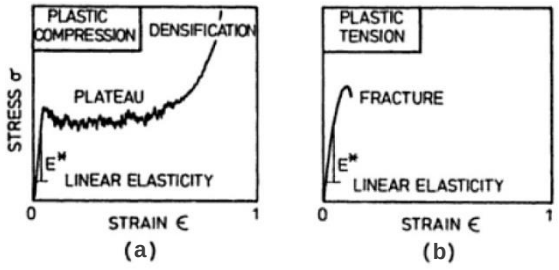

Figure 2.6: Typical in-plane (a) compression and (b) tensile stress-strain curves for honeycombs. Adapted from [7].

The Young's modulus for out-of-plane loading (E_3^*) is considerably easier to define, as deducted in Equation 2.4, acting as a representation of the solid surface section which supports the load [30].

$$\frac{E_3^*}{E_s} = \frac{\rho^*}{\rho_s} = \bar{\rho} \tag{2.4}$$

2.2.3 Manufacturing Methods

As mentioned before, the honeycomb structure has been observed and adapted to industrial applications for decades, with the first real design appearing in 1877, as F.H. Kustermann designed a moulding process through which paper honeycomb structures would be manufactured [31]. The concept of paper honeycomb structures would be further studied by H. Heilbrun, who invented the first expansion production process in 1901, followed a few years later with the first patent for the use of honeycomb structures as structural elements being issued to R. Hofler and S. Renyi [31]. World War II would serve as an unjust incentive for the development and use of honeycomb structures in aeronautical applications, with 1945 marking the year of the creation of the first aluminium honeycomb produced by adhesive bonding [20].

The manufacturing processes of honeycomb structures can, for the most part, be separated into *traditional* manufacturing processes and *novel* manufacturing processes, with the latter being mainly focused on additive manufacturing processes in the present work.

2.2.3.1 Traditional Manufacturing Processes

Traditional manufacturing processes are generally associated with the formation of stacks of sheet materials converted into a honeycomb structure, existing five basic methods of creating this stack: *adhesive bonding*, *resistance welding*, *brazing*, *diffusion bonding* and *thermal fusion* [20]. The majority of these stacked materials are produced via adhesive bonding, with nodes (contact points between sheets) withstanding temperatures up to 399 ºC, while resistance welding, brazing and diffusion bonding are used in situations in which nodes must withstand high temperatures or harsh environments. Finally, thermal fusion is used in polymer sheets in which nodes are heated and fused together [20], [31]. There are two main techniques to convert sheet materials into honeycomb structures: the *corrugation* and the *expansion* processes.

The c*orrugation* process is the original honeycomb production method, still used for structures with high relative density and difficult to attain through the expansion process. In this process, the sheet material is passed between corrugated rolls, assuming the corrugated shape shown in Figure 2.7, which is consequently stacked and joined through one of the previously mentioned methods. The stack is finally sliced to the desirable thickness, obtaining a honeycomb core [10].

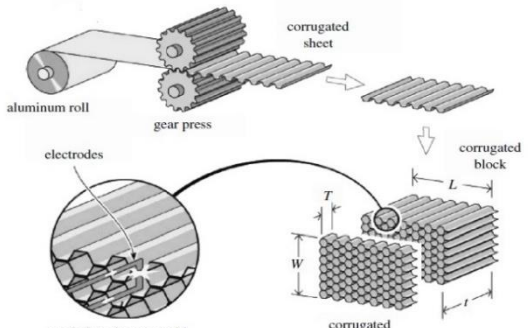

Figure 2.7: Schematics of the corrugation process for honeycomb production. Adapted from [10]

The *expansion* process is presently the most commonly used, as majority of adhesive bonded stacks are converted in honeycomb structures by expansion. It is also a process associated with structures with relatively low relative density, as thin sheets are cut and strip bonded in order to form an intermediate assembly named HOBE or “honeycomb before expansion”. The HOBE is then cut in the desired thickness and extended perpendicularly to the bonds, resulting in a hexagonal structure (Figure 2.8) [10]. This process is restricted to materials which support the plastic deformation associated to the expansion step, so brittle materials are mostly associated to the corrugation process.

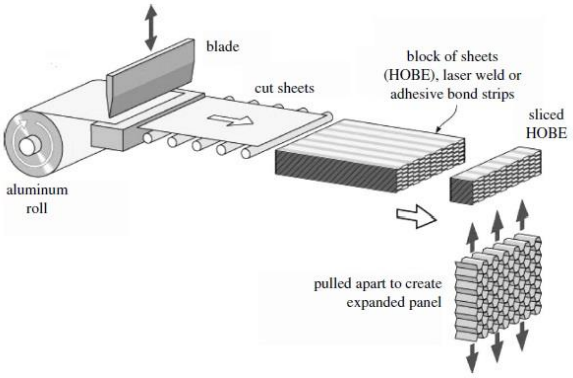

Figure 2.8: Schematics of the expansion process for honeycomb production Adapted from [10].

2.2.3.2 Novel Manufacturing Processes

As technology started corresponding to the progressive interest in honeycomb structures, more advanced manufacturing processes and variations of honeycombs started to emerge. New materials which could not be processed by the previously described methods, and irregular structures with added multifunctionality, pushed investigators to develop new manufacturing processes which could achieve a degree of adaptability to these recent restrictions.

Pflug et al. [32] proposed a continuous process of folding corrugated cardboard sheets into honeycomb structures, which allowed for much higher productivity and material savings in the production of honeycomb core sandwich parts. This project would later be extended to thermoplastic films, exploring its application in the automotive industry [33]. In recent years, Wang et al. [34] studied the adaptation of this continuous folding process to the production of aluminium honeycomb structures, creating a path for further introducing these structures in everyday uses.

Naplocha et al. [35] explored the use of investment casting in the design of aluminium honeycomb structures, which showed promising results in terms of stiffness, strength, and dimension and surface accuracy regarding the complex mould.

Tripathi et al. [36] studied the use of woven glass fibre fabric in the development of 3D honeycomb composites via vacuum assisted resin transfer moulding. The use of woven fabric showed interesting results in terms of flatwise compression and impact testing, surging as a possible substitute to metal honeycombs in energy absorption applications.

The examples presented before denote the effort which was, and is currently being put into developing more advanced manufacturing processes. From this broad range of technologies, one can be selected which allows for the production of complex 2D and 3D geometries, in a variety of materials: *additive manufacturing* (AM).

Additive manufacturing (AM) is defined in the ASTM International F2792 standard [37] as a process through which, joining layer upon layer of material, a 3D computed aided design (3D CAD) is converted into a physical object. AM focuses on direct production, skipping the intermediate steps of conventional methods, like deciding on which tools and additional fixtures may be required, reducing like this the use of material and energy, and facilitating the production of prototypes [38]. This is further exemplified in Figure 2.9, showing how there is little to no human intervention between the design and manufacturing stages for AM, with the basic steps of the AM process going swiftly from the CAD file development, conversion and transferring to the machine, to its final production.

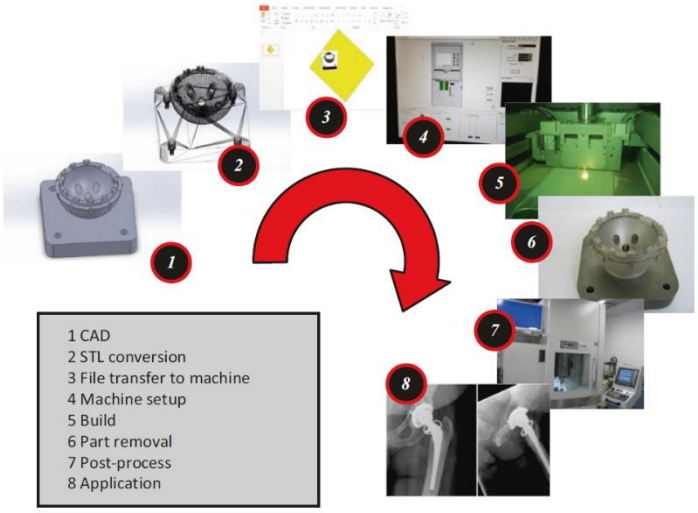

Figure 2.9: Eight general steps of an AM process [38]

AM is currently present in every major industry, with the main drivers of its continuous studying and improvement being the aerospace, automotive and medical industries, serving as a valuable tool in producing complex geometries with consequent material and time savings (automotive and aerospace), and allowing for a more direct and customized approach to every particular situation (medical). It is important to note how AM still serves as a rapid and low-cost process of prototyping [38], [39].

The ASTM F2792 [37] standard was also successful in providing a means of grouping current and future AM technologies, which are as such:

- *Binder jetting*, which groups AM processes in which a liquid binder is selectively deposited in order to join powder materials.
- *Direct energy deposition*, which groups AM processes which use focused thermal energy to melt the material as it is being simultaneously deposited.
- *Material extrusion*, which groups AM processes in which material is deposited selectively through a nozzle or orifice.

- *Material jetting*, which groups AM processes which consist in the selective deposition of droplets of material, with possible examples being wax or light-activated polymers.
- *Powder bed fusion*, which groups AM processes in which a powder bed is selectively fused with thermal energy. Powder bed fusion refers to processes where materials are not only fused by melting, but also sintering.
- *Sheet lamination*, which groups AM processes in which various sheets of material are bonded in order to create the final part.
- *Vat photopolymerization*, which groups AM processes in which a liquid light-activated polymeric material (contained in a vat) is cured selectively via exposition to light (photopolymerization).

The AM process through which the presently studied samples were produced is named *Selective Laser Melting* (SLM), but a number of other AM processes could be used (e.g., direct energy deposition). A more extensive review on the SLM process will be performed, as it was the one used in the present work.

Selective laser melting (SLM)

Selective laser melting (SLM) is a powder bed fusion process in which a high energy heat source, normally a high intensity laser, selectively melts and fuses consequent layers of powder. The manufacturing process starts with deposition of thin layer of powder on a substrate plate, which is melted and fused by the high energy source, according to the CAD data [40]. The substrate plate is then lowered so that a new layer of powder is deposited onto the previous one, repeating the process continuously until the final part is completed [40]. After completion, any remaining loose powder is removed and the part can proceed to post-processing, if needed. The SLM process is illustrated in Figure 2.10.

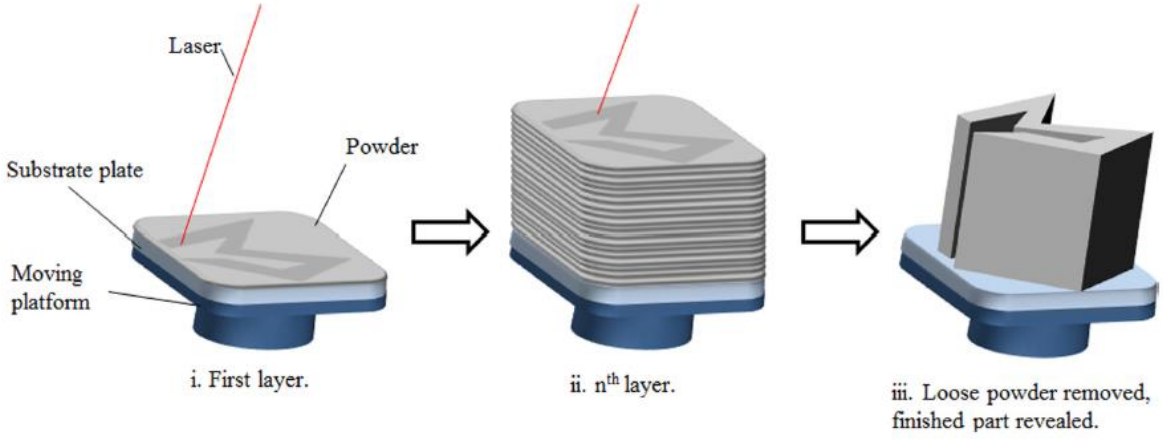

Figure 2.10: Schematics of the selective laser melting process [41]

Several parameters regarding the SLM process must be considered, with some examples being the laser power and scan speed, powder size and distribution and consequent layer size, atmosphere in building chamber, among others [41].

The thickness of the layers is generally between 20 to 100 μm, allowing for both appropriate flowability of powder and fine resolution. Larger powder particles lead to poor resolutions and increase in residual porosity, while smaller particles tend to agglomerate and consequently reduce powder flow [42]. The SLM process is often performed in a controlled inert atmosphere, usually nitrogen or argon gas, to prevent oxidation of the various materials. To help prevent distortion or cracking of the part due to high cooling rates, it is also possible to increase the temperature of the building chamber, normally by heating the substrate plate (up to 500ºC) [41]. Laser power is usually associated with the melting temperature of the fused material, with higher melting points requiring higher energy input. The previously mentioned parameters are mutually dependent, meaning altering one parameter may impact the remaining [38].

The SLM process is appropriate for a wide variety of materials. Thermoplastic polymers are widely used due to their relatively low thermal conductivities and melting temperatures, appropriate properties for this technology [38], [43]. Any metal deemed suitable for welding is considered an appropriate material for SLM processing, with aluminium, stainless steels, titanium and their alloys being some of the more common [38]. Ceramic materials are generally associated with selective laser sintering (SLS), a process similar to SLM in which powder particles never reach melting temperatures when fused, but recent studies have investigated the possibility of completely melting ceramic materials, like zirconia (ZrO_2) and alumina (Al_2O_3), to achieve less porosity in parts produced via AM [44].

SLM presents numerous advantages when compared to conventional methods, but suffers the same drawbacks as other AM processes. It allows for the processing of a wide range of materials, enables the development of complex geometries and internal features, and produces near net shape parts, reducing time loss in usually necessary intermediate tooling. On the other hand, it requires a considerable initial financial investment, is restricted to smaller parts due to the size restriction of existing SLM machinery, the tuning of process parameters can be time consuming and finished parts may exhibit rough surfaces which need post-processing [40], [45].

Regular honeycomb structures might not benefit as much from this versatile technology as other cellular structures, like lattice structures. But as grading is added to the honeycomb structure, generating a functionally graded material, AM's flexibility of design and production makes it a much more fitting solution.

2.3 Functionally Graded Materials

2.3.1 Overview

Functionally graded materials (FGMs) are materials whose characteristics and properties change gradually throughout their volume, which makes them extremely interesting in multifunctional applications [46]. Although materials with this particular characteristic have only been researched and looked up as reliable solutions for the past 50 years, they are constantly present in nature, with bamboo and enamel (teeth coating) being some examples of biological optimization via the grading of microstructure and composition [47], [48]. These examples are illustrated in Figure 2.11.

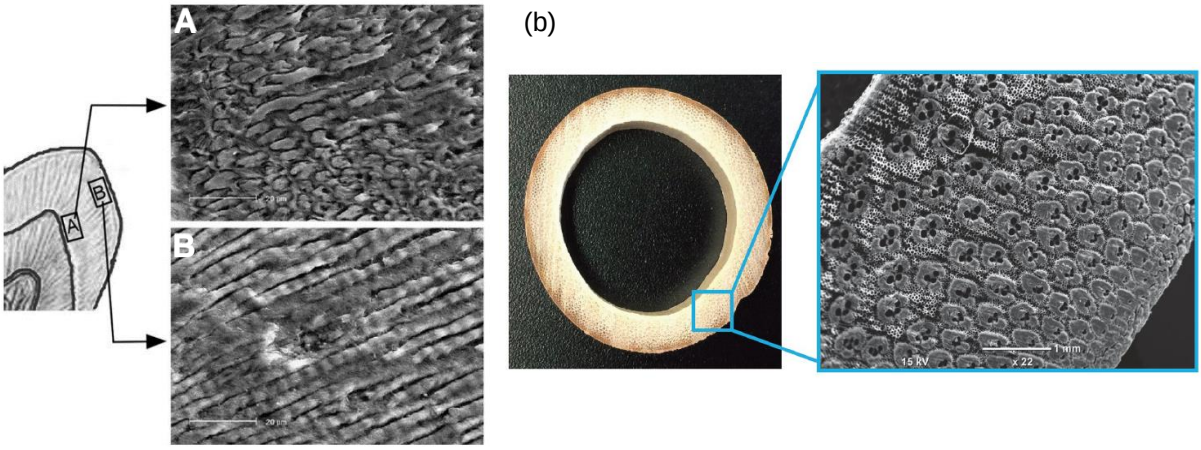

Figure 2.11: (a) Functionally graded enamel tooth coating; (b) Functionally graded wild moso bamboo [48], [49]

The first technical approaches regarding FGMs are associated with the introduction of gradients in polymeric materials, with Shen et al. [50] studying the spatial variation of monomers with different chemical nature in single phase systems, as well as crystallinity and porosity. But it was only in the 1980's that the first industrial proposition emerged, with Japanese researchers investigating solutions for the body of a spacecraft which had to withstand an extremely large temperature gradient (~1000ºC) between its exterior and interior. The solution appeared in the development of a material with gradually changing composition, which would allow for both better thermal resistance and mechanical properties [51], [52]. This inspired further investment and research in FGMs, leading to their gradual introduction in numerous industries, with some of the most impactful being the medical, defence and aerospace industries [53]. According to Mohammadi et al. [46], and due to the various properties which can be graded over the volume, FGMs should be classified based on changes in their *structure*, *gradient type*, *size and scale*, *physical state of material* and *type of deposition process*. From the previously five classifications, the most important are changes based on *structure* and *gradient type*, which will be further explored.

Classification of FGMs based on structure

Structure-wise, FGMs are classified into two categories: *continuous* and *discontinuous* [54], [55]. This helps categorize the manner in which the gradient factor changes through the bulk of the material [46].

Continuous gradients go along continuously through the material, with no perceivable interfaces, while discontinuous gradients show somewhat of a stepwise progression along the material, allowing for a clear separation between each gradient layer. This difference is well perceived, in Figure 2.12 (a).

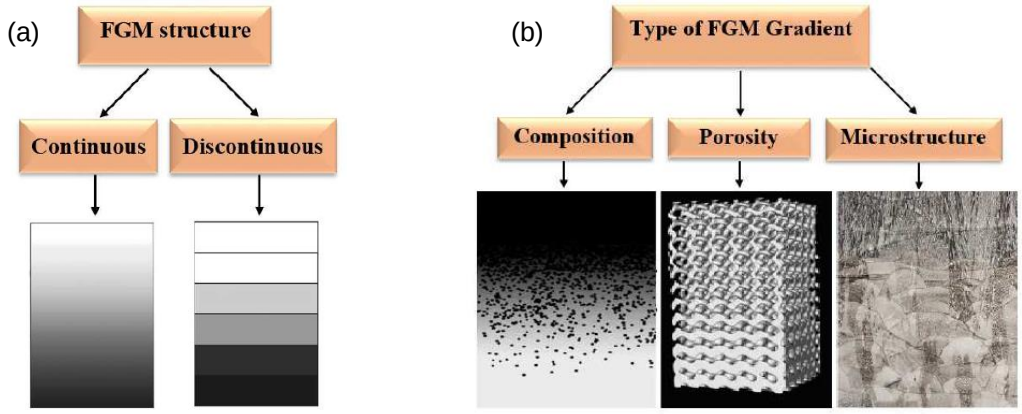

Figure 2.12: FGMs classification based on: (a) Structure; (b) Type of gradient [56]

The selection of FGMs based on structure depends strongly on the desired functionality, as each gradient distribution possesses its advantages. Continuous gradients have greater influence in situations in which good balance between multi-layers is necessary, like sound or heat absorption, while discontinuous gradients are more appropriate in situations in which a clear difference in properties is expected or a separation is beneficial, like preventing crack propagation with layer interfaces [46], [55], [57].

Classification of FGMs based on gradient type

FGMs are also classified depending on their gradient type, which can be divided into *chemical composition*, *porosity* and *microstructure* gradients, like presented in Figure 2.12 (b) [56].

The first FGMs were developed with a chemical composition gradient aiming to remove acute interfaces in composite materials, replacing it with a gradually changing one. Chemical composition gradient FGMs are usually multi-phased, meaning there are phase changes along the material as a consequence of the varying chemical composition, something that is finetuned and controlled in order to achieve the designed properties [58]. There exist rare exceptions in which single-phase FGMs are produced by varying the solubility of chemical agents used in the material.

Porosity gradient FGMs depend on the distribution of pores shape and size along the material, and are highly linked with biomedical applications, as many elements of the human body show porosity gradients [59], [60] This type of gradient can be obtained by controlling the shape and distribution of pores, but also by variating powder particles size when sintering [56].

Finally, the microstructure of FGMs can also be specifically adjusted along the bulk of the material to meet its requirements. This type of grading allows for the production of parts with very hard surfaces while maintaining some ductility in the core of the material, mainly via controlled solidification processes or heat treatments (mechanical processes also possible) [61]. It is especially applied in materials which must be simultaneously wear and impact resistant.

2.3.2 Functionally Graded Cellular Materials

Functionally graded cellular materials (FGCMs) are a derivate of FGMs, and consist fundamentally in cellular materials which show some sort of grading along its bulk volume, generally applied to cell size, as well as its distribution, and cell wall thickness [62]. These variations in cellular parameters are commonly merged in one generally inclusive term: *density gradient* [63–65]. An example of a FGCM is presented in the model illustrated in Figure 2.13.

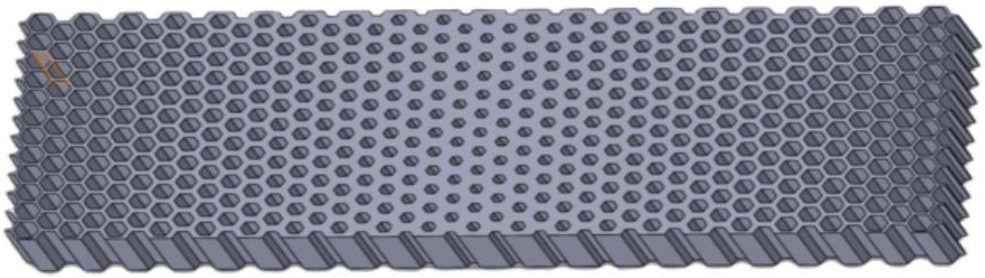

Figure 2.13: Example of a designed FGCM. Adapted from [66].

Even though cellular structures are proven to be advantageous in structural applications due to their load-bearing capacity paired with lower weight compared to their bulk counterparts, a major drawback comes up in terms of adaptability, as an increase in stiffness and strength comes at the cost of its energy absorption properties [7]. As further stated by Gibson and Ashby [7], an increase in relative density is generally associated to a higher resistance in cell wall bending and collapse, but also with an earlier densification and consequent lower energy absorption due to thicker cell walls. The implementation of a density gradient enables the tailorability of both these properties along specific directions, allowing the production of cellular materials with higher density in areas where deformation resistance, while still maintaining the energy absorption and low weight characteristics of cellular materials [67].

While the production of functionally graded cellular structures (FGCSs) can be performed via conventional methods, recent studies have proven the value in applying additive manufacturing processes into the fabrication of these structures, as these grant superior geometrical freedom and reduce the use of intermediate compounds (e.g., foaming agents) [68]. Choy et al. [69] studied the applicability of the SLM process in the production of functionally graded lattice structures with a titanium alloy (ASTM grade 5), obtaining satisfactory results, with an increase in specific energy absorption and plateau stress compared to its uniform density counterparts. Panesar et al. [70] investigated strategies in order to optimize material layout in additive manufacturing of cellular structures via topology optimization, reaching promising conclusions both in mechanical properties of structure in itself and manufacturing parameters. Nguyen et al. [71] further added to this topic, proposing the use of a level-set description strategy in multiscale design of FGCS for AM, obtaining results that show remarkable structural performance enhancements. Duraibabu et al. [68] analysed the compression behaviour of FGCSs with different cell shapes, concluding that the precise control of density gradient provided by AM technologies was translated into better energy absorption characteristics.

2.3.2.1 Recent Advances

FGCMs are a relatively recent group of materials, and their application in different industries, like the biomedical and aerospace, has proven advantageous. However, studies regarding this kind of structures are many times experimental, which is timely and costly [72]. Additionally, when numerical models are possible and the mechanical properties of FGCSs are simulated, it is generally based on outdated or insufficiently accurate theoretical models [73].

Therefore, efforts have been recurrently put into developing new models/parameters that help define or compare the characteristics of these structures, and even the impact that different gradients have in these same characteristics [62], [72–77]. The study of the effect of density gradients in the mechanical properties of structures can be difficult, depending on the level of complexity of the gradient.

Liu et al. [77] developed a more actual model regarding the influence of density gradient in the shock front formation and propagation of cellular rods in foams, as current models were only applicable to rods with constant density. The model was corroborated by numerical simulations, which were in agreement with the formulated theory, proving that the density gradient has a significant influence on the impact stress transmitted to the structure. Further exploring the influence of density gradients in the mechanical performance of honeycomb structures, Rua [6] developed three different types of density gradients regarding honeycomb structures by radially varying the cell wall length and, consequently, the cell wall thickness. The structures were tested numerically and experimentally (PLA and aluminium alloy samples) via uniaxial compression tests, obtaining superior values of stiffness and absorbed energy for graded structures when compared to regular honeycomb structures. Also by varying the cell wall thickness, Wu et al. [78] proposed a novel bi-graded honeycomb structure by implementing both out-of-plane and in-plane thickness gradients, variating relative density throughout the structure, obtaining positive results regarding specific energy absorption when compared to regular honeycombs. The complex structures were additive manufactured by fused deposition modeling, once again confirming the contribution this technology provided to the production of parts of additional complexity.

Liu et al. [79] studied the addition of functional grading to structures with fractal self-similarity features, which are structures that show similar geometry to themselves on all scales. This combination was performed by applying a variating fractal parameter to each layer of a traditional hexagonal honeycomb, consequently variating relative density along the structure. An asymmetric and a symmetric graded designs were developed, with the latter showing considerably higher energy absorption behaviour in both low-velocity impact (89% increase) and high-velocity impact (17% increase). Liu et al. [80] additionally studied the implementation a hierarchical topology to traditional honeycomb structures, targeting the improvement of the crashworthiness performance of these structures. The functionally graded hierarchical honeycomb structures were constructed by substituting the cell walls for regular hexagonal honeycombs of different sizes, creating a gradually differing relative density along the structure. Triangular shaped cells were also applied. The study concluded that the triangular sub-structure presented better results, with an increase of 32.2% in specific absorbed energy when compared to regular honeycomb structures, proving the prospective use of hierarchical gradients.

Chapter 3: Methodology

The purpose of the present study is to assess the effect of different geometrical parameters in the compressive behaviour of honeycomb structures. With this goal, the compressive behaviour of different structures was numerically simulated via the finite element method (FEM), as well as experimentally tested, with compressive testing. Three groups of regular hexagonal honeycomb structures, each with particular dimensions, were studied. Additionally, according to the models formulated by Rua [6], three groups of functionally graded structures were studied.

3.1 Materials and Manufacture

3.1.1 Aluminium (AlSi7Mg0.6)

Aluminium is, in terms of engineering applications, the most used non-ferrous metal in the world [81]. At first sight, aluminium does not appear as a good candidate material for AM applications due to its high reactivity with oxygen, creating oxides with much higher melting temperatures, and high thermal diffusivity. But it still remains as material which is easily available, with low density and high specific strength, motivating researchers to investigating different alloying substances which would increase the applicability of this metal to AM processes (mostly in powder bed fusion) [82].

The aluminium alloy utilized in the present study is designated AlSi7Mg0.6, or EN AC-42200 according to the European standard DIN EN 1706 [83], and produced by SLM Solutions Group. Even though this alloy was originally specified for casting applications, it has been gradually incorporated in SLM manufacturing due to its satisfactory corrosion resistance and weldability [84], [85].

A data sheet containing the mechanical data of the alloy in question was provided by the supplier, but some adjustments were necessary for the numerical simulations. The FEM software stipulates the use of true values of stress (σ_R) and strain (ε_R). Therefore, a conversion was applied as a function of the corresponding nominal values for stress (σ_N) strain (ε_N), as shown in Equations 3.1 and 3.2.

$$\sigma_R = \sigma_N\,(1 + \varepsilon_N) \tag{3.1}$$

$$\varepsilon_R = \ln(1 + \varepsilon_N) \tag{3.2}$$

In order to describe the plastic behaviour of the material, some coordinates of three points of the plastic segment of the stress-strain curve were provided: the material's yield stress ($\sigma_{y,N}$), the material's ultimate tensile strength ($\sigma_{U,N}$) and the elongation at break ($\varepsilon_{T,N}$). The strain at yield is obtainable by applying Hooke's law, as demonstrated in Equation 3.3:

$$\varepsilon_y = \frac{\sigma_y}{E} \tag{3.3}$$

It was further needed to calculate the plastic component of the true break strain ($\varepsilon_{pl,R}$), which can be achieved by subtracting the elastic component ($\varepsilon_{el,R}$) from the true break value ($\varepsilon_{T,R}$). By applying Hooke's law to the strain's elastic component, the following subtraction emerges (Equation 3.4), in which ($\sigma_{T,R}$) is the stress at breaking:

$$\varepsilon_{pl,R} = \varepsilon_{T,R} - \varepsilon_{el,R} = \varepsilon_{T,R} - \frac{\sigma_{T,R}}{E} \tag{3.4}$$

It is important to mention that, due to the unavailability of the break stress value, low necking is assumed, making the break stress similar to the ultimate tensile strength value, leading to the approximation in Equation 3.5.

$$\varepsilon_{pl,R} = \varepsilon_{T,R} - \frac{\sigma_{T,R}}{E} \approx \varepsilon_{T,R} - \frac{\sigma_{U,R}}{E} \tag{3.5}$$

Finally, a standard value of Poisson's ratio for aluminium alloys was chosen due to its absence in the provided data sheet. The chosen value was **0.33**, following the trend in past studies [6]. The mechanical and physical properties considered are presented in Table 3.1, with further information on other properties and chemical composition referring to this aluminium alloy present in Appendix A.

Table 3.1: Considered properties for the computational model regarding the aluminium alloy AlSi7Mg0.6.

Density [g/cm³]	Poisson's Ratio	Young's Modulus [MPa]	Yield Stress [MPa]		Ultimate Tensile Strength [MPa]		Ultimate Plastic Strain	
2.680	0.33	59000	Nominal	True	Nominal	True	Nominal	True
			211	212	375	405	------	0.070

3.1.2 Sample Manufacturing

The honeycomb samples analysed in the present work (Figure 3.1 (a)) were manufactured via SLM, in a SLM Solutions 125HL machine belonging to the École Nationale Supérieure des Mines d'Albi-Carmaux, in France, as in previous related studies [6], [86]. The SLM Solutions 125HL machine, as shown in Figure 3.1 (b), possesses a single laser of 400W of power, with width ranging from 70μm to 100μm and a maximum speed of 10m/s. The chamber in which the samples are manufactured has a volume of 125mm× 125mm × 75mm, using argon as an inert gas. This particular machinery allows for the fusion of singular material layers with thicknesses ranging from 20μm to 75μm.

(a) (b)

Figure 3.1: (a) Graded structures immediately after fabrication in a (b) SLM Solutions 125HL machine [87]

3.2. Modeling of 3D-CAD Structures

Both the regular and graded honeycomb structures analysed in the present work were originally designed by Rua [6], in a previous study. The 3D-CAD structures were modeled in the *SolidWorks* software, by Dassault Systèmes S.A, and later exported to the FEM software.

3.2.1 Regular Structures

The regular honeycomb structures designed in the present study were set to have a constant cell wall thickness (t) of 2.31mm, varying only in cell length (l) and cell core height (h). The designation of each honeycomb structure is based on the combination of its cell length ($l \equiv$ L) and cell core height ($h \equiv$ H), with a hypothetically structure with $l = 6$ and $h = 6$ being assigned the code L6H6.

The geometric parameters and characteristics of the designed regular honeycomb structures are present in Table 3.2., in which the apparent area consists in the multiplication of the maximum side lengths of the structure, which defines the rectangular area in Figure 3.2. (a). Images representing the in-plane and out-of-plane loading orientations are presented in Figure 3.2 (a) and (b), respectively, while images of both CAD and physical regular structures can be found in Appendix B.

Table 3.2: Designation and geometrical parameters for the regular structures.

l [mm]	Apparent area [mm^2]	Solid area [mm^2]	$\bar{\rho}$	h [mm]	Designation
6	65.81 × 66 (4343.46)	1449.63	0.338	6	**L6H6**
				10	**L6H10**
				12	**L6H12**
8	83.15 × 84 (6984.60)	1881.23	0269	6	**L8H6**
				10	**L8H10**
				12	**L8H12**
10	61.20 × 68 (4161.60)	948.43	0.228	6	**L10H6**
				10	**L10H10**
				12	**L10H12**

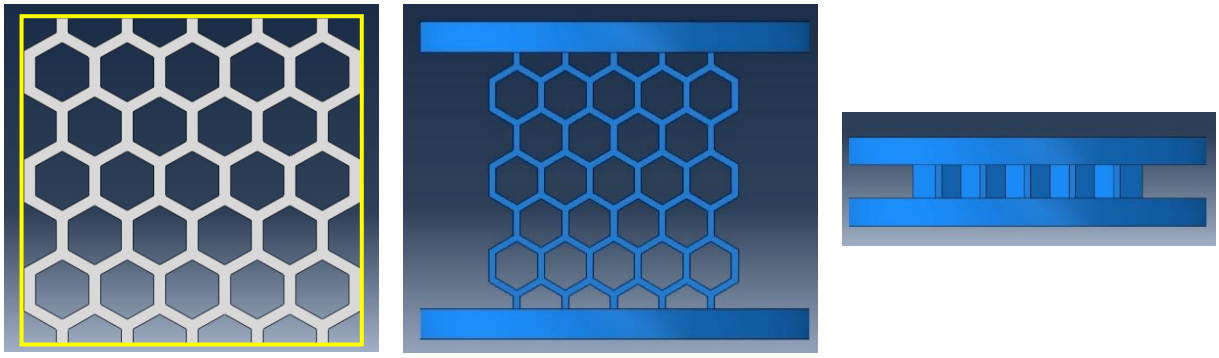

(a) (b) (c)

Figure 3.2: Definition of the (a) structures' apparent area and (b) in-plane and (c) out-of-plane loading orientations.

3.2.2 Graded Structures

As mentioned previously, three groups of graded honeycomb structures were analysed. Each group was designed by Rua [6] according to a specific grading, i.e., variation of density, with a resulting total of twelve different structures. Throughout the gradient structures, a constant cell core height was kept at 12mm. It is further important to refer that the designs were based on radial symmetry, with the density gradient starting in a central core cell and propagating in concentric circumferences, as exemplified in Figure 3.3.

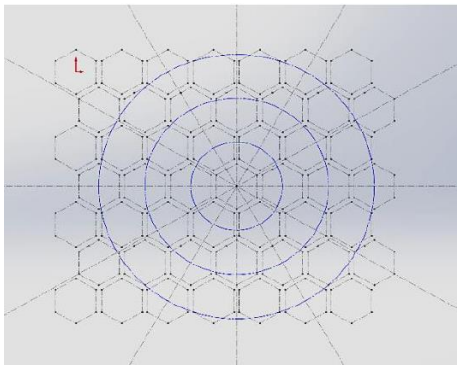

Figure 3.3: Main symmetry lines and exemplification of associated concentric circumferences [6]

The designation of each honeycomb structure was assigned depending on its gradient group, with the first and second graded structure of the first gradient group being assigned the designation *1A* and *1B*, respectively. The same applies to the remaining gradient groups.

3.2.2.1. Gradient 1

The design of the first gradient structures depended on fixed values of cell length, with cell wall thickness varying as a function of the previous parameter. As already mentioned, the grading followed the concentric circumferences, with each of these so called “belts” corresponding to a specific cell length value, starting in the centre cell.

Two variants were studied: one with increasing cell length ($l: 6 \rightarrow 8 \rightarrow 10$) and consequent decreasing cell wall thickness, and one with decreasing cell length ($l: 10 \rightarrow 8 \rightarrow 6$) and consequent increasing cell wall thickness. Geometric parameters and designations of the respective structures were as demonstrated in Table 3.3.

Table 3.3: Designation and geometrical parameters for the graded structures (gradient type 1).

l variation [mm]	Apparent area [mm^2]	Solid area [mm^2]	$\bar{\rho}$	Designation
$6 \rightarrow 8 \rightarrow 10$	91.59 × 91.35 (8366.47)	2698.21	0.322	**1A**
$10 \rightarrow 8 \rightarrow 6$		3514.44	0.421	**1B**

Figure 3.4 (a) and (b) shows the models for structures *1A* and *1B*, respectively. Images of the physical structures can be found in Appendix B.

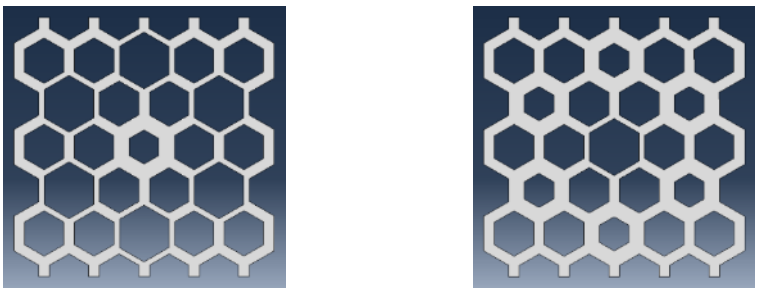

(a) (b)

Figure 3.4: Structure model for samples: (a) 1A; (b) 1B.

3.2.2.2 Gradient 2

The geometry of the structures designed according to the second gradient was once again dependent on cell length. Four different structures were designed following this method, with cell lengths varying between 7mm and 9mm, divided into increasing or decreasing density gradients.

For the decreasing density gradient, the central cell was designed with a cell wall length of 7mm, which progressively increased by an increment 0.5mm with each concentric circumference. Two different structures were developed with this grading, differing solely on the cell wall length of the four cells in the corners (either 7mm or 8.5mm).

For increasing density gradient, the central cell wall was designed with a cell wall length of 9mm, which progressively decreased by an increment of 0.5mm with each concentric circumference. With the same criterion of the previously gradient, two different structures were developed (either 7.5mm or 8.5mm).

Geometric parameters and characteristics of the respective structures were as demonstrated in Table 3.4., with Figure 3.5 (a-d) showing the models for structures *2A*, *2B*, *2C* and *2D*, respectively. Images of the physical structures can be found in Appendix B.

Table 3.4: Designation and geometrical parameters for the graded structures (gradient type 2).

l variation [mm] (corner l)	Apparent area [mm^2]	Solid area [mm^2]	$\bar{\rho}$	Designation
$7 + 0.5$ (8.5)	100.46×102 (10246.92)	4534.70	0.443	**2A**
$7 + 0.5$ (7)		4776.32	0.466	**2B**
$9 - 0.5$ (7.5)		4368.43	0.426	**2C**
$9 - 0.5$ (8.5)		4202.15	0.410	**2D**

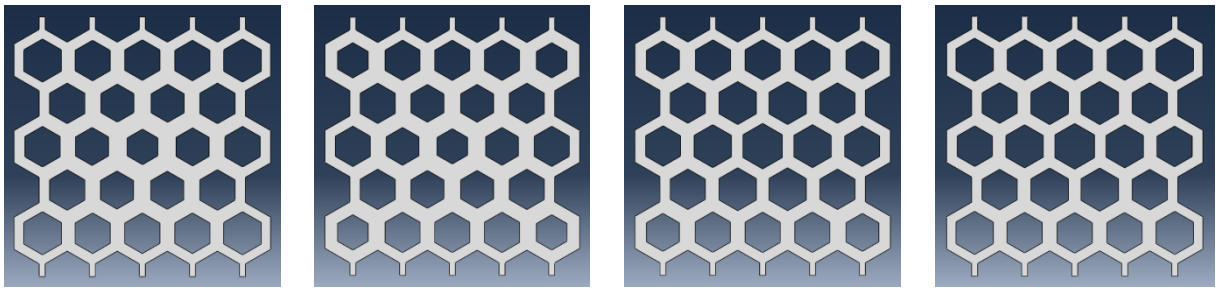

(a) (b) (c) (d)

Figure 3.5: Structure model for samples: (a) 2A; (b) 2B; (c) 2C; (d) 2D

3.2.2.3 Gradient 3

The structures comprising the final and third gradient group were designed according to a gradient parameter R. The R parameter is calculated according to certain geometric variables, which Rua [6] describes as: the length from the centre cell's most distant wall thickness to the side end of the structure (L^*), the length from the centre cell's most distant wall thickness to the end of an i cell (x_i), the cell wall in-plane thickness of an i cell (d_i), and half of the base cell length (l). An example is present in Figure 3.6.

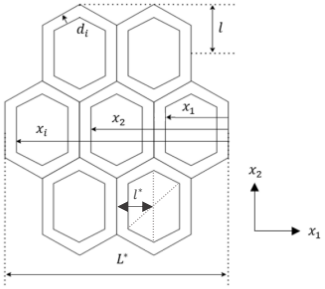

Figure 3.6: Considered geometrical variables for R parameter calculation. Adapted from [6]

The parameter consists in the slope of a liner function between two fractions ($\frac{x_i}{L^*}$ and $\frac{d_i}{l}$), which describes the cell wall length and consequent density gradient increments, with higher R parameter values associated with steeper density gradients. Positive R parameters indicate a decrease in density from centre to exterior, while negative R parameters indicate the opposite. As demonstrated in Figure 3.7, values of x_i and d_i are assigned for the initial and final cells, obtaining the slope of the size function and consequent R parameter.

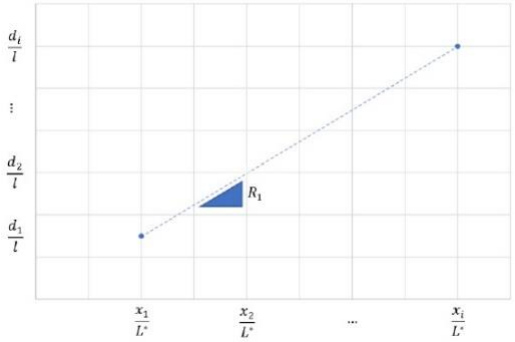

Figure 3.7: R function and consequent R parameter. Adapted from [6]

To maintain coherence in the present work, cell wall thickness of an i cell should be referred as t_i. Additionally, for future use of the R parameter, it is suggested that the length (l) be converted to a different variable (l^*) corresponding to the distance from the wall thickness to the centre of the cell, along the x_1 axis, as demonstrated in Equation 3.6 and Figure 3.6.

$$l^* = \left(l \times \cos\frac{\pi}{6}\right) + d_i \tag{3.6}$$

Geometric parameters and characteristics of the respective structures were as demonstrated in Table 3.5, with Figure 3.8 showing the models for the designed structures and said designations. Images of the physical structures can be found in Appendix B.

Table 3.5: Designation and geometrical parameters for the graded structures (gradient type 3).

R parameter	Apparent area [mm^2]	Solid area [mm^2]	$\bar{\rho}$	Designation
+ 0.22	88.51 × 90 (7965.90)	2572.60	0.323	**3A(+)**
- 0.22		1910.90	0.240	**3A(-)**
+ 0.31		2113.53	0.265	**3B(+)**
- 0.31		2371.00	0.298	**3B(-)**
+ 0.37		1584.65	0.199	**3C(+)**
- 0.37		2668.46	0.335	**3C(-)**

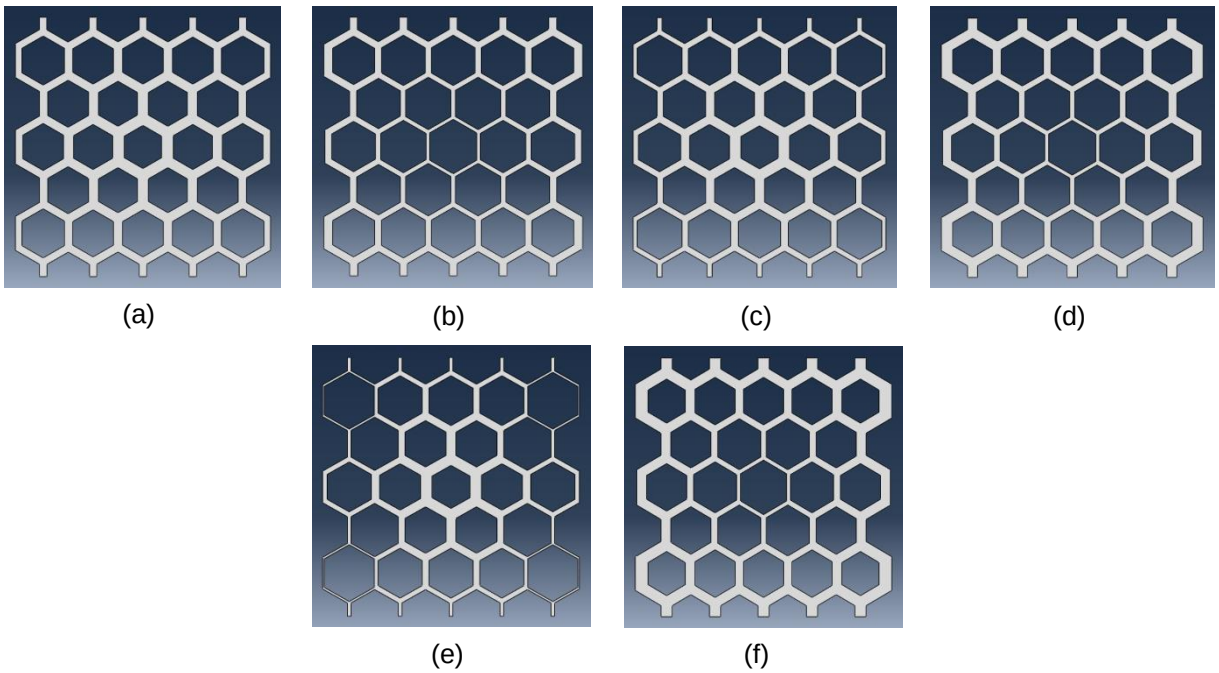

Figure 3.8: Structure model for samples: (a) 3A(+); (b) 3A(-); (c) 3B(+); (d) 3B(-); (e) 3C(+); (f) 3C(-)

3.3 Finite Element Modeling

As mentioned in previous chapters, the numerical simulations performed in the present study were ran in a finite element analysis (FEA) software, most specifically on *ABAQUS 2022*, by Dassault Systèmes S.A. The computational model consisted in the uniaxial compression testing of the different designed structures, with the modeling sequence consisting in the following steps, described in the system as "modules":

- *Part* module.
- *Property* module.
- *Assembly* module.
- *Step* module.
- *Interaction* module.
- *Load* module.
- *Mesh* module.
- *Job* module.
- *Visualization* module.

Finally, it is important to note that the ABAQUS software simply assumes that the user employs consistent units, meaning the user has flexibility in terms of choosing appropriate units as long they match between each other. This being said, the units chosen for the present work were millimetre (mm) for distance and newton (N) for force. Consequently, it stays implied that the unit for energy was millijoule (mJ), and for stress was megapascal (MPa).

3.3.1 Part module

The first step in developing the computational module consists in importing and/or designing the parts involved in the simulation. In the present case, the parts involved in the uniaxial compression testing were the honeycomb structures and an upper and lower compression plates from the testing machine. The compression plates were created as 3D solid "deformable" type parts, with the intent of having similar geometry to the real ones involved in experimental testing, consisting in cylindrical shapes of radius of 70mm and extruded by 10mm, as shown in Figure 3.9.

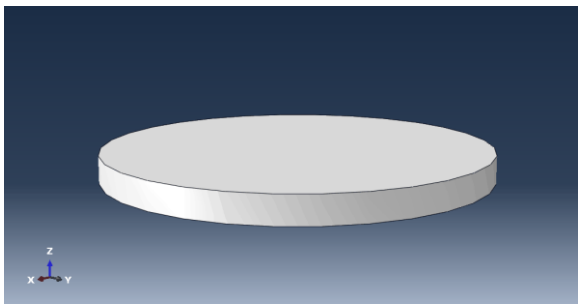

Figure 3.9: Modeling of the compression plate part.

The CAD honeycomb structures were imported as .IGS files, and defined with a very high Young's modulus to ensure ideal rigid behaviour.

3.3.2 Property module

The property module allows the user to define the properties of materials used in the simulations and to assign those materials to the different designed parts. The process consists in defining the various properties of a material (e.g., physical, mechanical, electromagnetic), and creating and assigning *sections*, which are limited region containing information about properties. These sections can be assigned to parts, but also to regions of parts, depending on the goal.

The first step was to formulate the materials representing the aluminium alloy used in the fabrication of the honeycomb structures and the compression plates, which were named “aluminium” and “rigid”, respectively. For “aluminium”, two scenarios emerge:

- A scenario in which the material’s response is purely elastic, being mechanically defined by the Young’s modulus and Poisson’s ratio (Figure 3.10 (a)).
- A scenario in which the material’s response is elastoplastic, being mechanically defined by the Young’s modulus, Poisson’s ratio and an additional description of the plastic segment of the material’s stress-strain curve, in the form of multiple points of the curve (Figure3.10 (b)). In this case, two points were used, as calculated in Table 3.1 (true yield stress and strain and true ultimate stress and strain).

In addition to the assigned values, the material was also computed to have isotropic hardening, meaning the yield stress increases (or decreases) in all stress directions as plastic straining occurs and that any anisotropy developed during deformation is neglected [88]. While metals normally show kinematic hardening, this option does not affect the simulation, as the samples were only to be simulated in one orientation.

The “rigid” material was formulated as purely elastic, and in a way in which the compression plates would suffer virtually no deformation, with the deformation in the system being purely induced in the honeycomb structures. This is achieved by assigning a Young’s modulus several orders of magnitude above the one of the material to be tested and an exceptionally low Poisson’s Ratio, illustrated in Figure 3.10 (c).

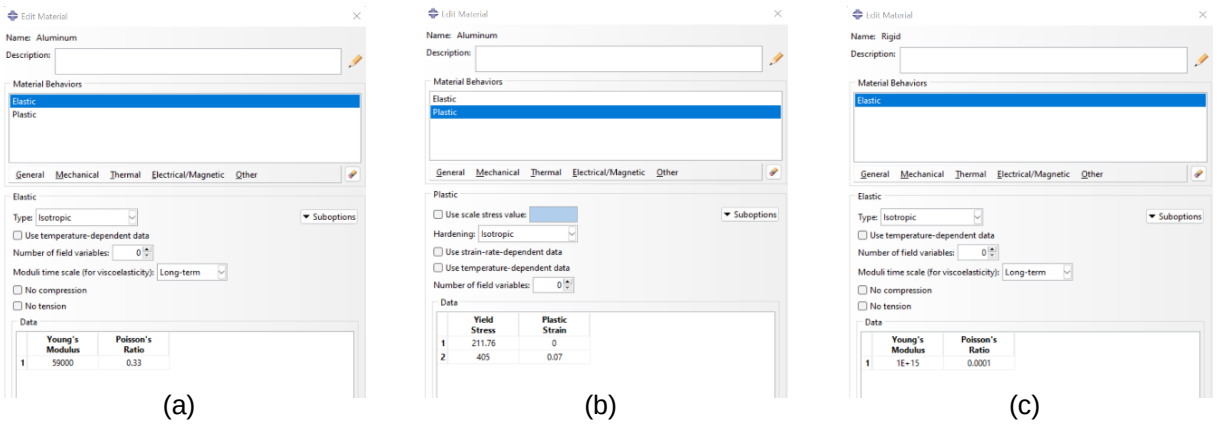

(a) (b) (c)

Figure 3.10: Tabs referring to: (a) Elastic properties of “aluminium”; (b) Plastic properties of “aluminium”; (c) Elastic properties of “rigid”

The following step was to create sections and subsequently assigned them to each region, in this case each part. Using the command *Create Section, a* section named “Honeycomb” was created regarding the material “aluminium” and attributed to the honeycomb part using the command *Assign Section*, while a second section named “Plate” was created regarding the material “rigid” and attributed to each of the two plate parts. Both sections were created under the assumption they would be assigned to solid and homogeneous parts, even though this is not entirely accurate for the real honeycomb structures. Although the physical honeycomb structures possess a level of porosity expected from AM processes, they are assumed to be homogeneous in terms of computational modeling.

3.3.3 Assembly Module

The assembly module allows the user to join the previously designed parts in the intended apparatus, which in the present case would be the uniaxial compression test machine. The various parts are converted to *instances*, which are created as *dependent* using the *Create Instance* command, allowing each part to later be meshed individually. In the present study, the instances created were named “Lower Plate” and “Upper Plate” for the compression plates and the specific designated code for each honeycomb structure.

Using the command *Translate Instance*, all instances were positioned in a way that their geometrical centre would be along the *z axis*. Finally, as exemplified in Figure 3.11, the command *Translate to* was utilized to move the surfaces of the compression plates into contact with the honeycomb structure. This command permits the translation of a movable surface (red) towards a fixed surface (purple) via a direction of movement, in this case the *z axis*. By choosing a null *clearance*, the surfaces will come into contact.

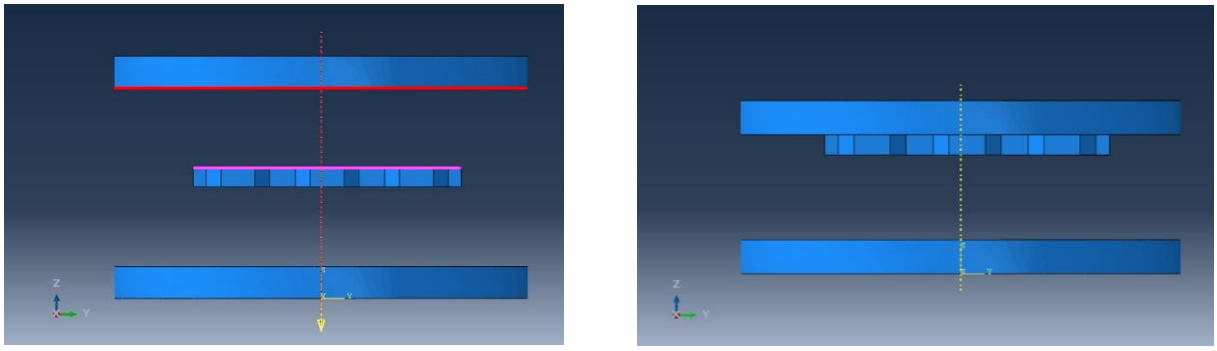

(a) (b)

Figure 3.11: (a) Selection of moveable surface (red) and fixed surface (purple) in the command “Translate to”; (b) Outcome of the “Translate to” command”

After repeating the command for the lower plate, the instances are joined, thus creating the final assembly exemplified in Figure 3.12.

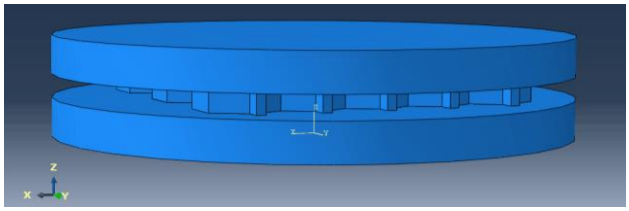

Figure 3.12: Final assembly

3.3.4 Step Module

The step module focuses on the division of the problem history into convenient phases, or periods, of loading named *steps*. If the problem in question has varying loading and/or boundary conditions through time, several steps can be created. For each step, the user chooses a particular analysis procedure, varying from the duration and increments at which the simulation is going to progress, to the variables to be recorded by the software.

The present model did not have varying conditions throughout the simulation, so one single step was created. When creating the step in the *Create Step* tab, one needs to define the type of simulation procedure, which was “Static, General” in the present work. This type of problem is generally applied to static stress analysis, like the present one, in which static equilibrium is assumed. The step needs to be further defined with crucial parameters which assure the outcome of the simulations, done so by filling the 3 different tabs opened by the command *Edit Step*:

- In the *Basic* tab (Figure 3.13 (a)), it was firstly defined the time period of the step, which was left as 1. As the problem in question is static, without strain rate dependence or creep strain involved, it does not depend on the test duration, so any other value could have been chosen. *Nlgeom* was turned on, as displacements may become large enough to take into account *Non-linear Geometry*. An automatic stabilization was chosen to reduce divergence.
- In the *Incrementation* tab (Figure 3.13 (b)), increment size and number can be selected, controlling how the step is divided, and how the load is distributed between each increment. Ideal increment size differs greatly from simulation to simulation, with incrementation for the present model chosen to be *automatic* and with *initial, minimum and maximum increment sizes* of 10^{-10}, 10^{-15} and 1, respectively. Like this, the first increment size is established, and the software chooses the size of subsequent increments. In some cases, the initial and minimum increment sizes had to be lowered due to errors in the simulation. A large maximum number of increments was selected (1000).
- The *Other* tab was left as it was (Figure 3.13 (c)).

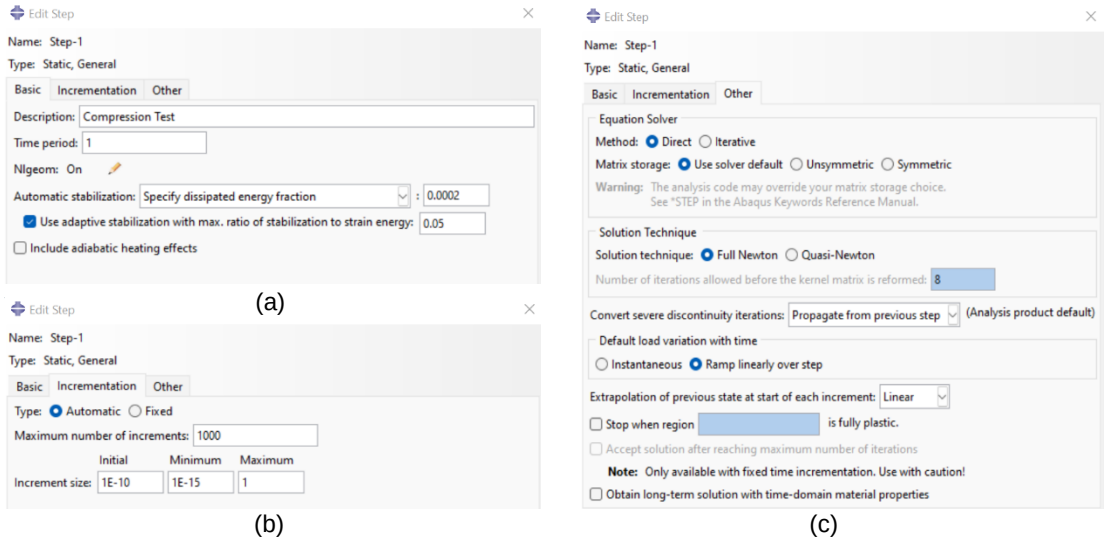

Figure 3.13: Tabs regarding the command “Edit Step”: (a) Basic options; (b) Incrementation options; (c) Other options

It is still in the step module that the *output variables* the software will record during the simulation are specified, and also the frequency at which they are recorded. Automatically, ABAQUS generates a *field output request* (data spatially distributed over the entire model) and a *history field output* (data at specific points in the model) over a number of increments. The impactful variables requested were solely *field output variables*: stress components and invariants ("S"), including von Mises equivalent stress ("MISES"), total strain components ("E"), plastic strain components ("PE"), logarithmic strain components ("LE"), translations and rotations ("U) and reaction forces and moments ("RF").

3.3.5 Interaction Module

The interaction module allows the user to define and manage the mechanical interactions between regions or instances of a model and its surroundings, while also applying certain constraints between said regions. In the present work, it was necessary to define the contact properties between the honeycomb structure and the compression plates, more specifically the occurrence of friction. Firstly, the interaction type is chosen as being *Contact* in the *Create Interaction Property* command, which opens a new tab in which is possible to add contact property options. Under *Mechanical* options, *Tangential Behaviour* was selected with a *Friction formulation: Penalty*, which allows the introduction of a friction coefficient which governs the contact between the two surfaces. As in previous related works [62], [89], a value of 0.2 was chosen for the friction coefficient. Additionally, *Normal Behaviour* was selected. The selected name for the interaction properties was *IntProp-1*.

With the contact interaction properties defined, the interactions were assigned with the command *Create Interaction*. Two *Surface-to-surface contact* interactions were assigned in the initial step and propagated to the next, which was designed previously: one between the lower compression plate and the honeycomb structure (lower contact interface) and one between the upper compression plate and the honeycomb structure (upper contact interface). When assigning interactions, it is mandatory to choose a *main* and a *secondary* surface, which were chosen as the compression plates and the honeycomb surfaces, respectively. This opens a new tab (Figure 3.14), in which the previously defined interaction properties can be selected.

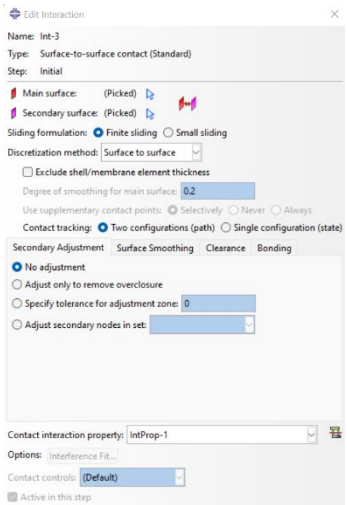

Figure 3.14: Tab regarding the "Surface-to-surface contact" interaction options

3.3.6 Load Module

The load module is where any conditions which induce a change in the response of the initial state of the assembly are created and managed (e.g., concentrated forces, prescribed displacements, or other boundary conditions). In the present work, boundary conditions regarding the movement of the compression plate instances were assigned, with no loads applied (loading emerged as a response from the movement and contact between plates and honeycomb). The two conditions were as follows:

- By opening the *Create Boundary Condition* tab, *Encastre* was selected and assigned to the whole of the lower plate instance (in the initial step). Like this, the two surfaces of this instance were denied of any rotational or translational movement.
- The same was performed for the upper plate instance, but selecting instead the option for *Displacement/Rotation*. After assigning the boundary condition to the whole of the upper plate instance, a value for negative displacement in the U3 (*z axis*) was attributed, meaning the instance would move in the direction of the other plate and honeycomb structure. The displacement for the remaining directions, as well as rotation in every direction, were made null.

The displacement value was mostly kept constant regarding the different geometries, with some necessary adjustments being introduced as necessary. For example, some of the graded structures with a steeper gradient had very small contact surfaces (in-plane), which would deform rapidly and crash the simulation, which in this case led to a decrease in displacement. This being said, the general value of displacement chosen was 3mm (in-plane compression) and 1.5mm (out-of-plane compression), with the exception of regular geometries with a cell core height (h) of 6mm, in which the displacement was 1.2mm (out-of-plane). An illustration of the assigned boundary conditions is shown in Figure 3.15.

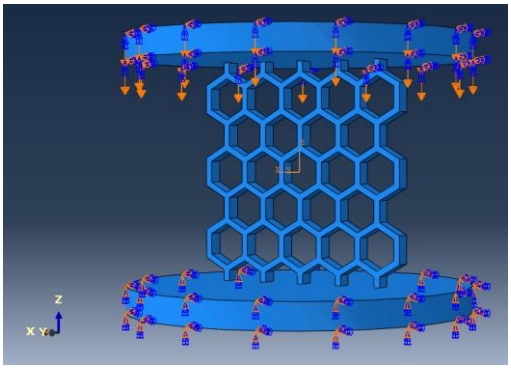

Figure 3.15: Illustration of the boundary conditions imposed on the assembly

3.3.7 Mesh Module

After establishing the simulation parameters in the previous modules, it is necessary to *mesh* the part instances individually. The process of meshing starts by *seeding* the parts via the *Seed Part* command, in which an *Approximate global size* of each finite element is suggested by the software (*global seed size)*. After deciding on this parameter, the user must decide the element type to be assigned to each region (e.g., quadratic or linear, and its geometry), which is possible via the *Assign Element Type* command. Finally, a mesh is attributed to each part instance via the command *Mesh Part* (Figure 3.16 (a) and (b)).

Generally, the global seed size suggested by ABAQUS is relatively high, originating coarser meshes (with fewer elements). This being said, it is necessary to refine the mesh by lowering the global seed size and occasionally altering the meshing controls or element geometry. This refinement of the mesh is done by performing a *convergence analysis*, which will be further explored in a following chapter.

For the present work, due to their simpler geometry and subsidiary influence in the study, the compression plate instances were assigned a higher global seed size than the honeycomb structures. This also allowed for the reduction of simulation time. The element type was kept constant for all instances, with a ten-node quadratic tetrahedral element type (C3D10) being chosen. This element type was chosen from the *Family: 3D Stress* of the *Element Library: Standard*, and apart from changing the *geometric order* from *linear* to *quadratic*, all other options were left as ABAQUS default settings. An additional step was performed via the *Verify Mesh* command in order to analyse the quality of the mesh. This command analyses the mesh and highlights any errors or poor elements present, as illustrated in Figure 3.16 (c).

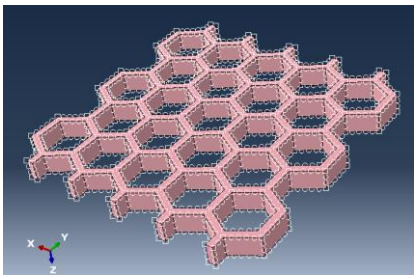

(a)

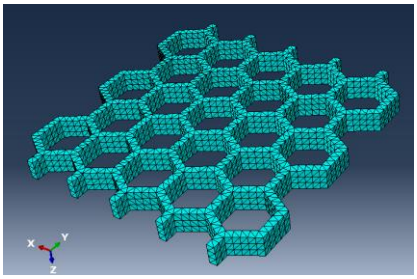

(a)

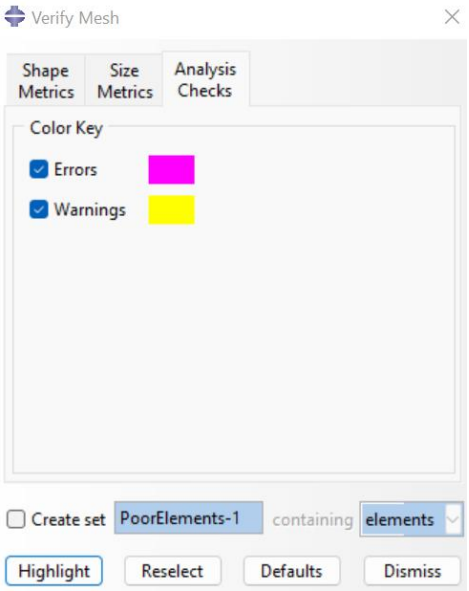

(a)

Figure 3.16: Illustrations of: (a) Seeded part; (b) Meshed part; (c) Verify Mesh command

3.3.8 Job Module

The job module is the one in which the simulation is submitted. With this intent, a *job* is created for the developed computational model using the command *Create Job*. This opens up an *Edit Job* tab, which in the present work was left with the default settings of the software. After this, the *Job Manager* tab is opened in order to assess and submit different simulations (jobs). The ABAQUS software allows the running of a *data check* on each job before submitting, which identifies any errors regarding the model. If nothing appears, the job is submitted via the *Submit* option. The simulation's evolution can be accompanied via the *Monitor* option, and when finished, the results can be visualized via the *Results* option.

3.3.9 Visualization Module

The visualization module allows the analysis of the visual representation of the simulation results across the geometry, as well as the post-processing of the same data. By using the command *Plot Contours on Deformed Shape* and selecting the variable to analyse, the software presents the resulting data distribution of said variable along the geometry. The software automatically presents the solution of the last increment, but the user is able to access the solutions at every increment time. An example of a deformed part instance in the visualization module can be seen in Figure 3.17.

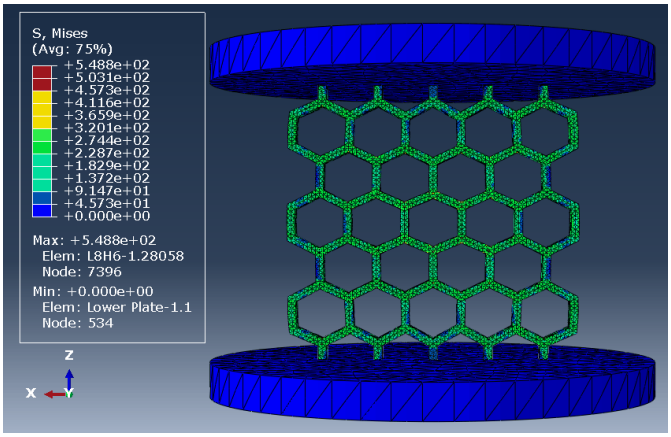

Figure 3.17: "Visualization Module" (deformed L8H6 sample with parameter von Mises stress).

In order to compare the simulated behaviour of the honeycomb structures with the experimental ones, an analysis of the requested output variables was performed:

- On the honeycomb structures: von Mises stresses (*Primary: S, Mises*) in order to ascertain stress levels and thus compare its magnitude between structures; also, plastic strain components (*Primary: PE, Max Principal*) in order to observe and quantify the permanent plastic deformation after unloading.
- On the moveable compression plate: the reaction forces corresponding to the *z axis* (*Primary: RF, RF3*) and the displacement along the same axis (*Primary: U, U3*).

The latter output variables, corresponding to the moveable compression plate, were utilized to formulate the force-displacement curves (and later stress-strain). These applied forces on the honeycomb structure can be taken from the compression plate as reaction forces due to the assumed static equilibrium. Firstly, a *display group* is created with only the upper compression plate instance. Via the command *Create XY Data*, the option *ODB field output* allows for the selection and extraction of data from any step. The *variable output position* was changed to *Unique Nodal* and the displacement along the *z axis* selected (*U3*), subsequently selecting one random node on the instance using the *Pick from viewport* option in the *Element/Nodes* tab. The specific data was then saved under the option "*as is*". For the reaction force (*RF3*), the process was similar, changing only in the number of nodes selected, which in this case must be all of the nodes comprising the instance.

Due to the large number of nodes and consequent individual data retrieved regarding reaction forces, it was necessary to add them in one englobing force value. This was attainable via the *Operate on XY data* in the *Create XY Data* command, opening a tab which allows for the treatment of XY data. The expression *sum((A,A,…))* was selected, in which the values for "A" would be the value of reaction force recorded in each node, creating a new XY data file, named "SUMForce", representing the summed values. Finally, the expression *combine(X,X)* was selected and the values for U3 and SUMForce introduced, specifically in this order. It is important to mention that, as the displacement was carried in the negative direction of movement and the force is the reaction of the intended forces, a minus signal must be included in the expression to standardize the results, resulting in the following expression: *combine(-U: U3,-SUMForce)*.

Using the option *Plot Expression*, the combined data is portrayed graphically. The plot, which corresponds to the force-displacement curve of the compression test simulation, can be exported via the *plug-ins tool: Excel Utilities*.

3.3.10 Mesh Refinement (Convergence Analysis)

Upon finishing the definition of the computational model, a mesh refinement must be performed. This step allows the user to ascertain the convergence of the results, discovering the ideal number of elements which allows for the most precise data in the least computationally heavy model. In the present work, even though the different honeycomb structures possessing significantly diverging geometries, it would be extremely time-consuming to perform a convergence analysis for each singular one. This being said, one regular and one graded structures were chosen (*L6H10* and *2D*, respectively), and a convergence analysis performed. The analysed variable in terms of convergence was the von Mises stress (MISES), in three different nodes. The three nodes were chosen with identical positions regarding the geometry, which can be found in Appendix C. The mesh refinement was performed regarding on global seed size, annotating the consequent number of nodes and elements, as well as simulation time. Finally, the deviation of values was calculated via the calculation of the relative error, as demonstrated in Equation 3.7, in which $\bar{\sigma}_{M,i}$ is the average von Mises stress obtained in the mesh i, and $\bar{\sigma}_{M,i-1}$ the same but for the previous mesh.

$$Error\ (\%) = \left| \frac{\bar{\sigma}_{M,i} - \bar{\sigma}_{M,i-1}}{\bar{\sigma}_{M,i-1}} \right| \times 100 \tag{3.7}$$

The Tables 3.6 and 3.7 show the global size, number of elements and nodes, values for von Mises stress and subsequent error for the various meshes in the regular structure, with the convergence analysis results for the graded structure present in Appendix C. For the present case, a maximum error percentage was set at 5%. This said, analysing both tables, as well as the evolution of von Mises stresses with mesh refinement for the different nodes (Figure 3.18), a global seed size of 1.4mm was selected. This value ensures appropriate convergence, with the lowest error percentage while keeping the simulation time at a relative low duration. For the graded structures, a global seed size of 1.4mm was also chosen.

Table 3.6: Parameters regarding the various meshes simulated for the convergence analysis

Global seed size [mm]	Number of nodes	Number of elements	Simulation time [s]
2.2	25811	16043	2189
2	30514	17344	2506
1.8	37923	21793	3131
1.6	54719	31261	5619
1.4	61166	34742	7414
1.3	90348	52685	16066
1.2	90488	52755	12385
1.1	115975	69940	16726

Table 3.7: Von Mises stress values and errors obtained regarding the various meshes in the convergence analysis

Global seed size [mm]	von Mises Stress (Avg: 75%) [MPa]			Error [%]		
	Node 1	Node 2	Node 3	Node 1	Node 2	Node 3
2.2	367.568	393.682	215.569	24.41	6.00	3.36
2	303.353	362.761	216.989	17.47	7.85	0.66
1.8	331.875	371.437	204.297	9.40	2.39	5.85
1.6	302.868	388.623	215.822	8.74	4.63	5.64
1.4	301.625	398.916	218.588	0.41	2.65	1.28
1.3	302.285	420.864	211.996	0.22	5.50	3.02
1.2	293.797	391.631	214.358	2.81	6.94	1.11
1.1	304.902	399.923	214.363	3.78	2.12	0.00

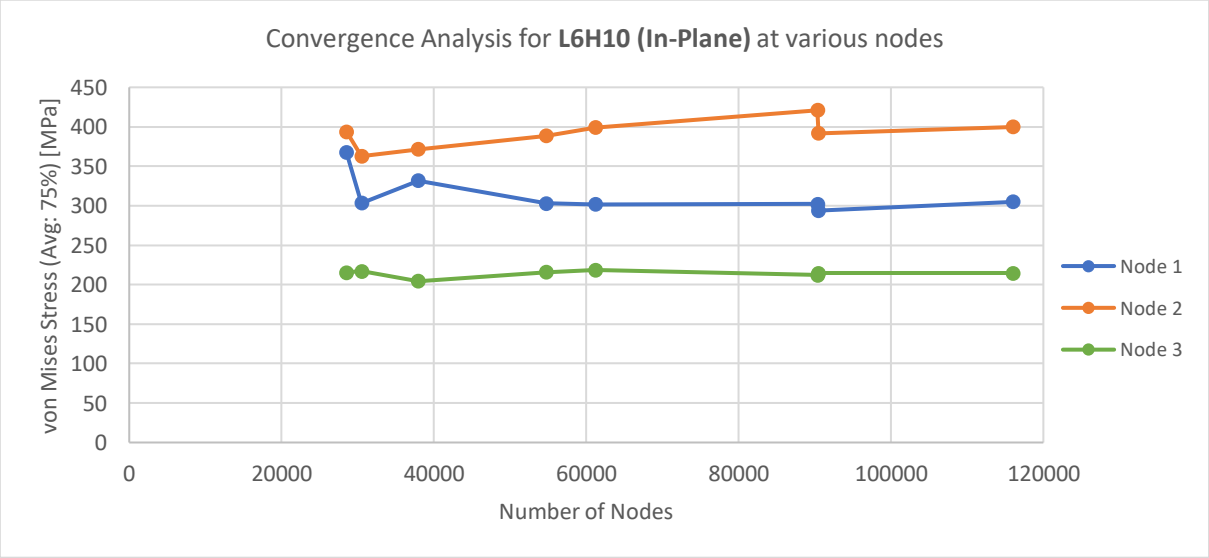

Figure 3.18: Convergence analysis plot for sample L6H10 (In-Plane) at various nodes.

3.4 Experimental procedure

The experimental procedure carried out in the present work can be divided into three separate steps, consisting of:

- Preparation and classification of samples.
- Uniaxial compression testing of prepared samples.
- Data treatment and fracture analysis.

3.4.1 Sample preparation and classification

Metallic samples produced via AM processes are usually associated with poor surface finishing, being common to perform some sort of post-processing to improve its tribological properties or simply improving its visual appearance. During a first assessment of the structures in the present study, it was anticipated that the excess material on the surface of the structures, could act as stress concentration points, thus possibly altering the true behaviour of the structures. The excessive material serves as support between subsequent parts, while also providing better heat conduction, usually under the form of a grid and/or pillars, as perceived in Figure 3.19.

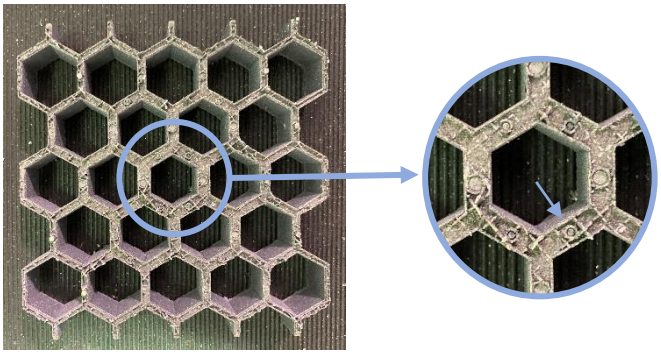

Figure 3.19: Magnified view of the typical excess material present in samples produced via AM (sample 3B(+)).

The removing of the material was performed via a *OPTI MF 4 Vario* milling machine, by Optimum Machines, at Laboratório de Técnicas Oficinais (LTO) – Departamento de Engenharia Mecânica (DEM), Instituto Superior Técnico. The milling was conducted with a carbide face mill cutter, with layers of material between 0.2mm and 0.4mm being removed sequentially until surface quality was acceptable and the cell core height was according to the design. The machine apparatus, as well as the direction and speed of rotation, are presented in Figure 3.20.

Figure 3.20: Milling machine apparatus (OPTI MF 4 Vario).

After finishing the post-processing, each sample was photographed in order to visually compare the permanent deformation after the compressive testing. The samples were further weighed at the Laboratório de Materiais Nanoestruturados (NanoMATLab) – DEM, Instituto Superior Técnico. The images and weight of the post-processed samples can be found at Appendix B.

3.4.2 Uniaxial Compression Testing

The samples were subjected to the compression tests, which were performed according to the ASTM C365-94 standard [90]. The machinery utilized was an Instron 3369 universal mechanical testing machine, equipped with a load cell of 50kN and a Teflon sheet between the contact surfaces of structure/plates, as visible in Figure 3.21, with the tests being performed at the Laboratório de Mecânica Experimental – DEM, Instituto Superior Técnico. The software used to process the data was the *Instron Bluehill Universal*, the setup of which can be seen in Figure 3.22.

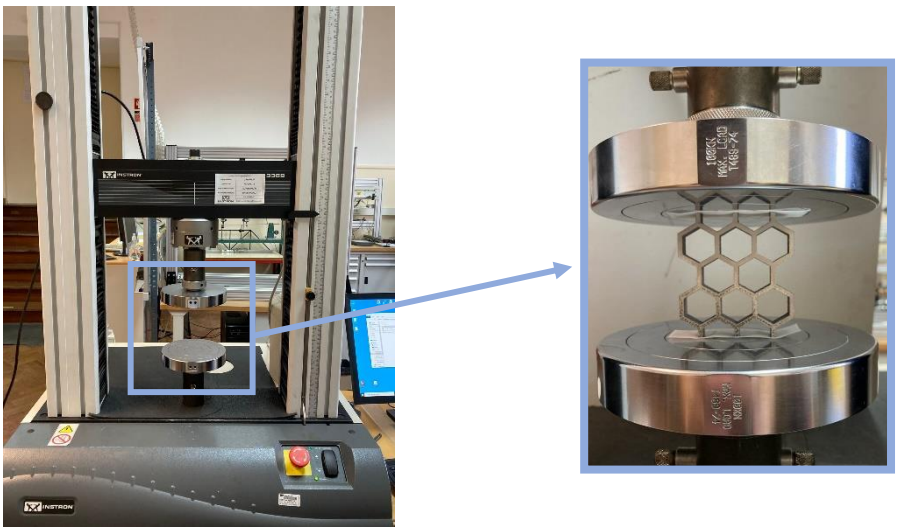

Figure 3.21: Compression testing machine apparatus (Instron 3369).

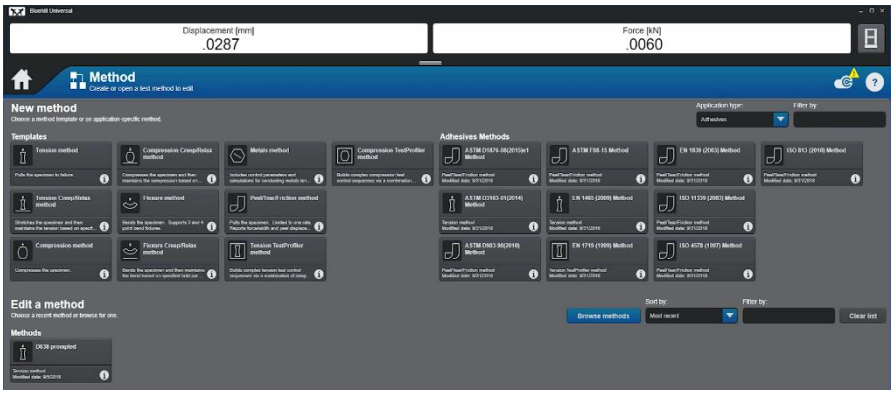

Figure 3.22: Instron Bluehill Universal software (initial set-up) [91].

Both out-of-plane and in-plane compression tests were performed with a constant displacement rate of 0.5mm/min, differing on the maximum displacement of the test. For the out-of-plane testing of regular honeycomb structures, the tests were terminated when the applied force was near 50kN, while in-plane testing was carried out until the plastic deformation suffered by the sample allowed for a clear understanding of the failure points, with a consequent acute reduction of applied force.

Regarding the graded structures, only in-plane testing was performed. The ending criterion utilized was identical to the one in regular structures. It is important to mention that not all graded structures were experimentally tested, instead selecting three designs out of the twelve designed: *2D*, *3A(-)* and *3B(+)*.

3.4.3 Data Processing and Sample Characterization

3.4.3.1 Data Processing

The software *Bluehill Universal* collected data on displacement and applied force on the samples, as a function of time. The file in which the data was exported was in the *.CSV* format, which was later converted into the format *.xlsx* when treated in *Microsoft Excel*. This data was utilized to create the force-displacement curve, used to obtain mechanical properties and characteristics of each sample, such as:

- Stiffness (K), obtained by ascertaining the slope of the elastic section of the force-displacement curve.
- Absorbed Energy (Ea), obtained by calculating the area below the force-displacement curve. The absorbed energy was calculated on a generic displacement value common for every geometry in out-of-plane testing (0.7mm) and in in-plane testing (1.5mm).
- Young's Modulus (E), according to the compression direction, obtained by ascertaining the slope of the elastic region section of the stress-strain curve. The stress-strain curve is obtained by dividing the applied force by the area where its being applied, and the displacement by the original length.

3.4.3.2 Failure Analysis

When tested in the in-plane orientation, the samples suffered permanent deformation. This deformation was observable in the form of cell wall bending and fracture, at times catastrophic. Therefore, and in order to develop a better insight regarding the failure mechanisms and behaviour of the honeycomb structures, the fracture surfaces and cracks were observed and photographed in the Laboratório de Ensaios Mecânicos e de Materiais (LEM^2) – DEM, Instituto Superior Técnico, using a stereomicroscope intended for low magnification observation. Using different magnifications, various fracture surfaces were observed and analysed, allowing also for a better understanding of the porosity level typical of samples processed via AM.

Chapter 4: Results and Discussion

The present chapter consists in the presentation and discussion of the numerical and experimental results that were obtained. Both the numerical and experimental data are to be presented via force-displacement plots, with the discussion focusing on the compressive behaviour of each different structure, and on mechanical and physical properties obtained via data treatment. A comparison is later performed between the numerical and experimental results, assessing the validation of the computational model. This comparison is further complemented with a matching of photographs of the deformed physical samples and images of the simulated samples. Finally, the failure and possible fracture of the cellular structures is observed via stereomicroscopy.

4.1 Introduction

Before the presentation of the results, some points regarding nomenclature and the numerical results are to be mentioned.

In order to simplify the designation of each type of test, some abbreviations were created. The out-of-plane numerical simulations were performed in both an elastic and an elastoplastic regime, even as experimental results showed a purely elastic behaviour for the displacements that were applied. Therefore, *numerical* (NUM) testing is divided into two subsections: *elastic* (EL) and *elastoplastic* (EP). Scenarios are also referred to as numerical elastic (NUM_EL) and numerical elastoplastic (NUM_EP). Regarding *experimental* testing, each scenario will be associated with the abbreviation (EXP).The samples referred to by the designations previously attributed in *Chapter 3.2.*

Due to the varying relative density ($\bar{\rho}$), the mechanical and physical properties obtained via the treatment of the results were normalized by this same relative density. Therefore, the presented properties are the *specific stiffness* ($\overline{K}$) and the *specific absorbed energy* ($\overline{E_a}$). Additionally, the *material's expected Young's Modulus* ($\bar{E}$), calculated in regular structures via the Equations 2.3 and 2.4, are also presented. This value could be helpful in evaluating the accuracy of the results, as it represents the value that should be the Young's modulus of the solid material ($E_S = 59000$MPa). For the geometries *L6H10*, *L8H10*, *L10H10*, *2D*, *3A(-)* and *3B(+)*, in which three samples were available, an average of the values is presented. The maximum von Mises stress ($\sigma_{M,max}$) is also presented regarding numerical results.

Finally, the out-of-plane simulations regarding sample *3C(-)* showed multiple numerical errors. It was assumed that, due to the very steep density gradient, the geometry might pose as somewhat problematic for the software to process.

4.2 Regular Structures

4.2.1 Out-of-Plane Compression

The resulting force-displacement plots for NUM_EL, NUM_EP and EXP are shown in Figure 4.1 (a-i), with samples grouped by cell wall length.

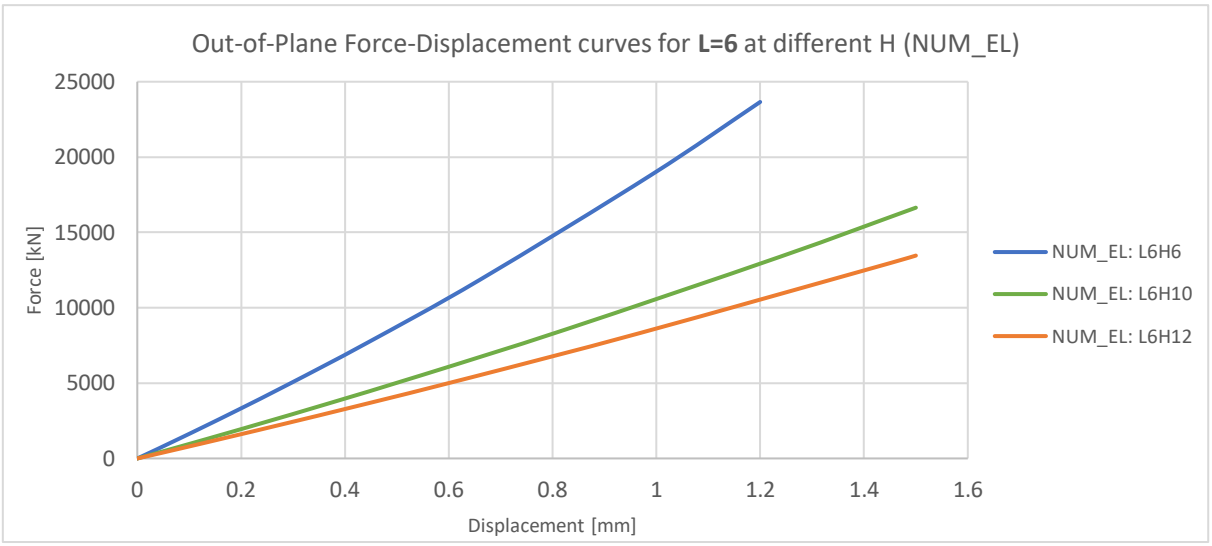
Out-of-Plane Force-Displacement curves for **L=6** at different H (NUM_EL)
Force [kN]
25000
20000
15000
10000
5000
0
0
0.2
0.4
0.6
0.8
1
1.2
1.4
1.6
Displacement [mm]
NUM_EL: L6H6
NUM_EL: L6H10
NUM_EL: L6H12

(a)

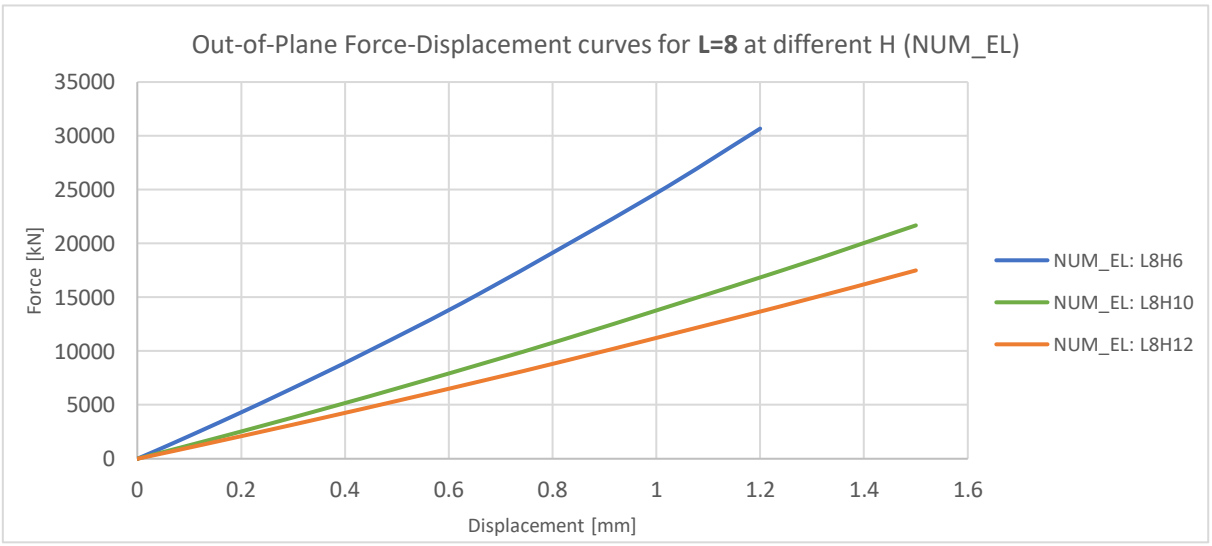
Out-of-Plane Force-Displacement curves for **L=8** at different H (NUM_EL)
Force [kN]
35000
30000
25000
20000
15000
10000
5000
0
0
0.2
0.4
0.6
0.8
1
1.2
1.4
1.6
Displacement [mm]
NUM_EL: L8H6
NUM_EL: L8H10
NUM_EL: L8H12

(b)

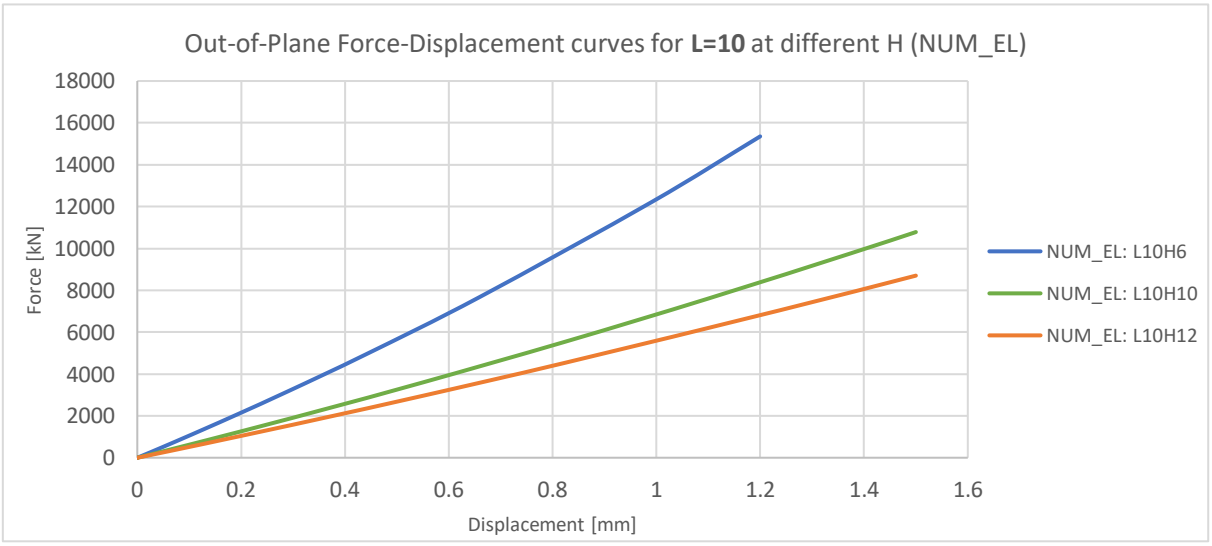
Out-of-Plane Force-Displacement curves for **L=10** at different H (NUM_EL)
Force [kN]
18000
16000
14000
12000
10000
8000
6000
4000
2000
0
0
0.2
0.4
0.6
0.8
1
1.2
1.4
1.6
Displacement [mm]
NUM_EL: L10H6
NUM_EL: L10H10
NUM_EL: L10H12

(c)

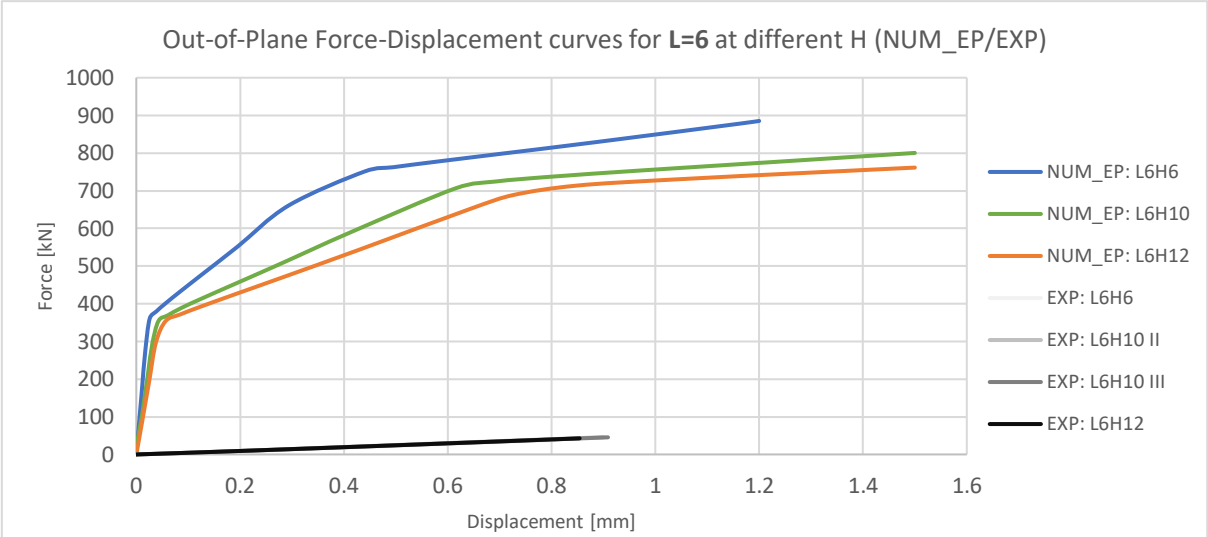
Out-of-Plane Force-Displacement curves for **L=6** at different H (NUM_EP/EXP)
Force [kN]
Displacement [mm]
NUM_EP: L6H6
NUM_EP: L6H10
NUM_EP: L6H12
EXP: L6H6
EXP: L6H10 II
EXP: L6H10 III
EXP: L6H12

(d)

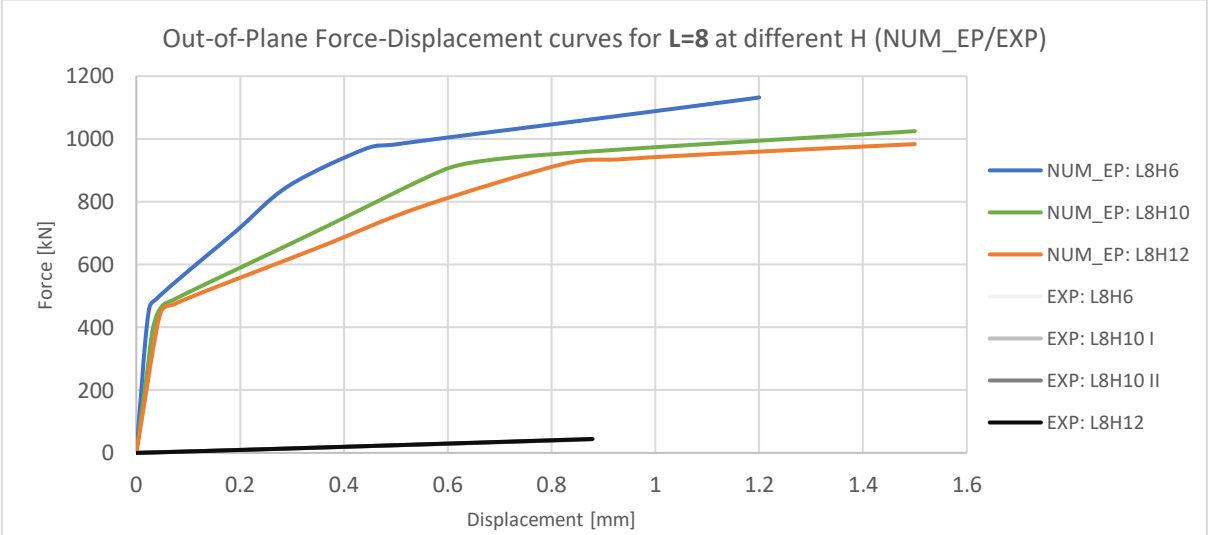
Out-of-Plane Force-Displacement curves for **L=8** at different H (NUM_EP/EXP)
Force [kN]
Displacement [mm]
NUM_EP: L8H6
NUM_EP: L8H10
NUM_EP: L8H12
EXP: L8H6
EXP: L8H10 I
EXP: L8H10 II
EXP: L8H12

(e)

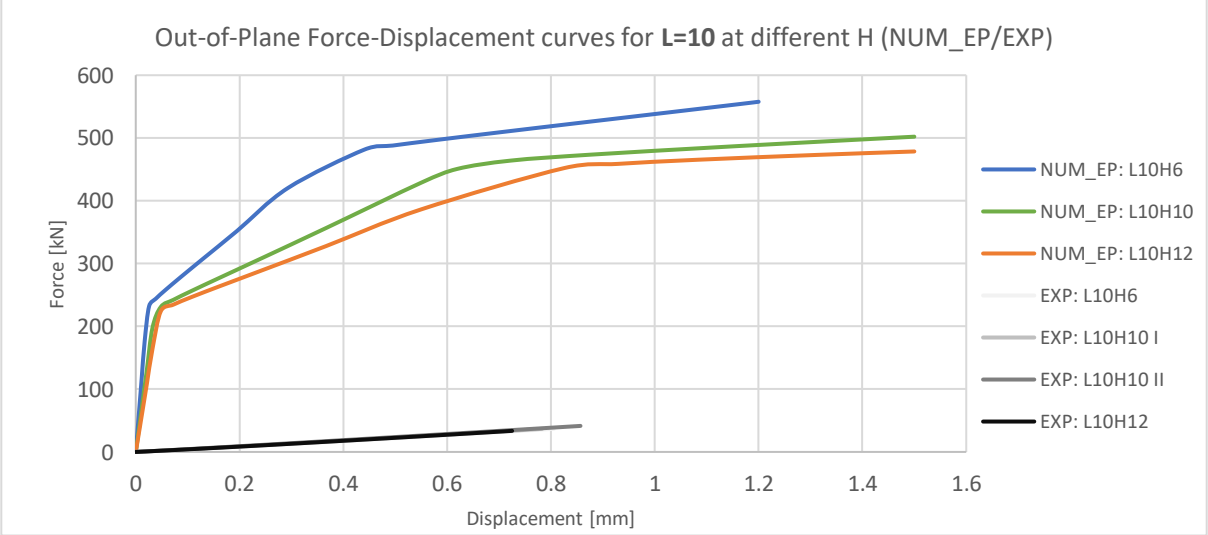
Out-of-Plane Force-Displacement curves for **L=10** at different H (NUM_EP/EXP)
Force [kN]
Displacement [mm]
NUM_EP: L10H6
NUM_EP: L10H10
NUM_EP: L10H12
EXP: L10H6
EXP: L10H10 I
EXP: L10H10 II
EXP: L10H12

(f)

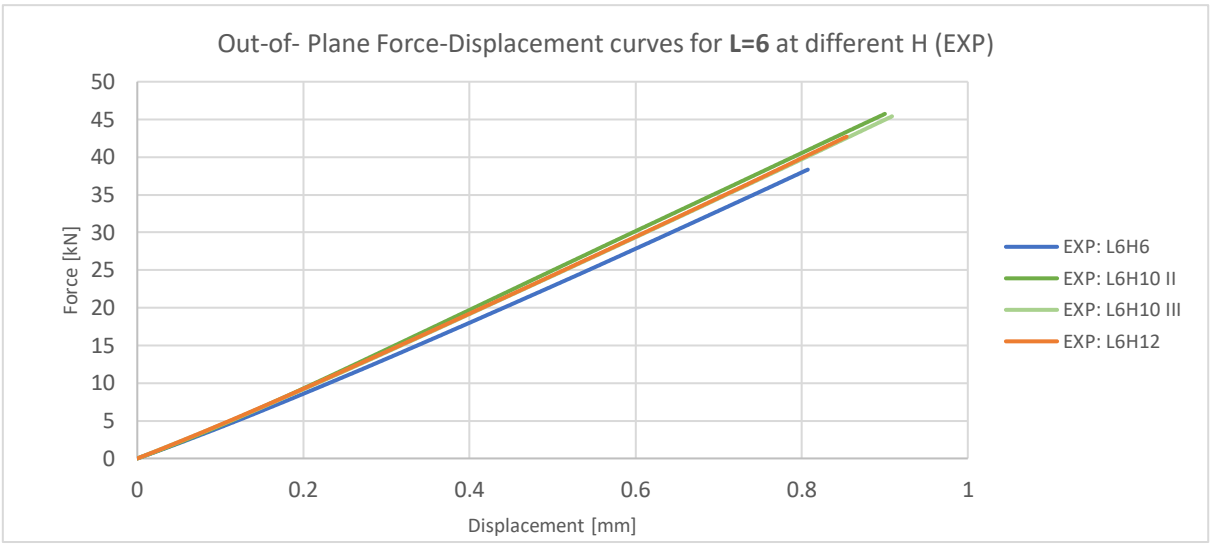

(g)

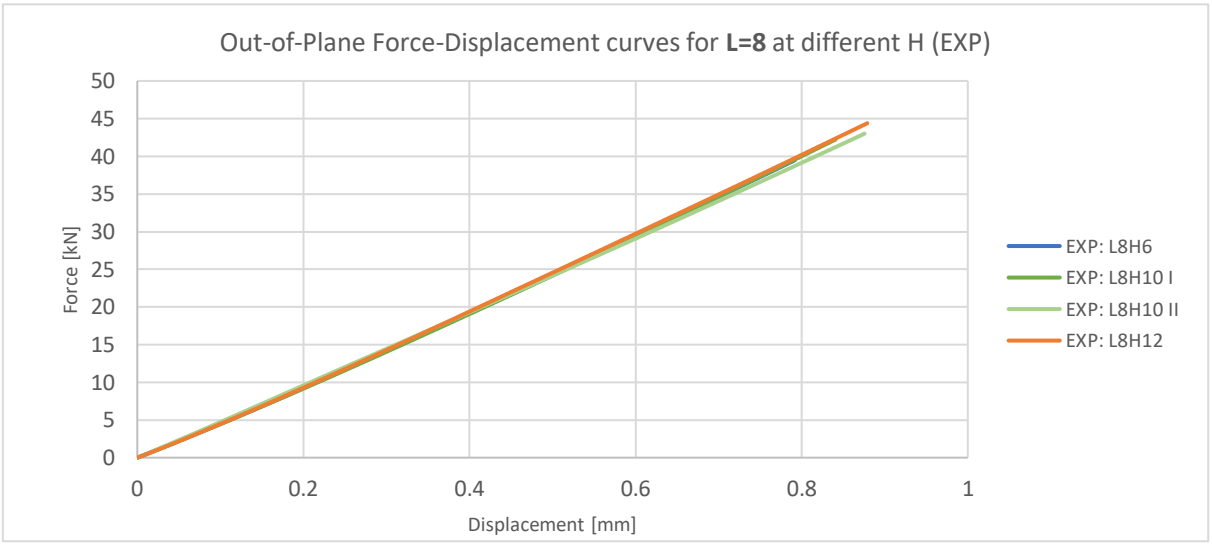

(h)

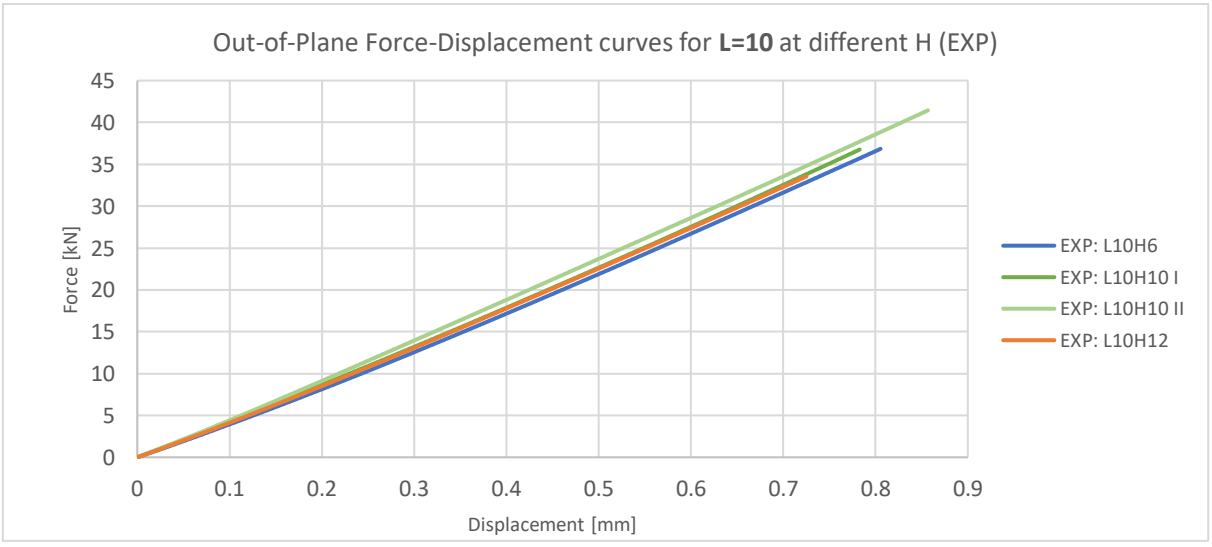

(i)

Figure 4.1: Out-of-Plane force-displacement curves at different heights for: NUM_EL: (a) L=6, (b) L=8, (c) L=10; NUM_EP: (d) L=6, (e) L=8, (f) L=10; EXP: (g) L=6, (h) L=8, (i) L=10.

A large disparity between numerical and experimental results can be denoted just from a simple observation. An expected variation in mechanical properties occurs with differing geometries in the data retrieved from the simulations, while the same not being observed in the experimental results. As seen further in Table 4.1, the values for specific stiffness, specific absorbed energy and expected Young's modulus are extremely lower than those obtained numerically, and from what would be expected. The problem had emerged in previous work [6], with possible causes being attributed to excess porosity or surface imperfections. Following this hypothesis, the surfaces were polished, with the problem persisting. This being said, it was concluded that internal porosity could not be the sole cause of the results discrepancy. It was then hypothesised that the software was recording the mechanical response of the machine apparatus instead of the honeycomb structures, or that the precision of the recorded data might not be appropriate. This said, the out-of-plane results obtained for regular structures cannot be deemed an accurate representation of the mechanical behaviour of the structures, with the majority of focus in the out-of-plane results being reflected on the numerical values. Some improvements regarding experimental testing will be suggested later on.

Table 4.1: Specific stiffness, specific absorbed energy and expected Young's Modulus for regular structures (out-of-plane numerical and experimental)

Code	$\bar{\rho}$	$\bar{K}$ [kN/mm]			$\overline{E_a}$ (at 0.7 mm) [J]			$\bar{E}$ [MPa]		
		NUM		EXP	NUM		EXP	NUM		EXP
		EL	EP		EL	EP		EL	EP	
L6H6	0.338	52668	47368	143.4	12791	1341	34.3	72755	65433	198
L6H10		30568	28679	152.7±1.9	7352	1127	36.4±0.3	70376	66028	352±5
L6H12		24183	23468	150.8	6053	1034	36.2	66812	64836	418
L8H6	0.269	82060	76164	186.2	20539	2139	44.7	70492	65427	160
L8H10		49224	45641	184.8±2.7	11861	1802	40.5±4.4	70475	65345	265±4
L8H12		40443	37841	189.2	9757	1658	45.3	69484	65013	323
L10H6	0.228	49974	44853	202.4	12137	1255	48.22	72050	64667	292
L10H10		29024	26799	209.9±3.5	6968	1052	50.6±0.9	69743	64397	505±9
L10H12		23828	22247	204.3	5741	967	49.1	68709	64151	589

Continuing the analysis, a clear pattern was identified regarding the influence of cell core height in the mechanical properties of the material, obtained numerically. As a trend, an increase in core height led to a constant decrease in both specific stiffness and specific absorbed energy.

The difference in stiffness can be attributed to the level of buckling occurring in the cell walls, with higher levels of elastic buckling being associated to longer structures. The decreasing rate in specific stiffness linked to largest variation of core height ($6mm \rightarrow 10mm$) is considerably higher than the one linked to the smaller increase ($10mm \rightarrow 12mm$), which might imply that steeper variations in core size give origin to higher variations in specific stiffness, while also suggesting the possibility of the existence of a critical core height at which specific stiffness starts stabilizing. This occurrence is better demonstrated in the charts in Figure 4.2 (a) and (b). This occurrence regarding the occurrence of buckling, which consequently affects stiffness, was explored by Zhang and Ashby [92]. A decrease in the expected Young's modulus with increasing cell core height is predominant throughout all regular geometries.

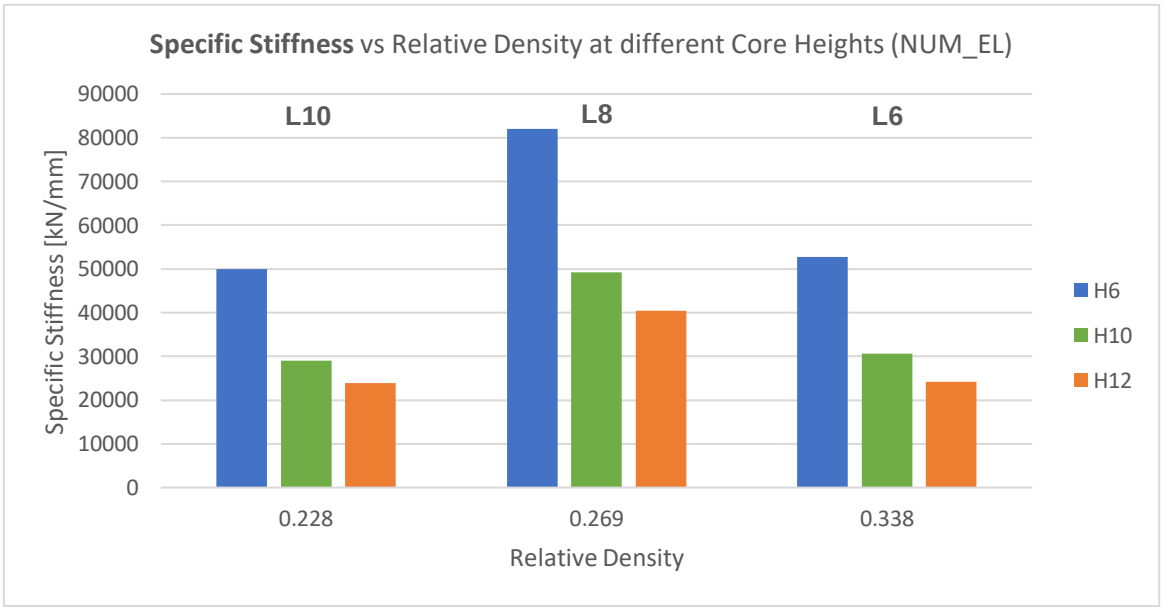

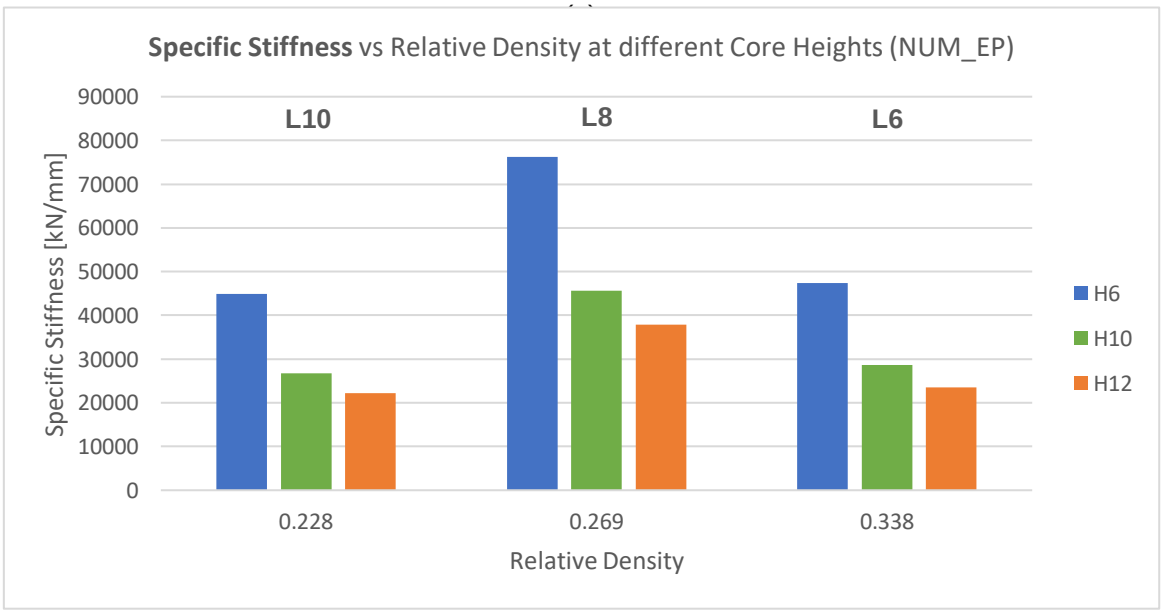

(b)

An assessment of the influence of cell wall length on the mechanical behaviour can be directly correlated to the relative density of the structure, as cell thickness is constant throughout all regular structures. This being said, and after observing the presented results, no immediate pattern can be associated to the effect of relative density in the mechanical response of the structures. On the other hand, when the charts presented in Figure 4.2 are altered to display the results regarding the apparent area (size) of the structures (Figure 4.3), a pattern emerges. As the apparent area is progressively increased, so does the specific stiffness of the structures. This correlation can also be extended to the degree at which the apparent area is increased, with a minimal variation in specific stiffness being associated to the smaller area variation between sample groups L10 and L6, while the variation between sample groups L6 and L8 is much more pronounced (an approximate increase of 4% in apparent area compared to an increase in 61%, respectively).

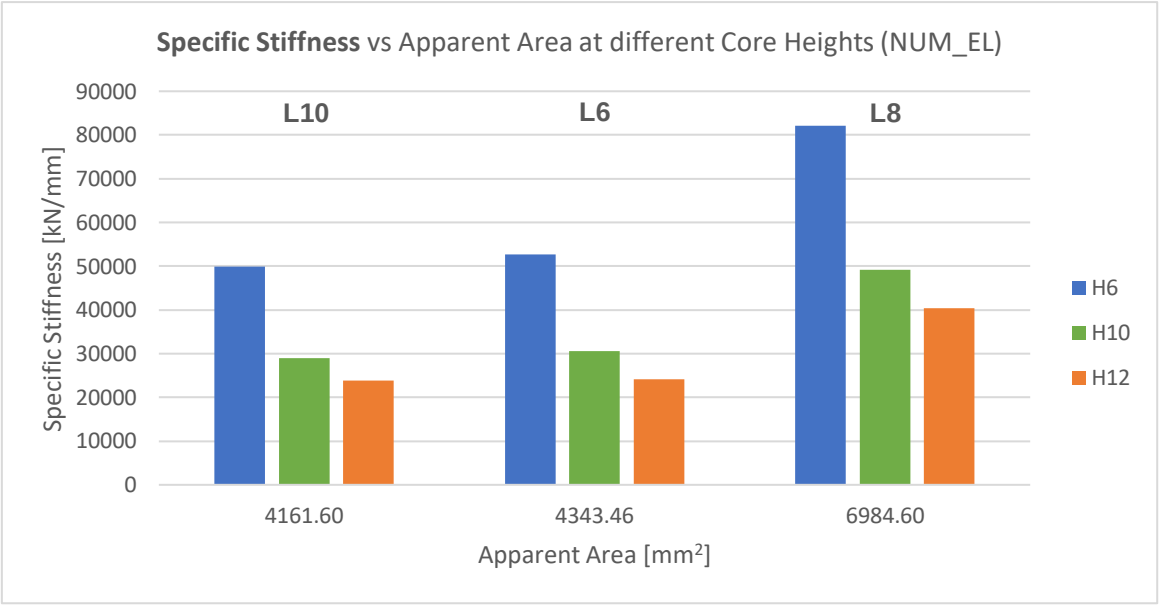

(a)

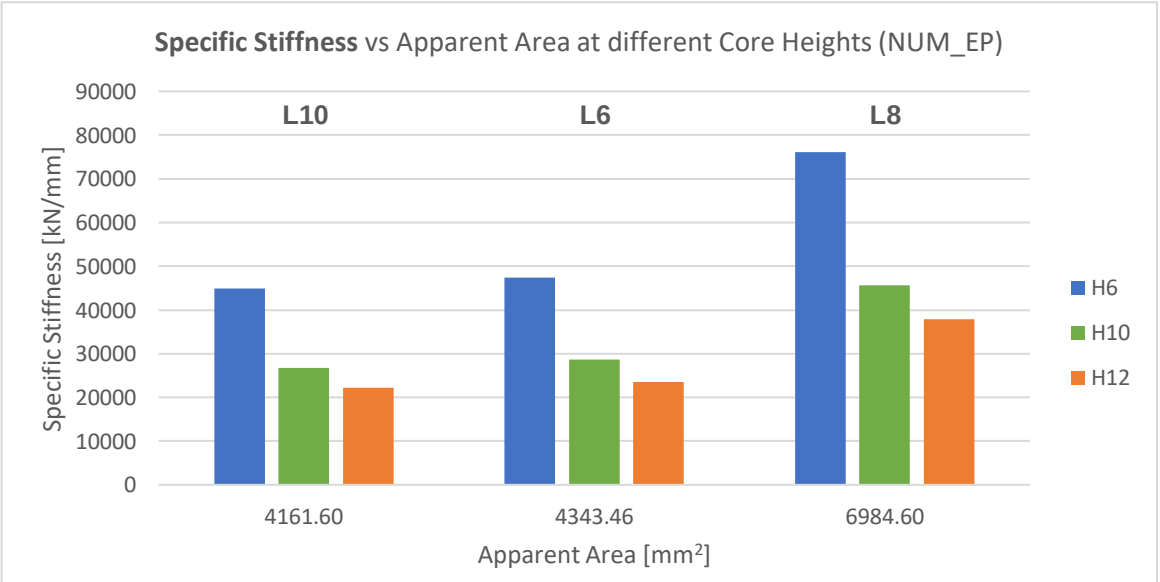

Figure 4.3: Specific stiffness vs apparent area at different cell core heights and length: (a) NUM_EL; (b) NUM_EP (Out-of-Plane)

The charts presented in Figures 4.2 and 4.3 regarding specific absorbed energy follow the same pattern, with increasing apparent area showcasing an increase in the energy absorbed by the structures. These charts can be found in Appendix D.

The software ABAQUS allows the user to assess if a given structure yields under the imposed boundary conditions. For most metals, this assessment is performed via the von Mises criterion, which states that a given material will yield if the von Mises stress is equal or greater than the yield stress (σ_y) of the same material. Having submitted the true yield stress of the material to the software ($\sigma_{y,R} = 212MPa$) and requesting the maximum von Mises stress ($\sigma_{M,max}$) in each elastoplastic simulation (Table 4.2), it was verified if the structures were yielding under the load, and in which manner.

Table 4.2: Maximum von Mises stress recorded for the regular structures (out-of-plane)

Code	$\sigma_{y,R}$ $[MPa]$	$\sigma_{M,max}$ $[MPa]$
L6H6	212	536.5
L6H10		525.3
L6H12		496.0
L8H6		552.3
L8H10		539.1
L8H12		544.7
L10H6		536.4
L10H10		515.6
L10H12		518.7

The values presented in Table 4.2 showed that every structure yielded when submitted to the applied load, as was concluded from the force-displacement plots previously analysed. A closer look on a typical deformed honeycomb structure (Figure 4.4) indicates that, to be precise, not the entire structure had yet yielded, with some small zones with maximum von Mises stress still below the yielding stress.

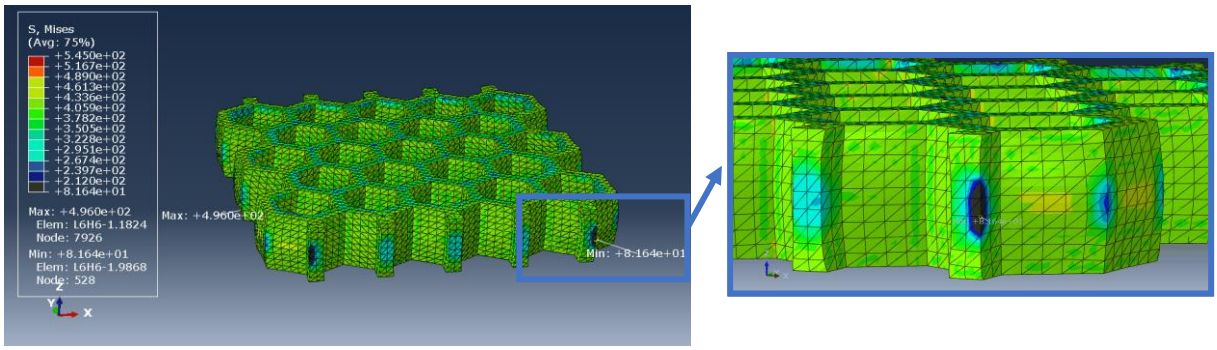

Figure 4.4: Illustration of the von Mises stress distribution in the deformed sample L6H6 (out-of-plane), showcasing a region which has not yet yielded (region in black).

Concerning the experimental results, the observed patterns were much different from those observed in the numerical results. Due to the immense discrepancy between experimental and numerical data, as well as the experimental results being far lower than expected, the depth with which they are analysed was lower. Contrary to what was concluded for the numerical results, no direct pattern was found between the mechanical and physical properties of the structures and their apparent area. Instead, a relative correlation with relative density was identified, as observed in Figure 4.5.

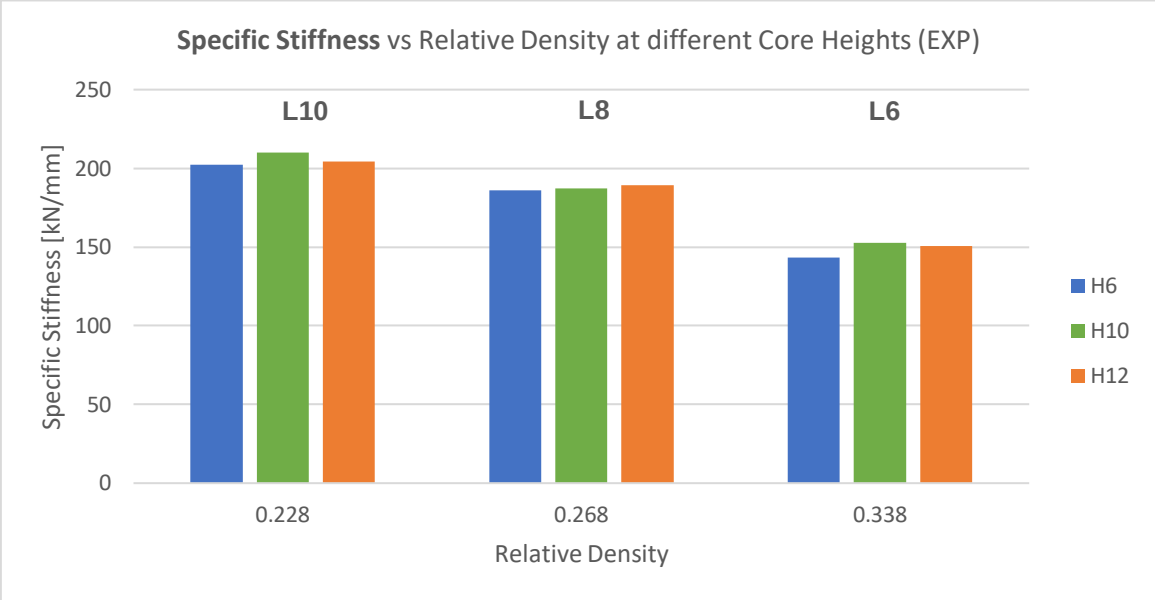

Figure 4.5: Specific stiffness vs relative density at different cell core heights and lengths (out-of-plane EXP)

As previously mentioned, due to the irregularities associated with the out-of-plane experimental results recorded for the regular structures, no clear conclusions could be taken. The remaining charts regarding the out-of-plane mechanical behaviour of experimental samples can be found in Appendix D.

Comparing the elastic and elastoplastic models, a slight variation in specific stiffness was recorded, which could be attributed to local plastic deformation on the interface between the upper compression plate and the structure, as well as numerical errors due to the superior complexity of the model. Regarding the specific absorbed energy, a clear separation was verified. Even though the absorbed energy in elastoplastic regimes can be high due to various mechanisms (e.g., energy dissipation consequent of permanent deformation), superior energy absorption was identified in the elastic regime. Ultimately, the most accurate model would be the elastoplastic, due to the ductility of the aluminium alloy, with plasticity being expected from the tested samples.. Furthermore, the values obtained for the expected Young's modulus in the elastoplastic model were closer to the solid material's Young modulus (59000MPa).

4.2.2 In-Plane Compression

The force-displacement curves resulting from the in-plane compression of regular structures, with different cell length and constant core height (H = 10mm), show closer results regarding the approximation of the computational model to the physical data, as presented in Figure 4.6 (a-d). The mechanical and physical properties calculated from these curves are presented in Table 4.3.

Table 4.3: Specific stiffness, specific absorbed energy, expected Young's modulus and maximum von Mises stresses for the regular structures (in-plane numerical and experimental)

Code	$\overline{\rho}$	$\overline{K}$ $[kN/mm]$		$\overline{E_a}$ (at 1.5 mm) $[J]$		$\overline{E}$ $[GPa]$		$\sigma_{M,max}$ $[MPa]$
		NUM	EXP	NUM	EXP	NUM	EXP	NUM
L6H10	0.338	108.6	48.8	63.9	44.3	27585	12564	508.4
L8H10	0.269	70.7	38.9	50.8	36.1	34599	19027	507.8
L10H10	0.228	40.1	25.8	27.9	21.1	35699	22921	528.7

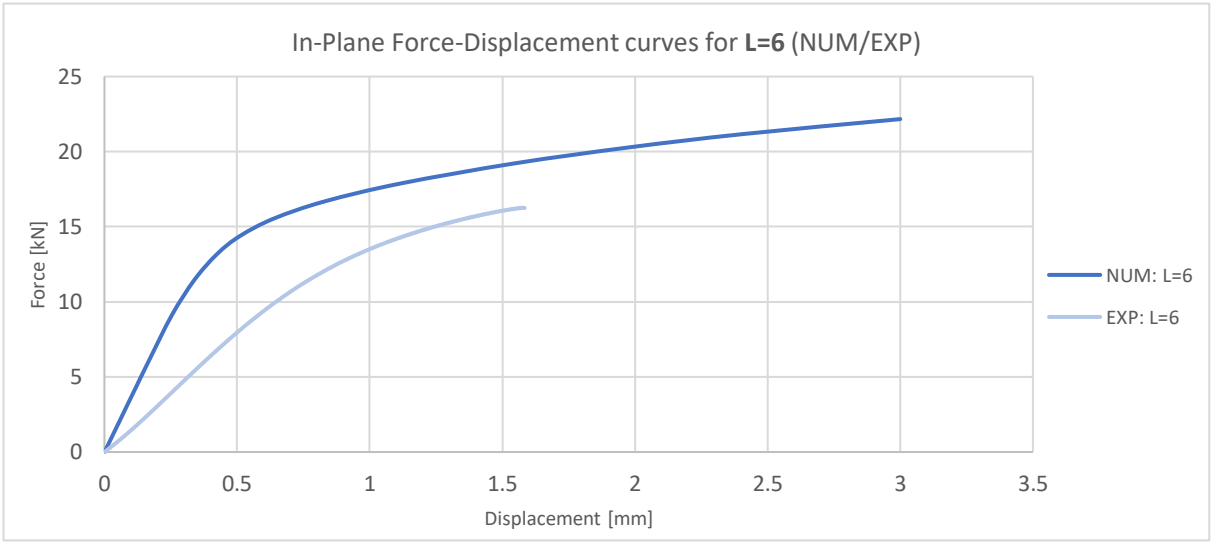

(a)

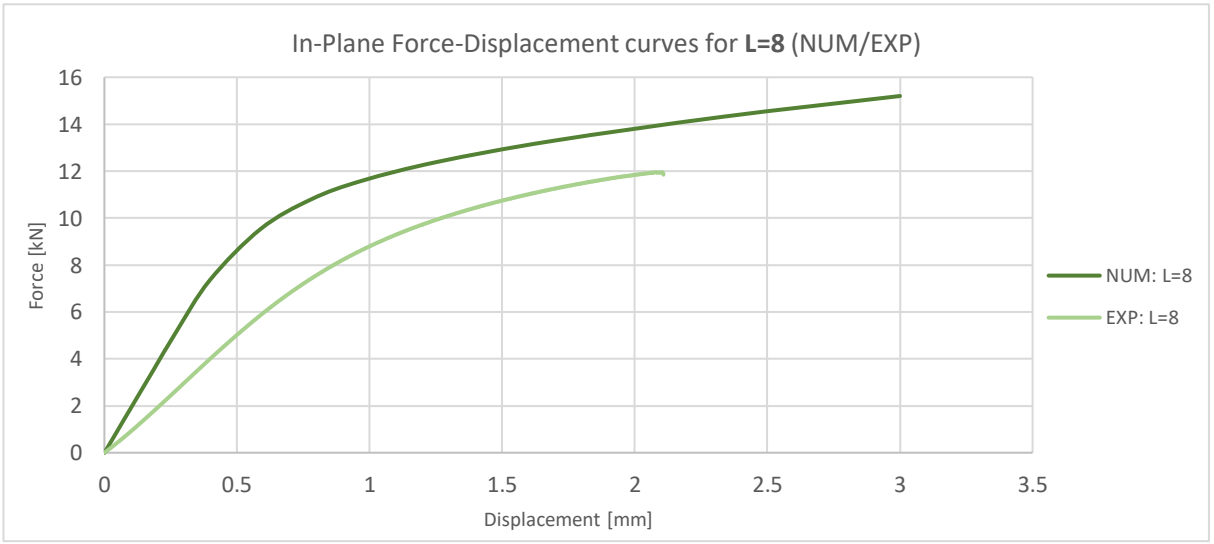

(b)

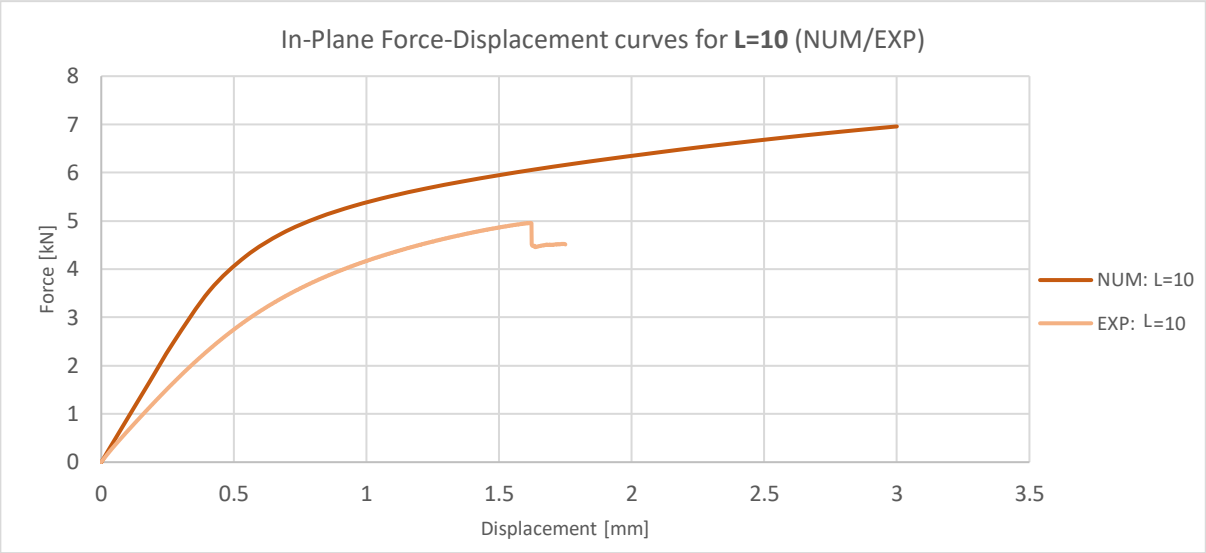

(c)

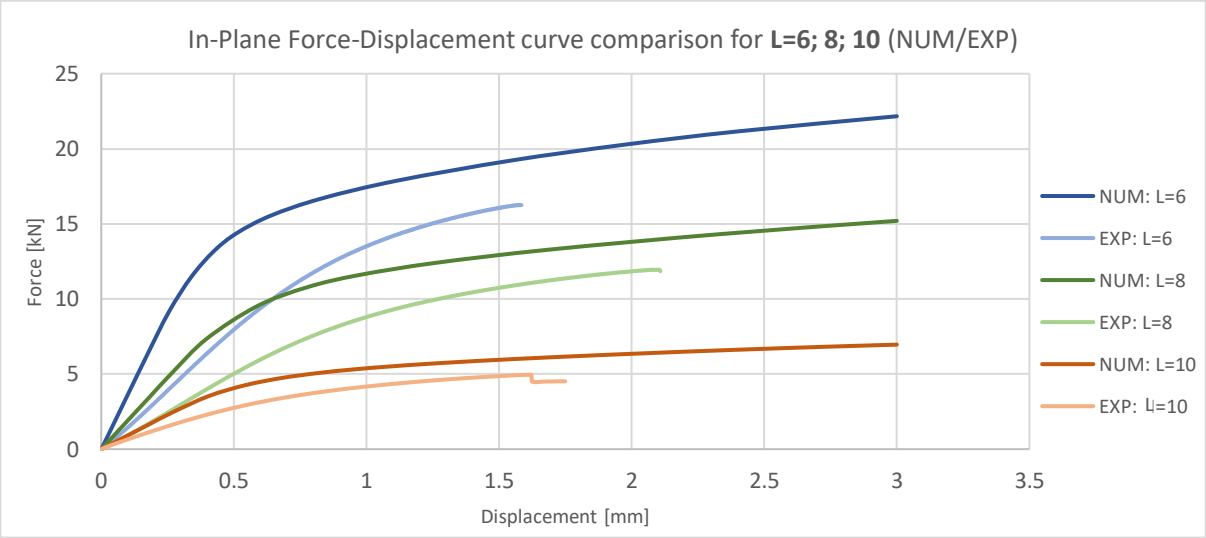

(d)

Figure 4.6: In-plane numerical and experimental force-displacement curves at different lengths for: (a) L=6; (b) L=8; (c) L=10; (d) L=6, 8, 10.

As expected, the values for specific stiffness, specific absorbed energy and the expected Young's modulus were much lower than those recorded in out-of-plane testing. This goes appropriately in context with the Gibson and Ashby [7] regarding the differences between out-of-plane and in-plane mechanical properties of cellular structures, with the latter orientation demonstrating lower results due to its deformation mechanisms. Contrary to the out-of-plane results, a trend can be delineated regarding the structure's in-plane properties and its relative density. This trend is further presented in Figure 4.7, with an increase in both specific stiffness and specific absorbed energy with increasing relative density in both numerical and experimental results. This trend once again goes accordingly to the studies of Gibson and Ashby [7], as higher values for relative density (i.e., lower values for cell length) can be correlated to a thickening of cell walls, offering a higher resistance to buckling and collapse of the cell walls, consequently meaning an increase in stiffness.

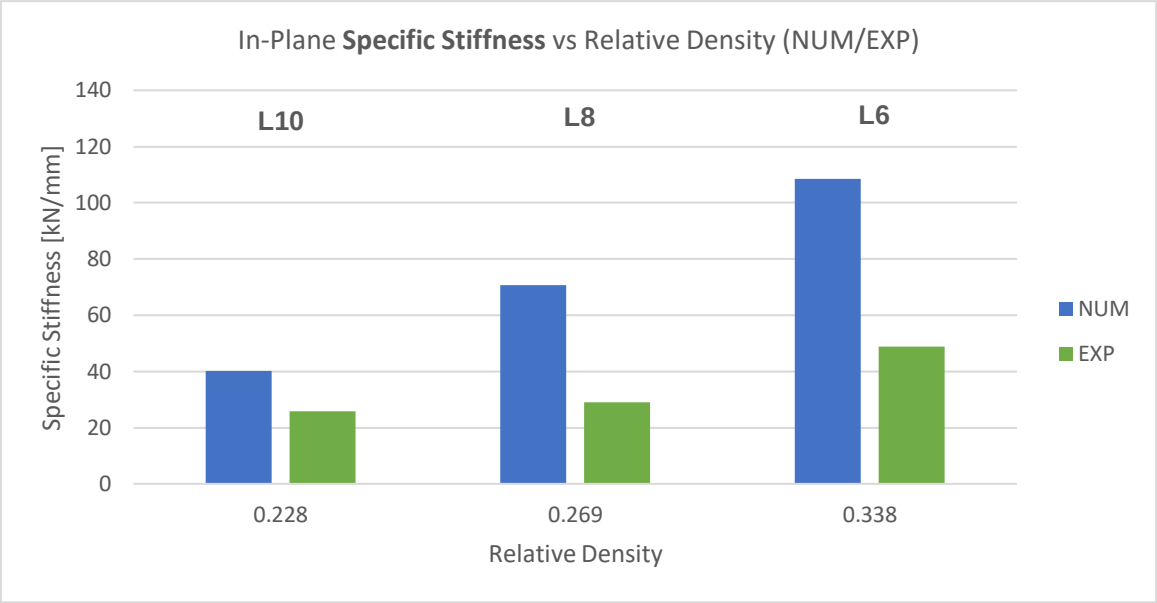

(a)

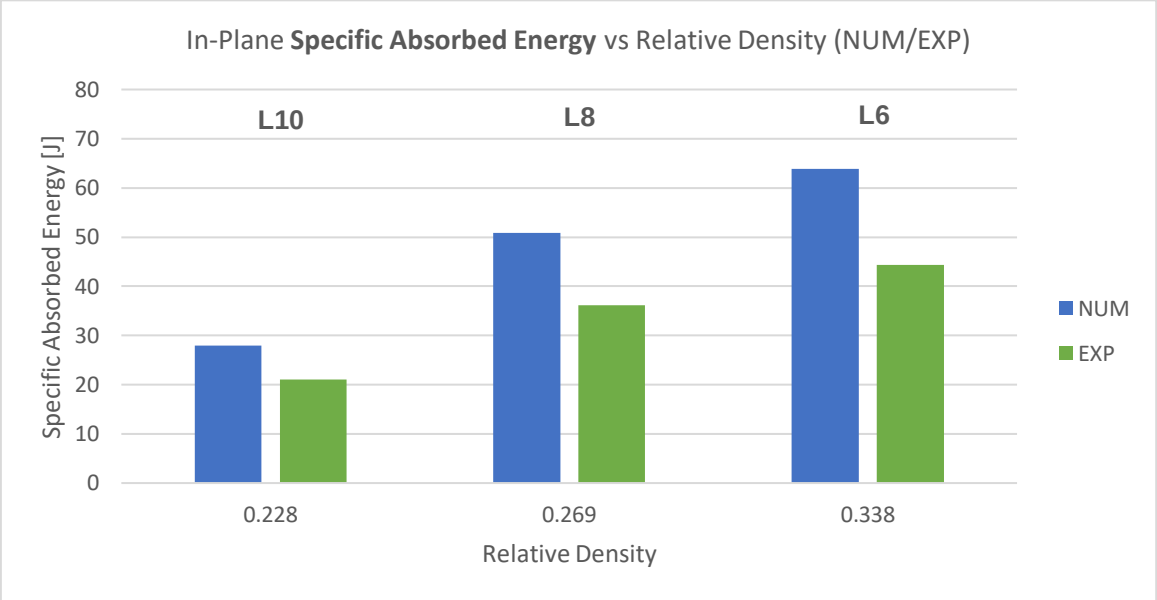

(b)

Figure 4.7: (a) In-plane specific stiffness vs relative density at different cell lengths (NUM/EXP); (b) In-plane specific absorbed energy vs relative density at different cell lengths (NUM/EXP)

When applying the same analysis to the effect of apparent area to the results, no pattern is identifiable. Even though the obtained results are as expected, as similarities are viewed when comparing between the present force-displacement curves and the theoretical behaviour for in-plane compressing of metallic cellular structures described in chapter 2.2.2, the displacement imposed on the structures might not be sufficient. The in-plane compression of cellular structures presents an initial purely elastic stage, which was observed, followed by a section of plastic deformation at which the stress-strain remains somewhat stable, reaching a plateau, and a final point of densification in which the cell walls are being compressed against each other due to the high displacement.

This second stage was observed in the numerical curves, showing a levelling of the applied force with increasing displacement, further corroborated by the fact the maximum von Mises stresses presented in Table 4.3 being higher than that of the yield stress, revealing yield of the material. On the other hand, experimental curves only partially demonstrated this behaviour. As force began to reach a plateau value, certain areas of the structure would begin to fail in a more brittle manner, even reaching the point of earlier catastrophic failure in certain cases (e.g., L6H10 structure (Figure 4.8)). This premature failure might be attributed to imperfections resulting from the manufacturing of the structure, which act as stress concentrators. Although there was a slight mismatch between the numerical and experimental curves, comparing the deformation of the simulated and experimental structures ensured the accuracy of the designed model, as plastic deformation was relatively concentrated in the same regions (Figure 4.9 (a-c)).

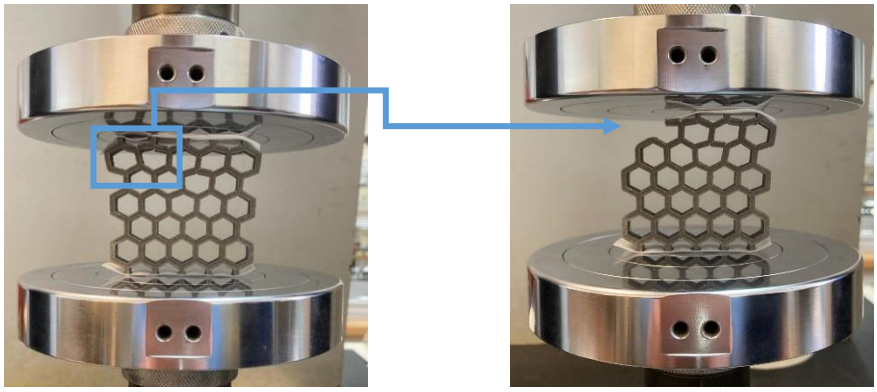

Figure 4.8: Experimental in-plane failure of sample L6H10

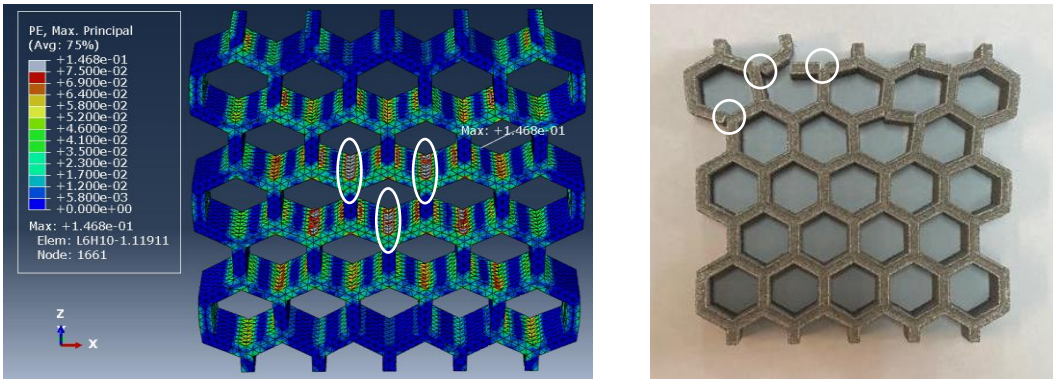

(a)

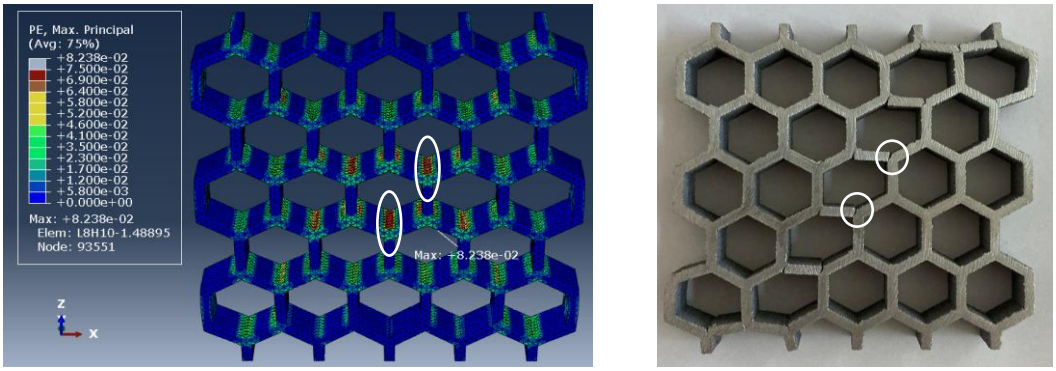

(b)

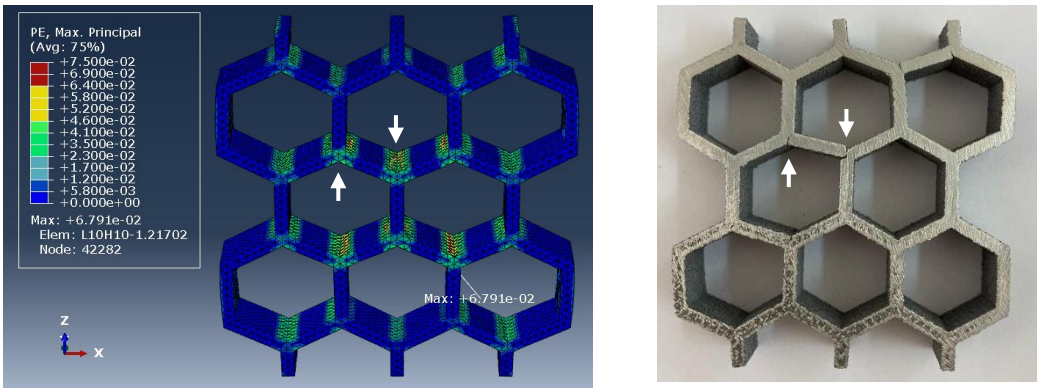

(c)

Figure 4.9: In-plane simulated (maximum plastic strain, PE) and experimental deformed samples, respectively, for: (a) L6H10; (b) L8H10; (c) L10H10.

Figure 4.9 (a) presents the in-plane deformation for the numerical and experimental L6 samples, with the failure in the experimental sample occurring in a region (top-left) in which the recorded plastic strain is higher than the maximum plastic strain submitted to the software, which indicates fracture. The deformation is concentrated in the triple junctions of the structures, which is where it should theoretically be concentrated. The deformation in the numerical case is concentrated in the middle section, which is not observed in the experimental case. In the case of the L8 samples (b), the deformation is once again matching to a relatively good degree, with failure occurring in the triple junctions. It might seem at first that the numerical maximum plastic strain is in the opposite side of the structure when compared to the experimental one, but the existence of symmetry shows the deformation applied to the entirety of the model. As seen in most experimentally tested samples, the deformation is concentrated in a specific region (e.g., top-half, along one axis) instead of the total structure. The model is further corroborated by the L10 results, as the numerical results show the maximum plastic strain recorded in the simulation is lower than the fracture plastic strain submitted in the model (0.06791<0.07) and no clear fracture can be identified in the experimentally tested sample.

4.3 Graded Structures

Due to the high number of different structures, and additional poor results regarding the experimental out-of-plane compression of the regular structures, the experimental compression of graded structures was only performed in the in-plane direction and of three different structures (*2D*, *3A(-)* and *3B(+)*). The totality of structures was numerically tested both out-of-plane and in-plane, except for the out-of-plane numerical results for the *3C(+)* structure, which constantly displayed errors during simulations.

4.3.1 Out-of-Plane Compression

The force-displacement curves obtained numerically are presented in Figure 4.10, grouped by the type of gradient which was utilized in the designing of said structure (gradient groups *1*, *2* and *3*, respectively). The comparison is performed firstly inside each group, aided by the mechanical and physical properties calculated from the same curves, as presented in Table 4.5, and between groups later. A first look on the curves showed the same behavioural trend as in regular structures, with the elastoplastic curves being comprised of an initial elastic section, followed by yield and some degree of plastic deformation.

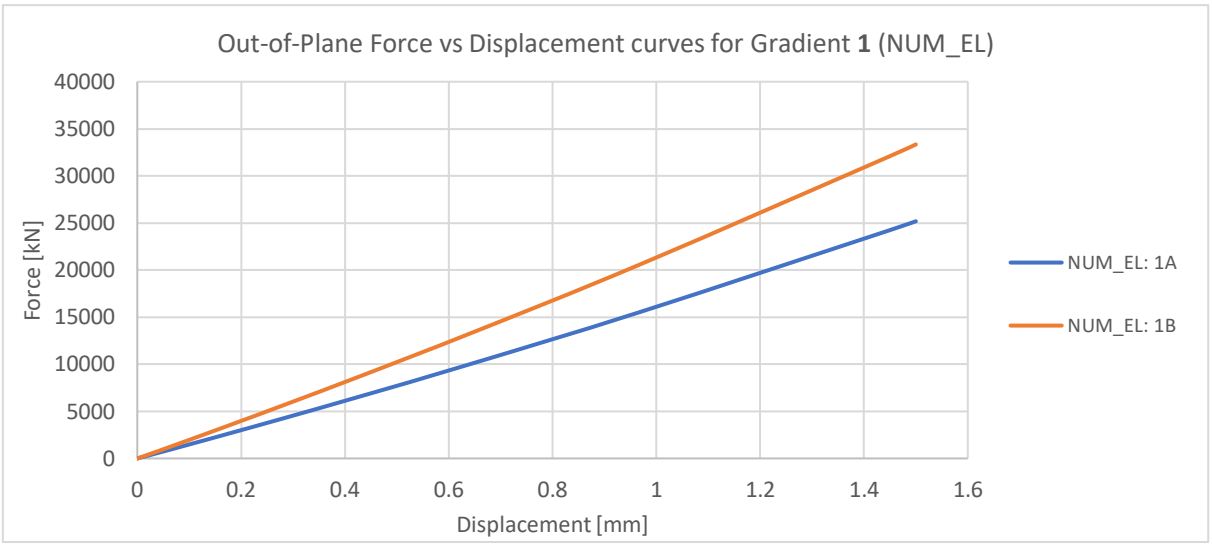
Out-of-Plane Force vs Displacement curves for Gradient 1 (NUM_EL)
Force [kN]
40000
35000
30000
25000
20000
15000
10000
5000
0
0
0.2
0.4
0.6
0.8
1
1.2
1.4
1.6
Displacement [mm]
NUM_EL: 1A
NUM_EL: 1B

(a)

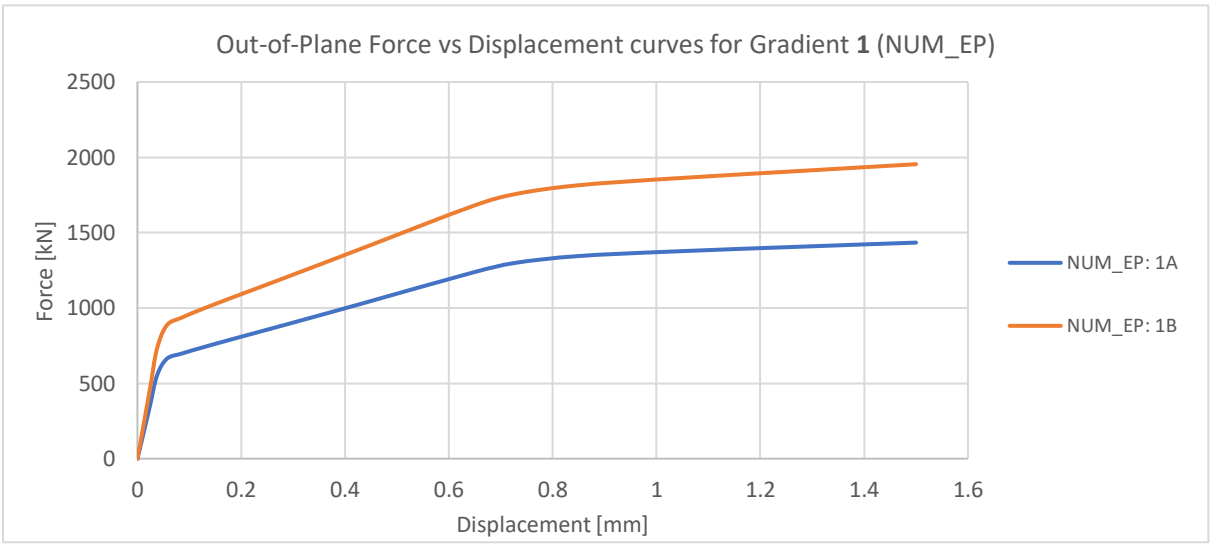
Out-of-Plane Force vs Displacement curves for Gradient 1 (NUM_EP)
Force [kN]
2500
2000
1500
1000
500
0
0
0.2
0.4
0.6
0.8
1
1.2
1.4
1.6
Displacement [mm]
NUM_EP: 1A
NUM_EP: 1B

(b)

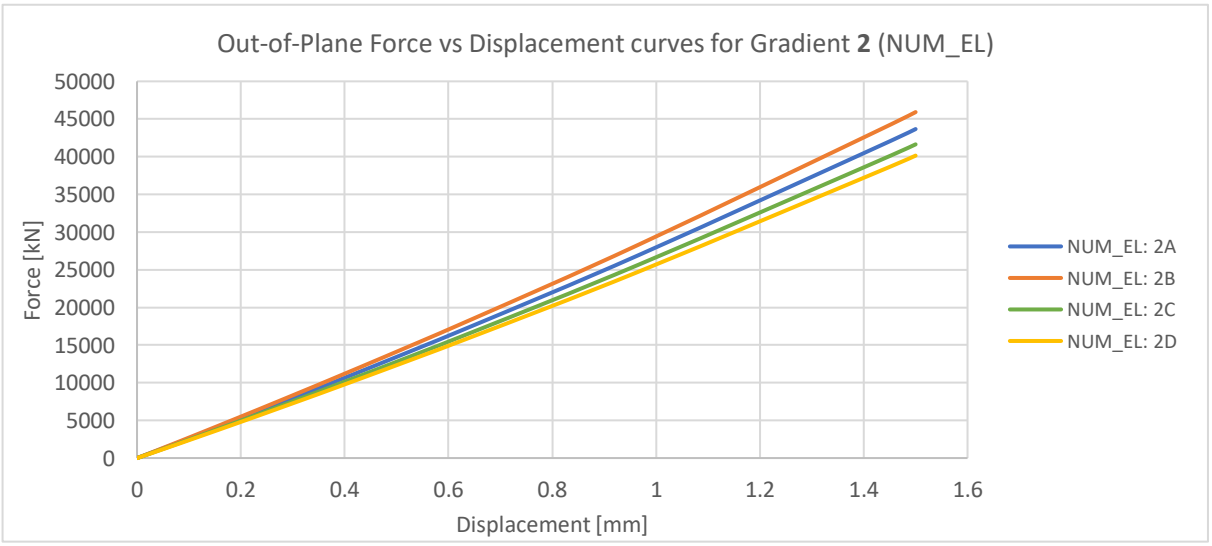
Out-of-Plane Force vs Displacement curves for Gradient 2 (NUM_EL)
Force [kN]
50000
45000
40000
35000
30000
25000
20000
15000
10000
5000
0
0
0.2
0.4
0.6
0.8
1
1.2
1.4
1.6
Displacement [mm]
NUM_EL: 2A
NUM_EL: 2B
NUM_EL: 2C
NUM_EL: 2D

(c)

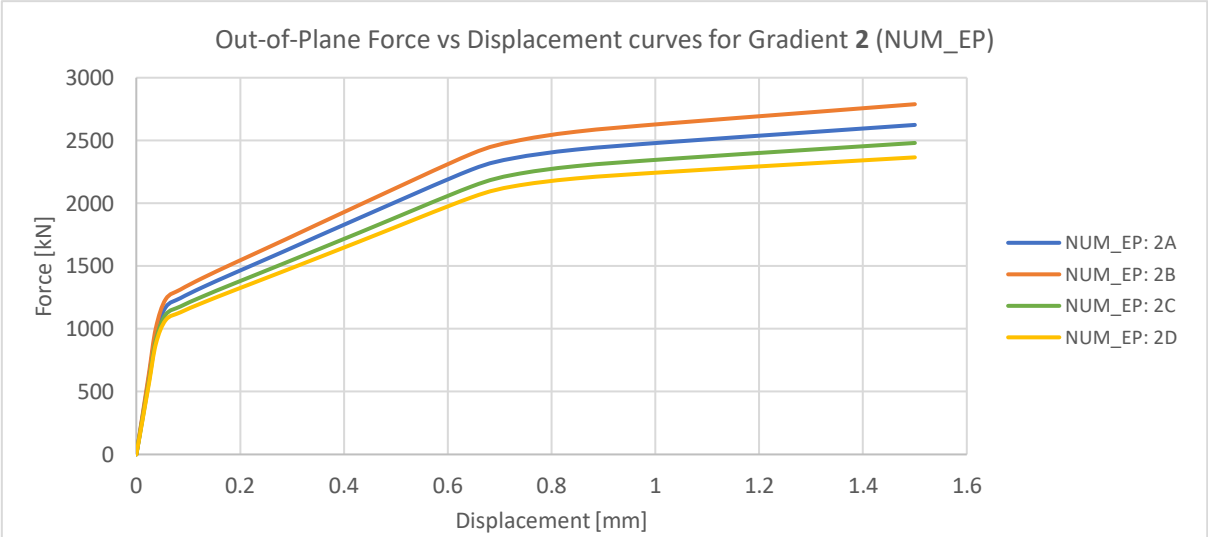

(d)

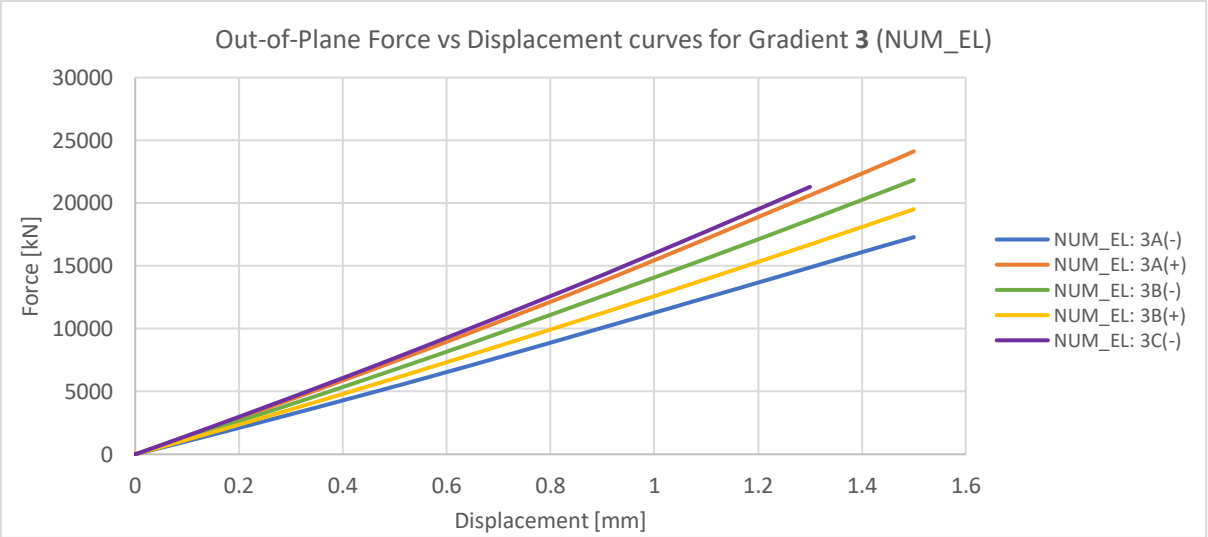

(e)

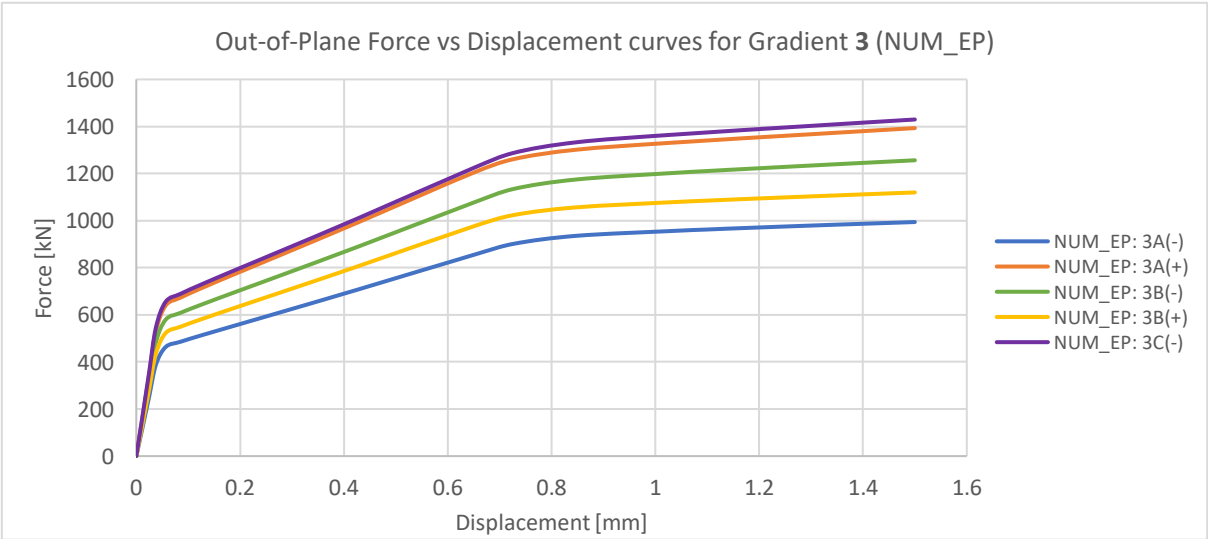

(f)

Figure 4.10: Out-of-plane force-displacement curves for structures of different gradient type: Gradient 1 (a) NUM_EL, (b) NUM_EP; Gradient 2 (c) NUM_EL, (d) NUM_EP; Gradient 3 (e) NUM_EL, (f) NUM_EP.

Table 4.5: Specific stiffness, specific absorbed energy, expected Young's modulus and maximum von Mises stress for graded structures (numerical out-of-plane).

CODE	$\bar{\rho}$	$\bar{K}$ [kN/mm]		$\overline{E_a}$ (at 0.7 mm) [J]		$\bar{E}$ [GPa]		$\sigma_{M,max}$ [MPa]
		NUM		NUM		NUM		NUM
		EL	EP	EL	EP	EL	EP	EP
1A	0.322	49003	45173	23979	2019	70	65	672.1
1B	0.421	49856	45833	24396	2096	71	66	519.0
2A	0.443	62060	57147	30369	2680	73	67	486.4
2B	0.466	61954	56886	30317	2685	73	67	491.8
2C	0.426	61365	56385	30029	2619	72	66	491.3
2D	0.410	61504	56651	30097	2613	72	66	505.6
3A(+)	0.323	46961	43359	22980	1954	71	65	733.8
3A(-)	0.240	47765	42645	23338	1879	72	64	567.6
3B(+)	0.265	46672	43242	22840	1933	70	65	626.4
3B(-)	0.298	48094	42843	23495	1903	72	64	533.9
3C(+)	0.199	---	---	---	---	---	---	---
3C(-)	0.335	47945	42960	23440	1919	72	65	633.7

Starting with the samples from gradient group *1*, no considerable variation was identified. The values for specific stiffness and specific absorbed energy did not show a great disparity between samples, with sample *1A* exhibiting lower values. In the present case, sample *1B*'s higher values might be attributed to its higher relative density. Regarding gradient group *2*, little variation was once again seen, as the structures are very similar. Finally, due to existence of steeper gradients, gradient group *3* was the one in which larger differences were identifiable. Samples showcasing a decrease in density from the centre to the exterior, more specifically *3A(-)*, *3B(-)* and *3C(-)*, presented higher values for specific stiffness and specific absorbed energy in comparison to their counterparts in the purely elastic scenario. When simulated in an elastoplastic scenario, the pattern inverts, with *3A(+)*, *3B(+)* and *3C(+)* presenting better energy absorption and stiffness.

Regarding the expected Young's modulus, the values were coincidental with those of the previously analysed regular structures, meaning the model is consistent. The expected value in the elastoplastic scenarios was closer to the Young's modulus of the solid material submitted to the software (59000MPa), which indicates this is the model closer to reality. The maximum von Mises stresses indicate every graded structure would yield when submitted to the applied load consequent of the imposed displacement in the present model. Although some plastic deformation would be expected, the values were considerably high, which might be due to the software assuming the structures as "perfect" with no level of defects, as in reality the structures present some level of porosity and inclusions.

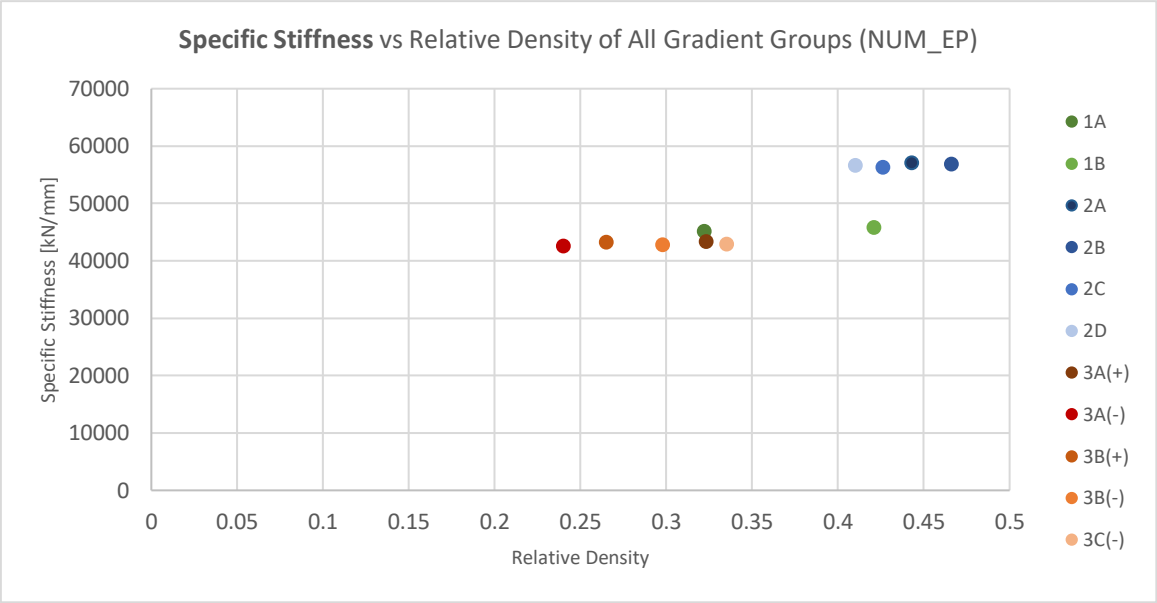

(a)

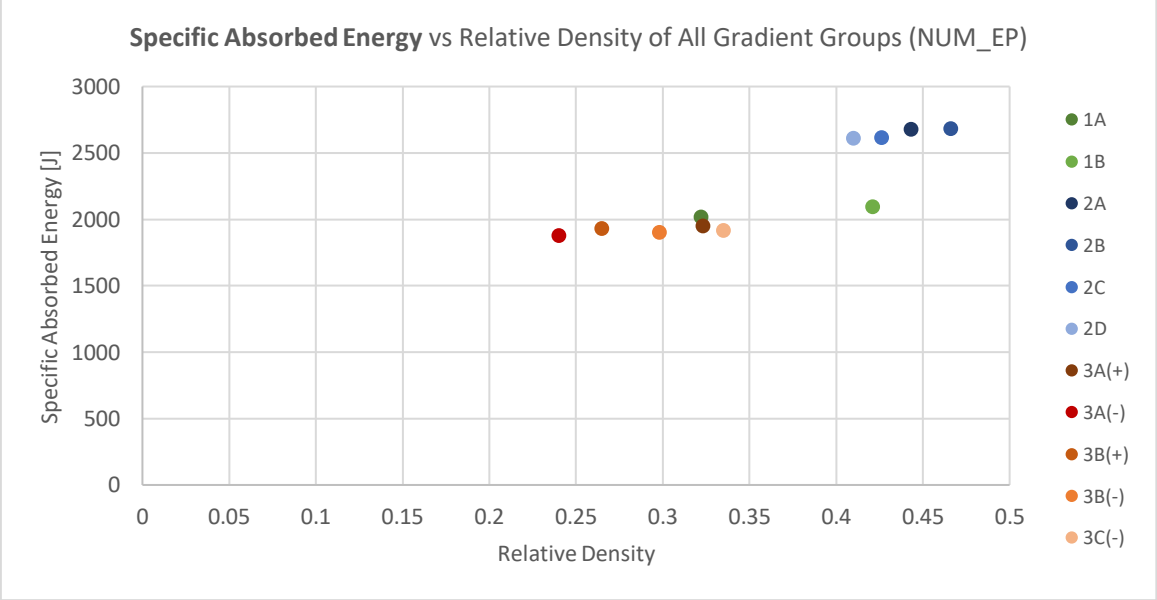

(b)

Figure 4.11: (a) Specific stiffness vs relative density for all gradient groups (NUM_EP); (b) Specific absorbed energy vs relative density for all gradient groups (NUM_EP)

The following step was to compare the mechanical properties between gradient groups and their defining geometric parameters. With this intent, the values for specific stiffness and specific absorbed energy were compiled in the plots presented in Figure 4.11, with samples from the same gradient group being attributed similar colours: green for gradient *1*, blue for gradient *2* and red for gradient *3*. A first observation of the plots would suggest there was a strong increase in stiffness and energy absorption from around a relative density of *0.4*, with the samples from gradient group *2* presenting values between *30%-35%* higher than the remaining groups. And although the increase was not as notable in sample *1B*, which presented the largest relative density between gradient groups *1* and *3*, it was the one with better mechanical performance. Even so, a clear correlation could not be established regarding relative density, as an increase in this parameter showed little impact in the mechanical properties of the analysed samples (excluding gradient group 2).

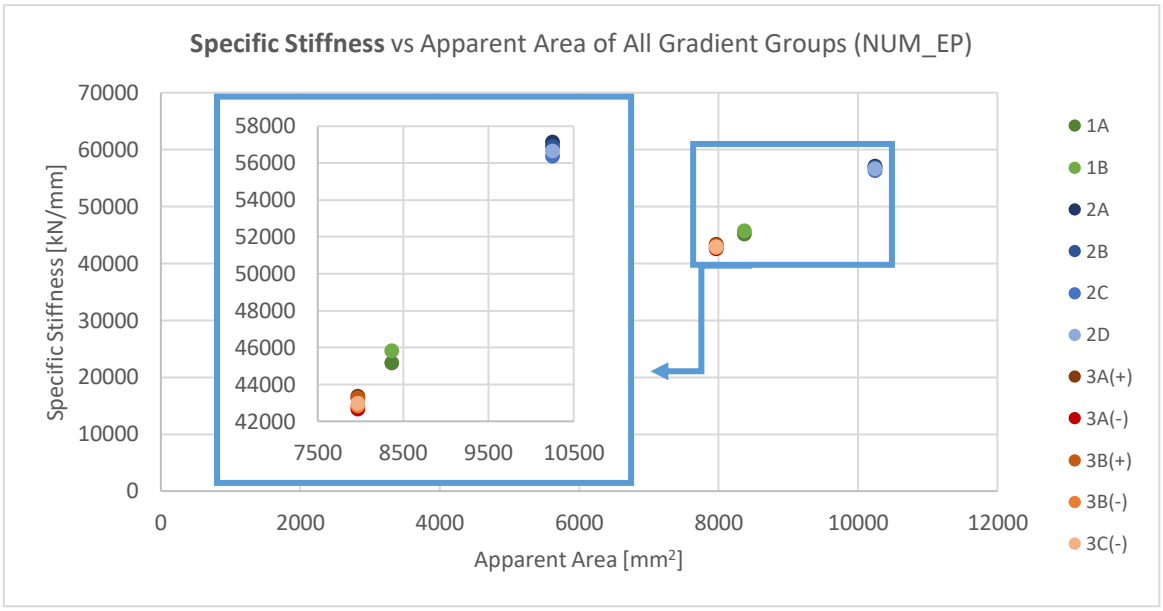

(a)

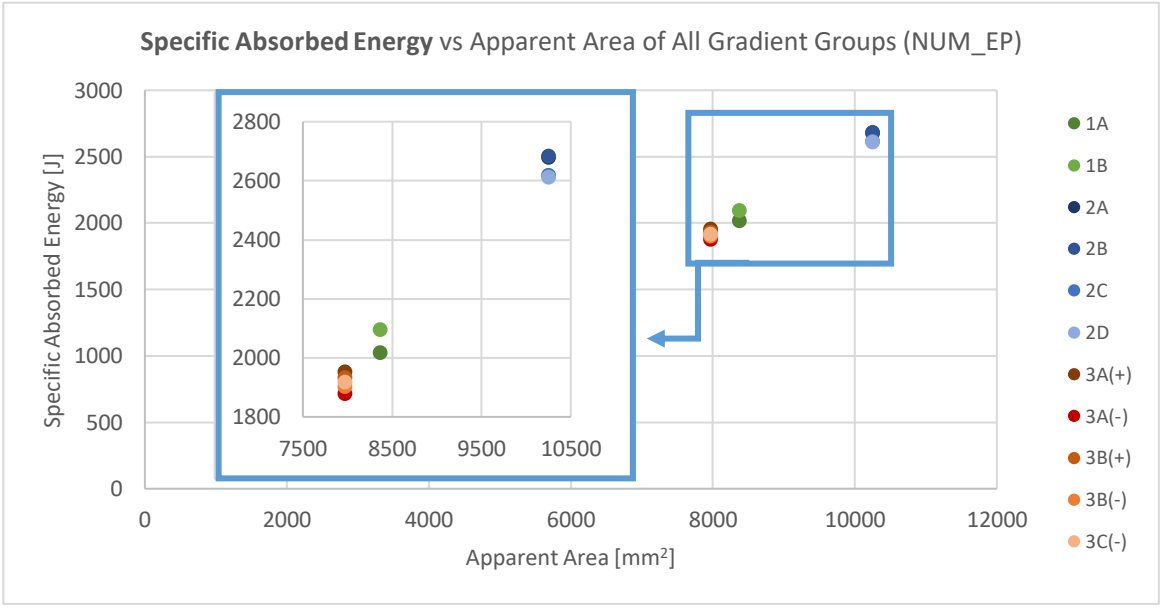

(b)

Figure 4.12: Specific stiffness (a) and specific absorbed area (b) vs apparent area for all gradient groups (NUM_EP)

When comparing the same results with varying apparent area (Figure 4.12), a pattern emerged. An increase in apparent area revealed a consequent increase in both specific stiffness and specific absorbed energy, almost in a linear pattern. The smaller variation in area between gradient groups *1* and *3*, designed with apparent areas of 8366.47mm^2 and 7965.90mm^2 respectively, represents a smaller variation in mechanical performance when compared to the clear superiority of samples from gradient group *2*, which were designed with a considerable higher apparent area (10246.92mm^2). A closer examination of the present plots exhibited an almost linear dependence between the stiffness and energy absorption of samples with their apparent area. In an effort of further investigating the influence of the internal geometry on the structures' out-of-plane mechanical performance (relative density), a normalization regarding apparent area was carried out for the values of specific stiffness and specific absorbed energy, with the results presented in Figure 4.13.

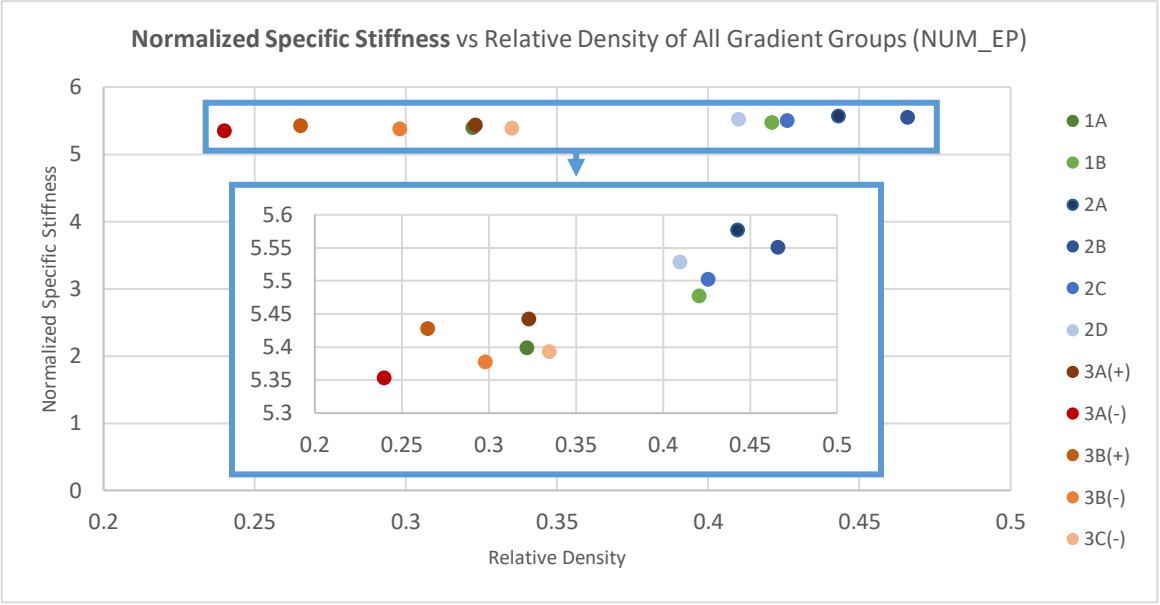

(a)

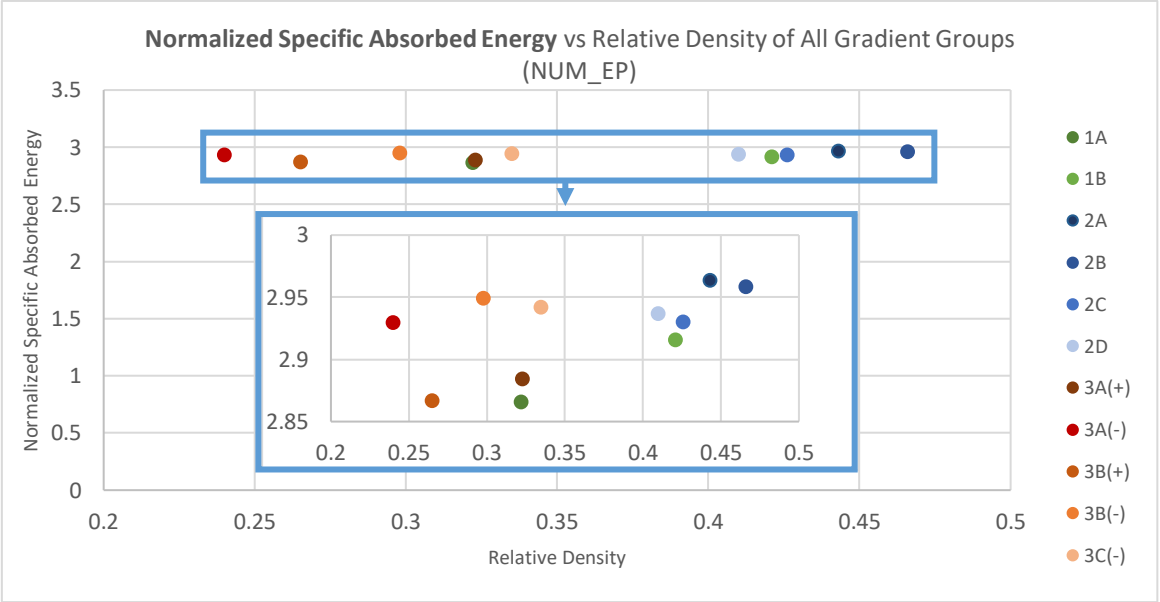

(b)

Figure 4.13: (a) Normalized specific stiffness vs relative density for all gradient groups (NUM_EP); (b) Normalized specific absorbed energy vs relative density for all gradient groups (NUM_EP)

A slight increase in specific stiffness with increasing relative density was seen regardless of the structure's apparent area. Regarding specified absorbed energy, three geometries were identified as showing superior values while presenting lower relative density (*3A(-)*, *3B(-)* and *3C(-)*). These structures were developed using gradient *3*, and all with a negative R parameter, which might indicate this geometrical combination is superior in terms of energy absorbing in the out-of-plane orientation.

4.3.2 In-Plane Compression

As mentioned previously, only three graded structures were both numerically and experimentally tested in the in-plane orientation. This being said, the analysis on the force-displacement curves will focus on these samples (Figure 4.16), with the remaining numerical curves being found in the Appendix D.

The influence of relative density and apparent area on all numerical simulations, as well as calculated values for specific stiffness, specific absorbed energy and maximum von Mises stress, were assessed and presented in Figures 4.14 and 4.15, and Table 4.6, respectively.

Table 4.6: Specific stiffness, specific absorbed energy and maximum von Mises stress for graded structures (in-plane numerical and experimental).

CODE	$\overline{\rho}$	$\overline{K}$ [kN/mm]		$\overline{E_a}$ (at 1.5 mm) [J]		$\sigma_{M,max}$ [MPa]
		NUM	EXP	NUM	EXP	NUM
1A	0.322	91.2	---	63.0	---	783.1*
1B	0.421	166.9	---	101.5	---	601.6
2A	0.443	195.1	---	114.1	---	479.0
2B	0.466	214.0	---	121.1	---	495.2
2C	0.426	195.1	---	123.7	---	490.4
2D	0.410	178.9	55.4±3.0	116.4	50.5±3.6	483.9
3A(+)	0.323	91.4	---	85.8	---	493.5
3A(-)	0.240	57.5	33.5±2.3	42.3	29.5±2.1	574.5
3B(+)	0.265	86.3	43.7±2.2	59.5	36.8±2.9	581.3
3B(-)	0.298	82.5	---	55.7	---	609.6
3C(+)	0.199	49.2	---	34.0	---	475.9
3C(-)	0.335	100.3	---	65.4	---	637.7

*Maximum von Mises stress considerably higher than the average due to stress concentrations.

When analysing the influence of relative density in the in-plane mechanical behaviour of the graded samples, a pattern was observed. An increase in relative density translated in an increase in specific stiffness and specific energy absorption, with some level of variation present inside each gradient group apart from samples. Once again, the results go accordingly to the model presented by Gibson and Ashby [7] regarding cellular materials, confirming the accuracy of the computational model.

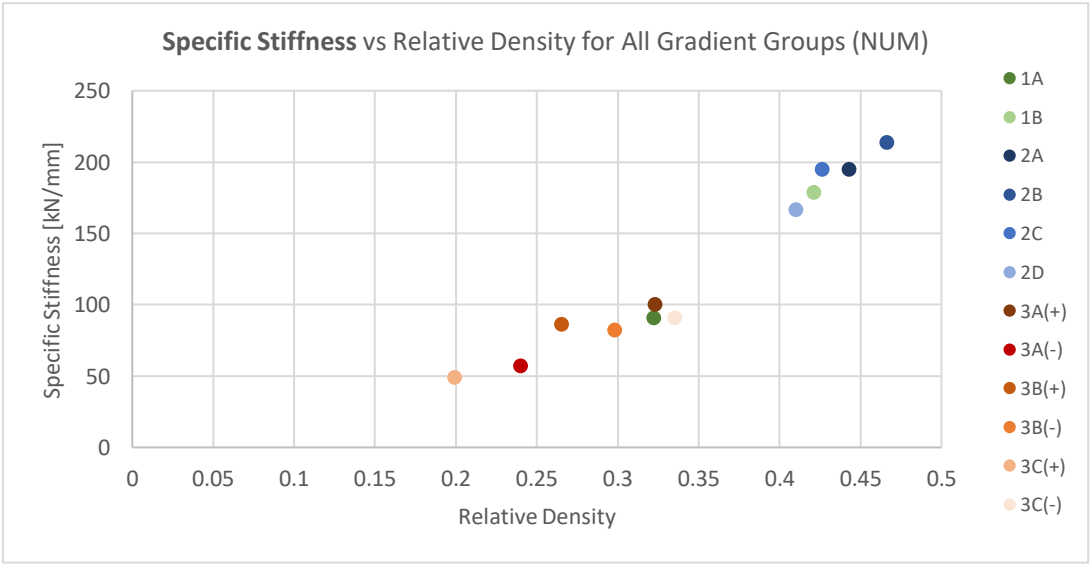

(a)

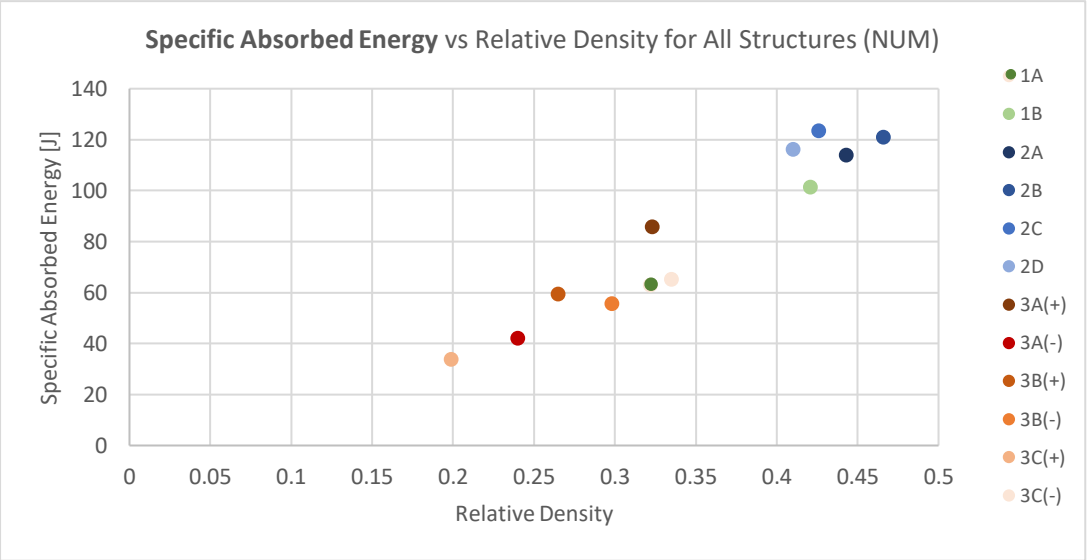

(b)

Figure 4.14: In-plane specific stiffness (a) and specific absorbed energy (b) vs relative density for all gradient groups (NUM)

An analysis on the specific stiffness and specific absorbed energy dependency on the apparent area of the samples proved that, even though there is still some degree of influence in the mechanical behaviour, it is not as relevant as in out-of-plane compression. By observing Figure 4.15, in which the normalized specific stiffness is compared with the relative density, the influence of the latter is confirmed, as the trend of increasing stiffness with increasing relative density is maintained. Apart from sample *1B*, the samples from gradient group *2* remained as the ones performing better, suggesting the conclusion that higher relative densities paired with an increase in apparent area provide the better combinations regarding the mechanical behaviour in in-plane compression cases.

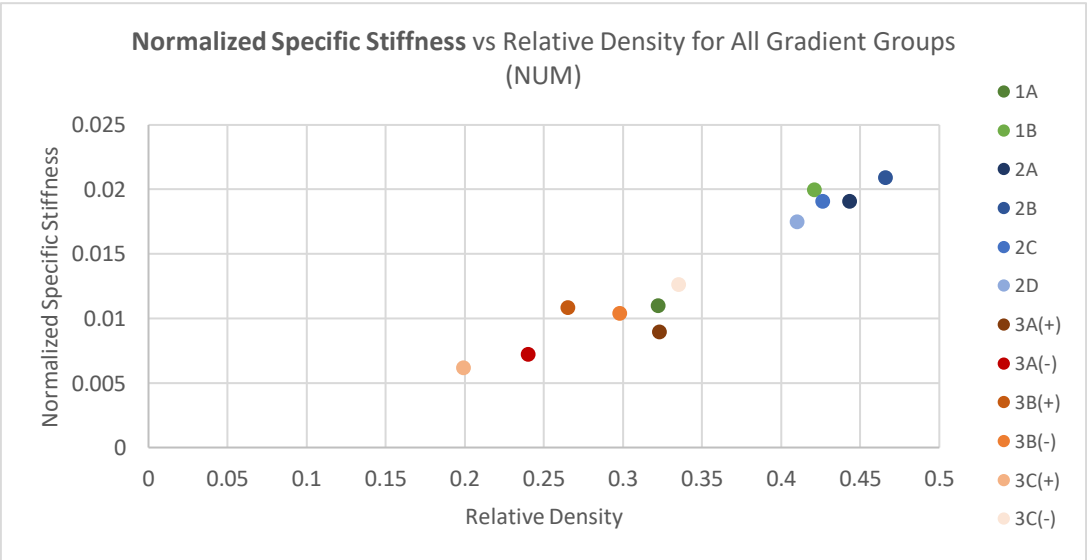

Figure 4.15: In-plane normalized specific stiffness vs relative density for all gradient groups (NUM)

The numerical and experimental force-displacement curves presented in Figure 4.16 showed similar results to those of the regular structures. It is important to mention that, due to the samples comprising gradient group *2* being larger in size, the displacements values were higher in testing of sample *2D*.

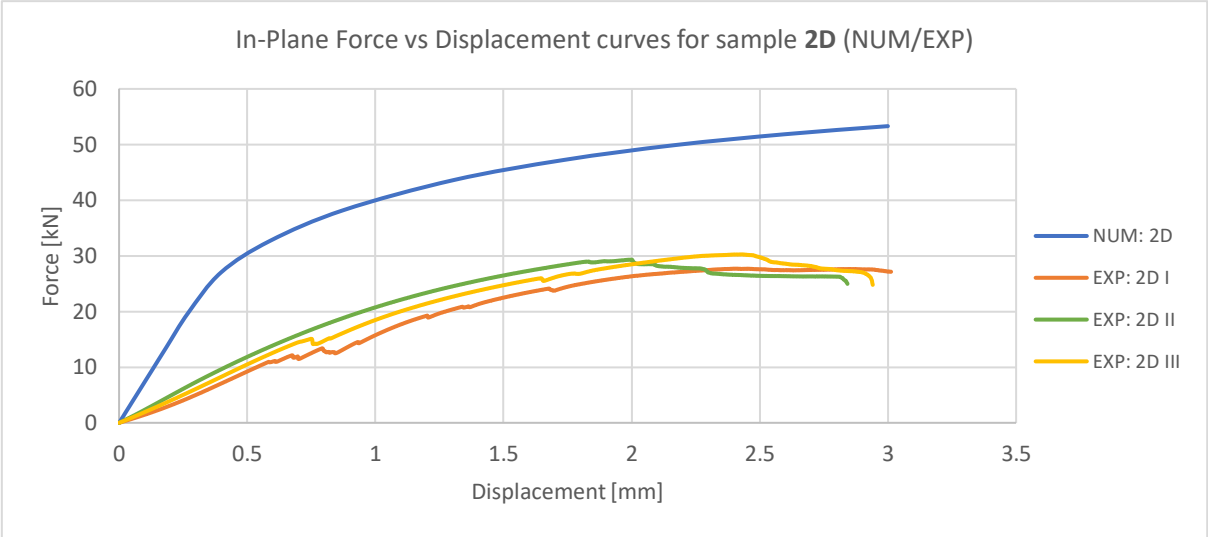

(a)

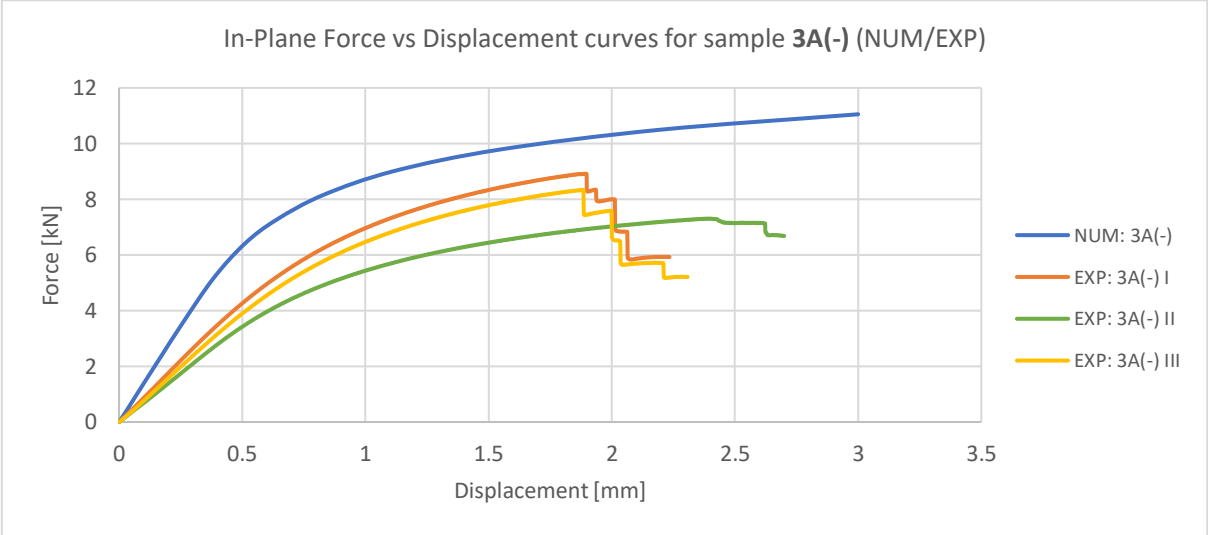

(b)

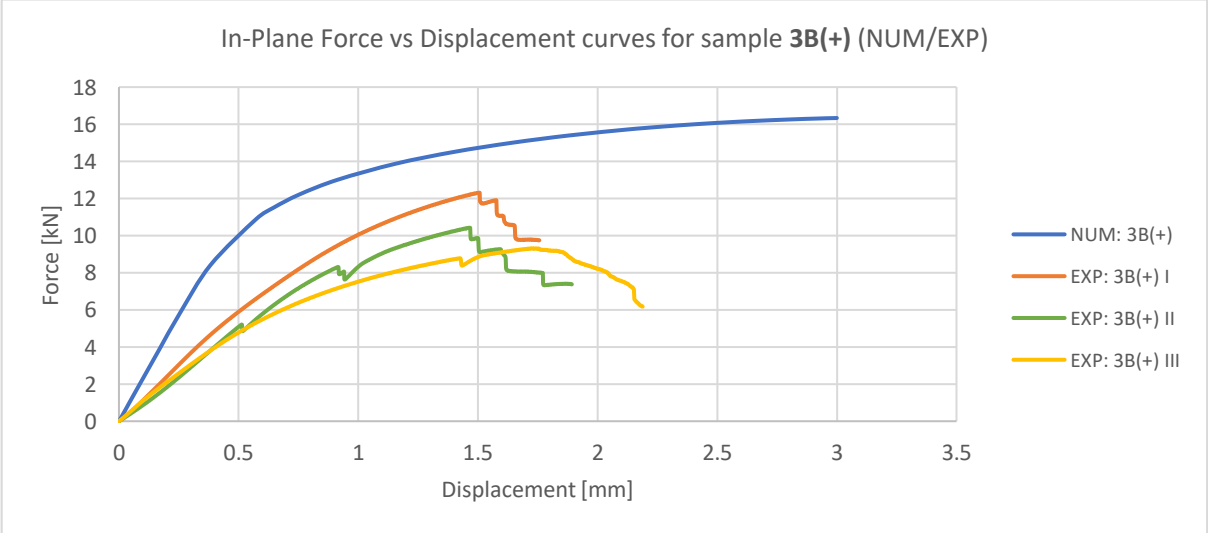

(c)

Figure 4.16: In-plane numerical and experimental force vs displacement curves for structures: (a) 2D; (b) 3A(-); (c) 3B(+)

A good match was observed between the experimental and numerical in-plane force-displacement curves, as well as relatively similar results for the different experimental testing of samples of the same design. The numerical curves were all similar in behaviour, with an initial elastic region followed by yield and a steady progression towards a plateau value of force. The experimental curves somewhat follow the same trend, with an initial elastic region followed by yielding. After yield, continuous small step-like reductions in force start appearing, revealing the failure of particular regions of the structure, due to plastic deformation, and subsequent fracture.

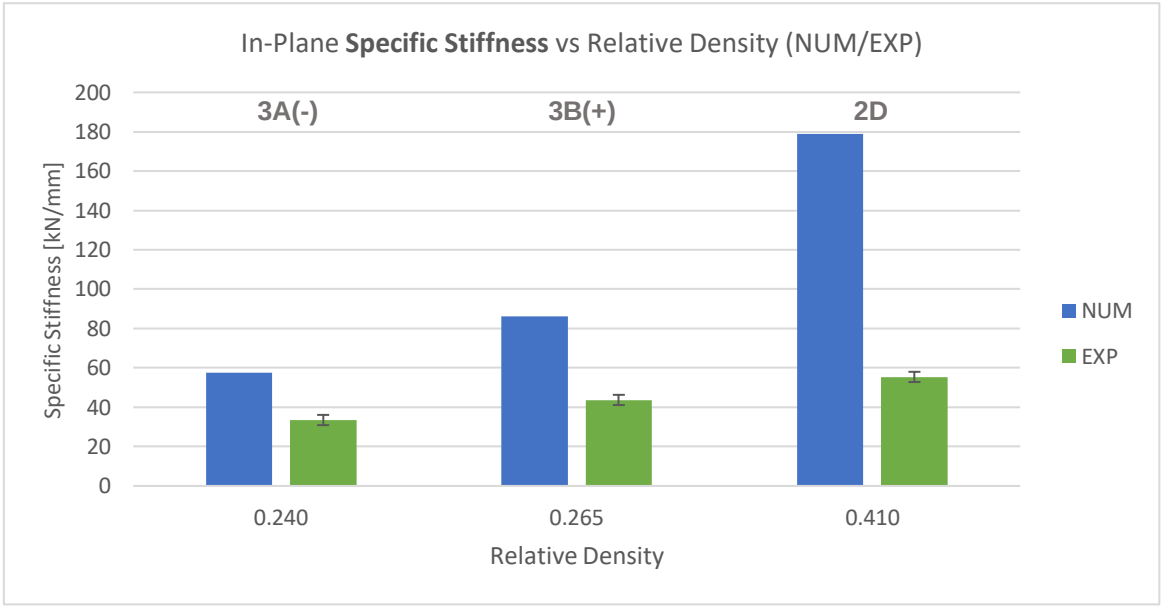

(a)

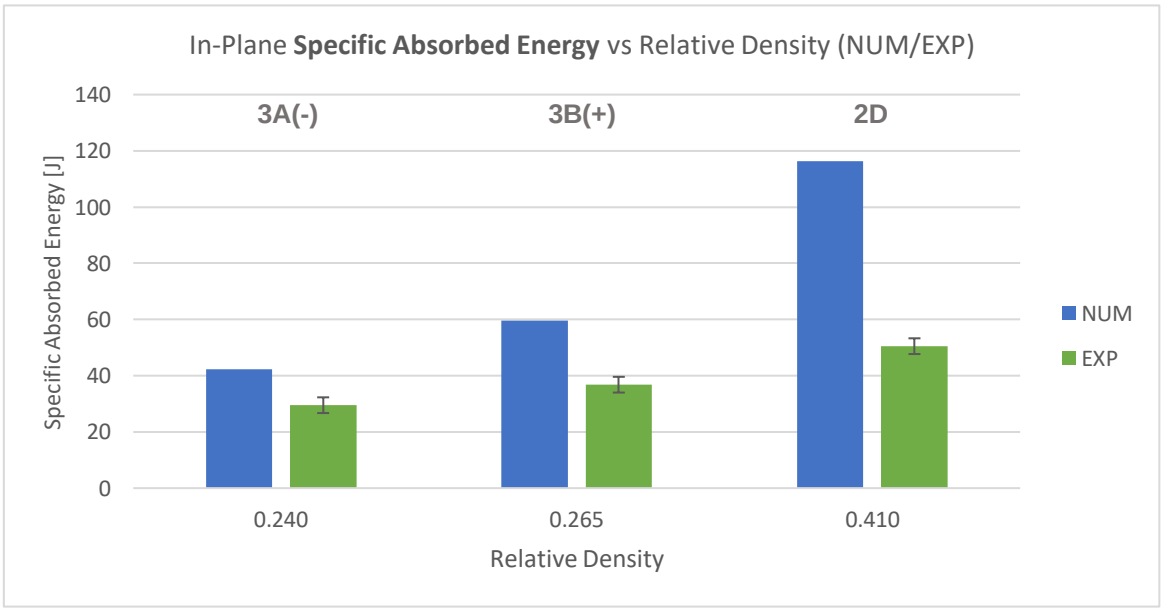

(b)

Figure 4.17: (a) Numerical and experimental in-plane specific stiffness (a) and specific absorbed energy (b) vs relative density for samples 2D, 3A(-) and 3B(+).

Observing the plots in Figure 4.17, the same conclusion which was taken from the numerical results can be taken for the experimental scenario, with a constant increase in both specific stiffness and specific absorbed energy with increasing relative density. Although the variation was not as acute as in the numerical values, a clear pattern could be established. This behaviour was once again expected, as higher values for relative density indicate an increasing relative thickness of the cell walls, offering a higher resistance to the applied load and consequent increase in stiffness. This means the structures are also able to absorb more energy when compared to ones with lower relative density for the imposed displacement, but may fail or fracture at an earlier stage. Although this occurrence was not observed, as the samples with higher stiffness value withstood larger displacements (samples *2D*), they are also significantly larger, which still affects the mechanical behaviour. Overall, the design which presented the better results in terms of in-plane compression of the graded structures was the samples in gradient group *2*, along with sample *1B*, which also featured a higher relative density.

In terms of the setting of plastic deformation in both numerically and experimentally tested graded structures, the results were satisfactory. The regions in which failure was predicted in the simulated graded structures coincided very closely with the critical deformation presented in the experimentally tested samples, as shown in Figure 4.18, 4.19 and 4.20.

(a)

(b)

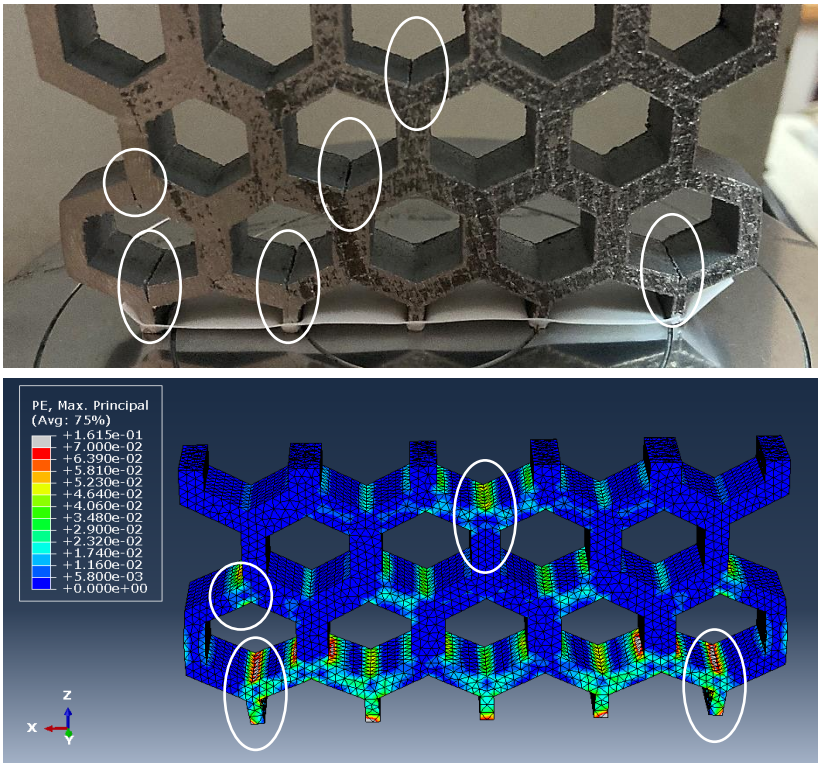

Figure 4.18: In-plane experimental (a) and simulated (b) (maximum plastic strain, PE) deformed samples, respectively, for sample 2D.

Starting with sample *2D*, a good match was observed when analysing Figure 4.18. Part (a) showed the plastic deformation withstood by the experimentally tested sample, before unloading, in which the failure was identified as occurring mostly in the points where three cell walls joined (triple junctions). This goes accordingly with the results obtained regarding in-plane testing of regular structures, confirming a pattern in the in-plane compression of cellular structures. A considerable level of deformation was also identified near the contact points with the compression plates.

Part (b) showed the same plastic deformation but on the numerical scenario. The range of values was defined as going from a null value of plastic strain until the maximum plastic strain the material was supposed to withstand (0.07), and then assuming that values equal or superior to the latter indicate fracture. As seen in the highlighted sections, plastic deformation was once again concentrated in triple junctions, more specifically the lowest and farthest triple junctions from the centre, which match the experimental results.

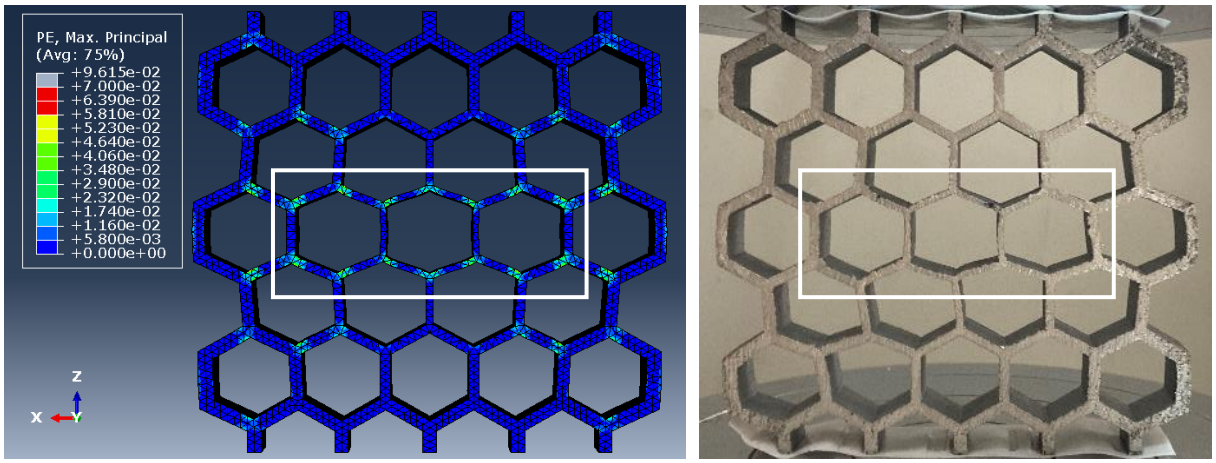

(a) (b)

Figure 4.19: In-plane experimental (a) and simulated (b) (maximum plastic strain, PE) deformed samples, respectively, for sample 3A(-).

Figure 4.19 represents the numerically predicted plastic deformation of sample *3A(-)* (a) and the experimental sample immediately before unloading (b). Once again, both deformed structures were similar, further confirming the matching of experimental results with the computational model. There was an evident buckling of cell walls in both scenarios, at a higher level in the outer, thicker cell walls. In the numerical results (a), the exterior of the structure was less deformed than the interior due to the imposed displacement, with concentration of plastic deformation in the central regions, in which density is lower. The same was perceived in the experimental results (b), and even though there were no signs of fracture in the triple junctions, the plastic deformation was still concentrated in these points of the central structure, as the deformation of the structure came from the shifting of these points in space.

Lastly, Figure 4.20 features the plastic deformation obtained for numerical (a) and experimental (b) in-plane compression testing for sample *3B(+)*. The plastic deformation predicted numerically for this particular design was predominantly concentrated in the middle lower contact region between the structure and the compression plates. A closer look showed a bending of the three middle contact points, which was simultaneously observed in the deformed experimental structure. Additional buckling of the lower exterior cell walls was observed in both numerical and experimental structures, with the thicker centre cells remaining relatively undeformed in both cases. Even though the numerical results predicted plastic strains superior to the maximum value submitted to the software, and therefore suggesting fracture, this was not observed in the experimentally tested structure.

It is important to refer that the images presented for samples *2D* and *3B(+)* were cut through the centre of the structure because the deformation was symmetrical, as the structures present axial symmetry in this orientation. This way, the deformation could be analysed in more detail.

(a)

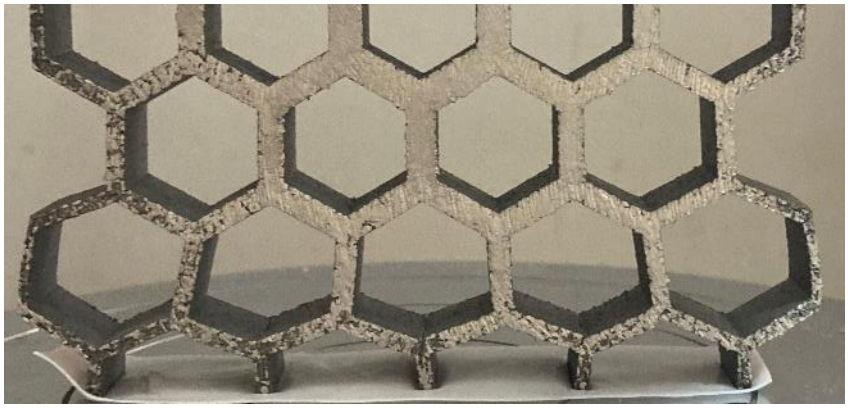

(b)

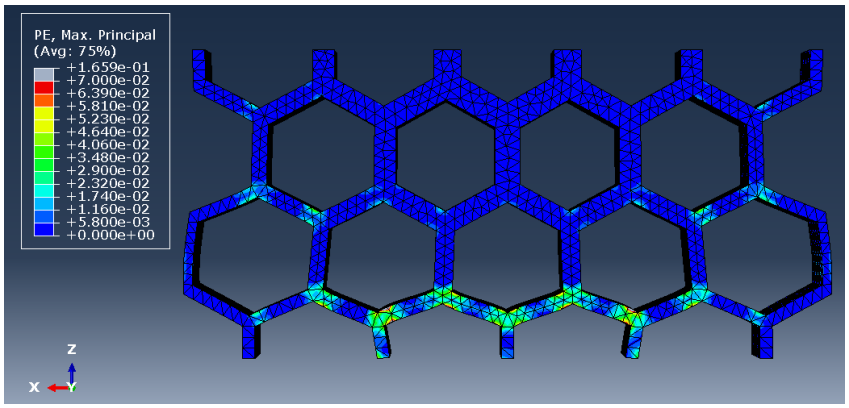

Figure 4.20: In-plane experimental (a) and simulated (b) (maximum plastic strain, PE) deformed samples, respectively, for sample 3B(+).

4.4 Regular and Graded Structures Comparison

One of the objectives of the present study was to compare the mechanical performance of the analysed regular and graded structures and therefore to ascertain if the use of density gradients in cellular structures was beneficial. For further comparison, a colour was assigned for the different geometries, as presented in Table 4.7. This said, a comparison was performed for regular and graded structures, with equal core height (H=12), for specific stiffness in relation to relative density and apparent area (Figure 4.21 (a) and (b), respectively). Figure 4.21 (a), showing the variation of specific stiffness of all designs with relative density shows a somewhat scattered distribution, with the graded structures presenting higher results. But when analysing the plot (b) for the relation with apparent area, this better performance is justified by the increase of the specimen size, creating an almost linear correlation. Even so, the graded structures demonstrated better results of specific stiffness comparing with regular structures, proving the applicability of density gradients. The graded structures also presented higher specific energy absorption.

Table 4.7: Regular and graded structures' designation and assigned colour code.

L6	L8	L10	1A	1B	2A	2B	2C	2D	3A(+)		3B(+)		3C(+)	
									+	-	+	-	+	-

(a)

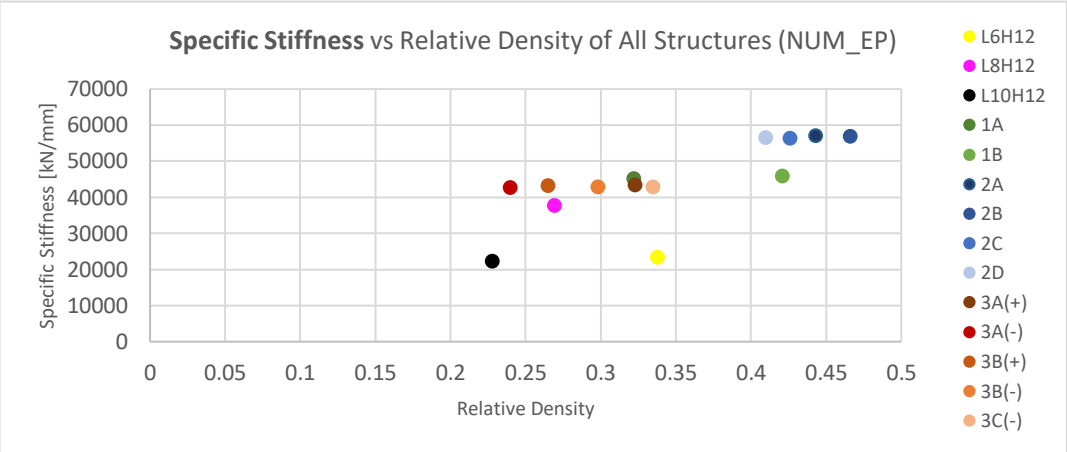

(b)

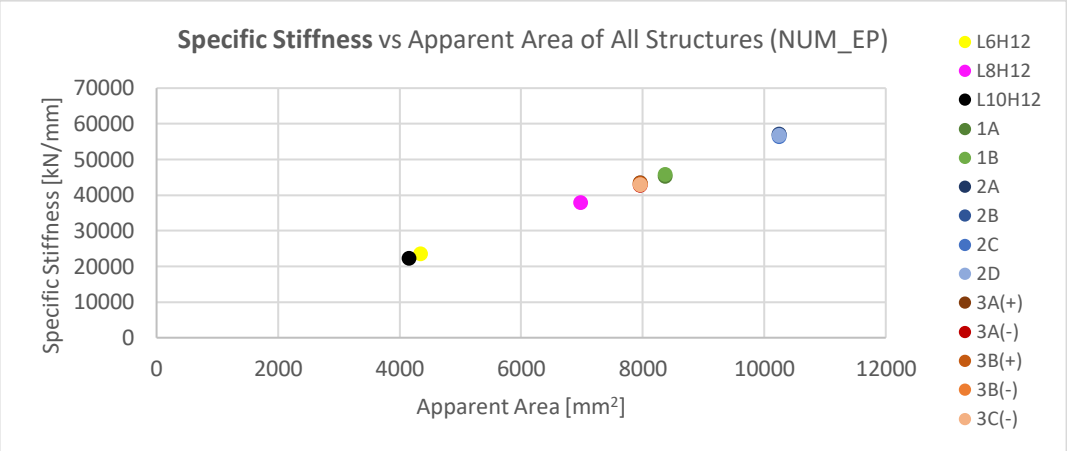

Figure 4.21: Out-of-plane specific stiffness vs relative density (a) and apparent area (b) for all structures (NUM_EP).

In terms of in-plane compression, it was concluded for both regular and graded structures that relative density was the main factor of dependency in terms of specific stiffness and specific energy absorption. This was due to the increase in relative thickness of cell walls, which translated into a stiffer response of the structure to the imposed displacement. There exists one key difference between the regular and graded structures compressed in the in-plane orientation, which is core height: regular structures have a core height of 10mm while graded structures have one of 12mm. This said, while there as little variation in terms of specific stiffness versus relative density (Figure 4.22 (a)), regular structures showed relatively lower results in terms of specific absorbed energy compared to their counterparts (Figure 4.22 (b)).

(a)

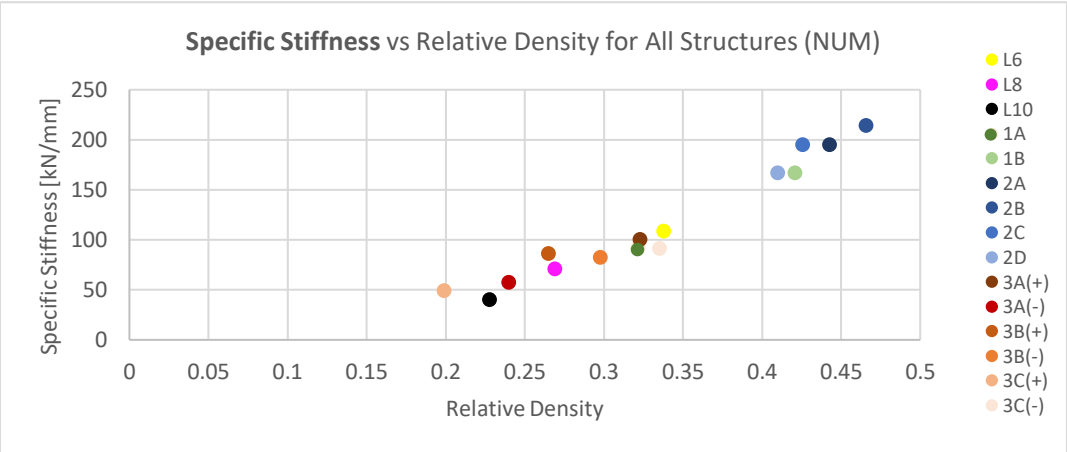

(b)

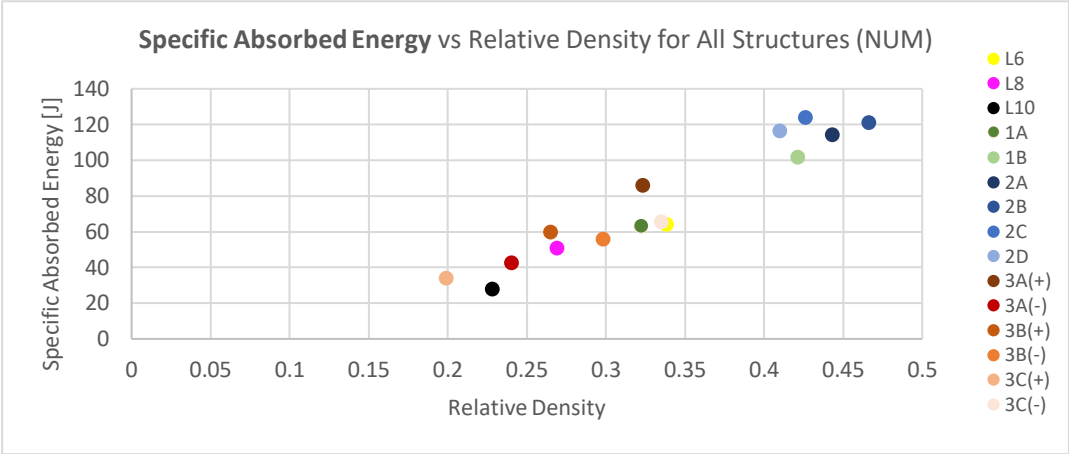

Figure 4.22: In-plane specific stiffness (a) and specific absorbed energy (b) vs relative density for all structures (NUM).

Although small variations were observed between regular and graded structures, it was difficult to traduce into clear conclusions, as there were key geometrical differences, mainly in terms of cell core height.

In terms of the experimental results, the same pattern was identified. When comparing samples of similar relative density, the graded structures were always superior in terms of specific stiffness and specific absorbed energy, as shown in Figure 4.23 (a) and (b), respectively.

(a)

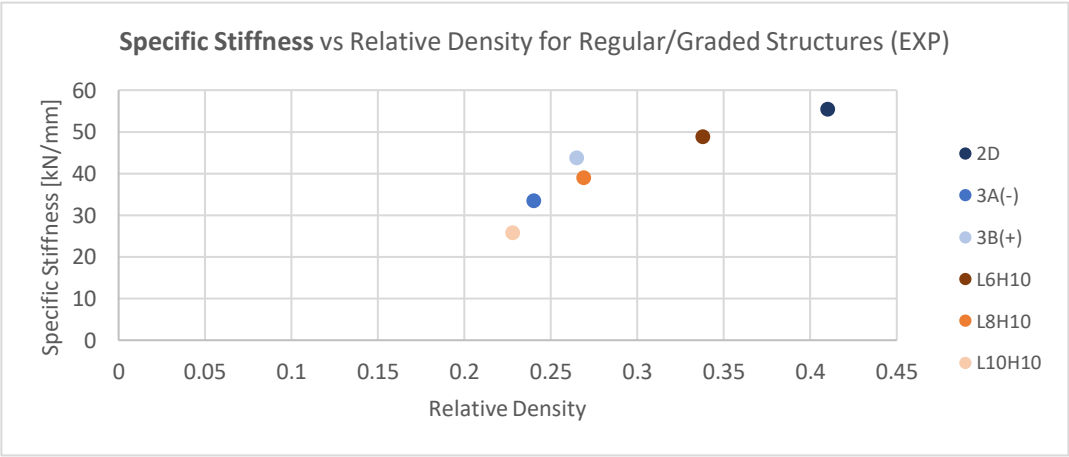

(b)

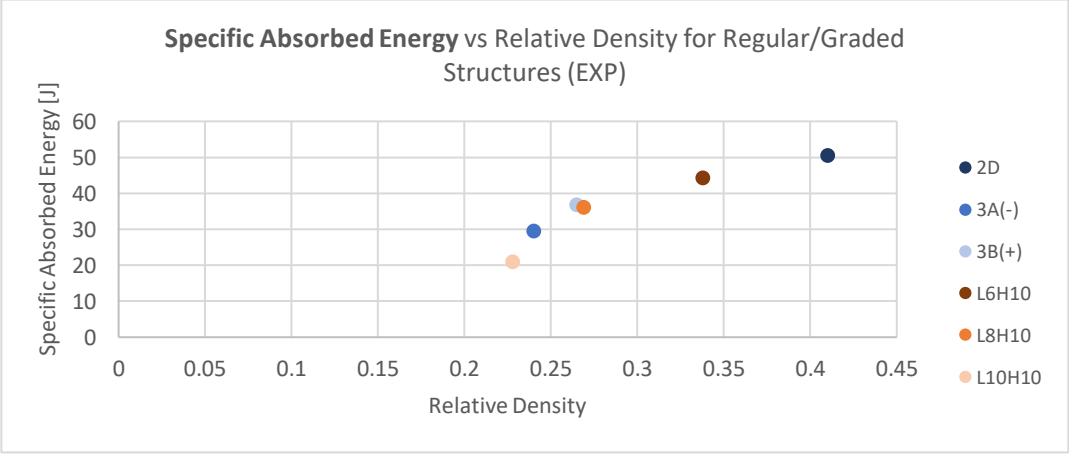

Figure 4.23: In-plane specific stiffness (a) and specific absorbed energy (b) vs relative density for regular and graded structures (EXP).

4.5 Failure Analysis

Following the experimental in-plane compression testing regarding the regular structures, the plastic deformation was observed via a low-resolution stereomicroscope, aiming for a better understanding of the failure mechanisms concerning this type of cellular materials produced via additive manufacturing.

As concluded in the previous chapters, the plastic deformation and consequent failure were allocated to the triple junctions, regions in which three cell walls are joined, which end up being stress concentrating regions. This can be seen in Figure 4.24, in which a section of a collapsed cell of the structure *L8H10* is presented. Observing with higher magnification, it was possible to identify the origin of the crack, as well as the directions in which it divided and propagated. Due to the change in geometry, as well as the irregular topography of the exterior of the cell walls, the stresses are concentrated in the junctions of cell walls, creating a crack. This crack might also initiate due to an irregularity in the material's microstructure, such as porosity or an inclusion, as observed in Figure 4.25.

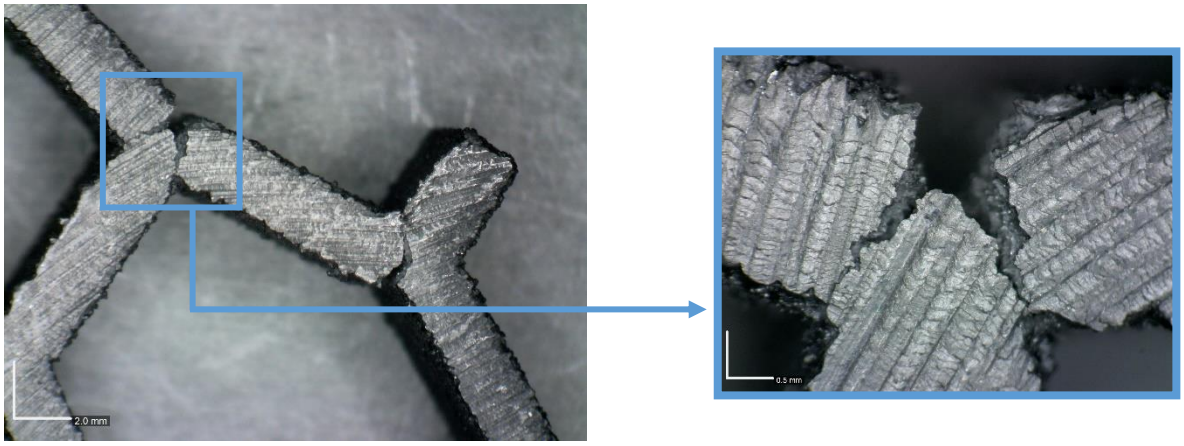

Figure 4.24: Fracture of a collapsed cell with magnification 0.5x and 2x (sample L6H10).

Figure 4.25 presents the surface of a section of a cell that fractured completely in sample *L6H10*, allowing for an appropriate observation of the macrostructure of the material, including the typical defects expected from structures produced via additive manufacturing processes.

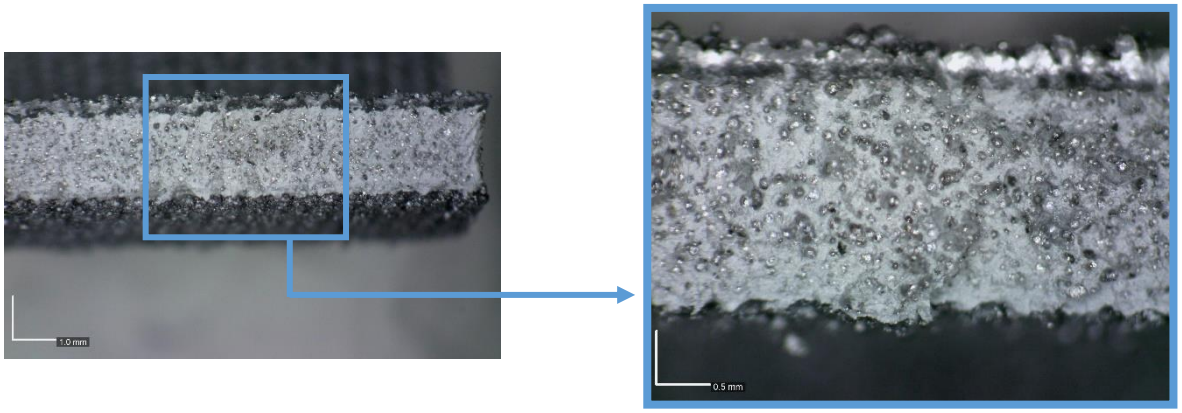

Figure 4.25: Fracture surface resulting from a fractured triple junction with magnification 0.5x and 2x (sample L8H10).

The higher magnification image allowed the identification of some level of porosity in the solid walls, as there are discontinuities and clear remarks of isolated pores in the fracture surface. This porosity may occur due to the presence of hydrogen during the fabrication process, which originates from residual humidity. Additionally, the fracture surface appeared to demonstrate the existence of some inclusions, which might be attributed to an isolated separation of a silicon-rich phase consequent of the selective laser melting process[93]. The irregularities in the edges of the structure were also noticeable, which might serve as stress concentrating defects, leading to permanent deformation and possible subsequent fracture [94].

The previously mentioned commentated factors are further confirmed in Figure 4.26, which displays the initiation and propagation of a crack in sample *L10H10*. The crack initiates in a junction of two cell walls located in a triple junction, and appears to emerge from an irregularity in the outer surface of the structure.

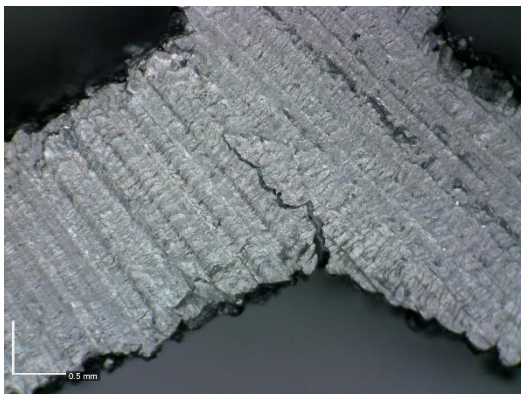

Figure 4.26: Crack initiation and propagation in a triple junction (sample L10H10).

Chapter 5: Conclusions

The present work aimed for both the out-of-plane and the in-plane mechanical characterization of regular and graded aluminium honeycomb structures produced by additive manufacturing processes. To achieve this goal, the samples were submitted to compression testing and a FEM computational model was developed in order to predict the mechanical behaviour of the samples, comparing both types of results for a better understanding of the structures. The structural failure was also studied in the experimental and numerical models, with a final analysis of the fractured samples being performed.

Regarding the out-of-plane results, it was concluded that the featured mechanical properties depended mainly on sample size, with increasing apparent area leading to an increase in specific stiffness and specific absorbed energy in both regular and graded structures in an almost linear pattern. Relative density was seen to be of secondary importance, with small variations between each gradient group. The best performing structures belonged to the gradient group *2*, in which the gradient is dependent on cell wall length, with this parameter varying between 7mm and 9mm in increasing or decreasing density gradients. In terms of regular structures, it was also concluded that lower cell core heights provide better stiffness and energy absorption potential. The comparison between the numerical and experimental models was not possible due to unsatisfactory experimental results, mostly likely originating from the experimental setup.

Regarding the in-plane results, it was concluded that the mechanical properties depended mainly on the relative density. An increase in this geometrical parameter is translated into an increase of the relative thickness of the cell walls, consequently resulting in higher values of relative stiffness. The same was observed in terms of specific absorbed energy. Normalizing the two analysed variables by the apparent area showed little to no change in the pattern of mechanical behaviour, but allowed for the highlighting of graded structures designed with a negative R parameter in terms of specific absorbed energy. A comparison between the in-plane regular and graded mechanical properties was performed, although with different core cell heights (10mm and 12mm, respectively). Graded structures showed better results overall (numerical), with an overall better specific stiffness concerning structures with similar relative density. Regarding specific absorbed energy, the graded structures were clearly superior, with the example of sample *3A(+)*, with a lower relative density of *0.323*, showing an increase in 34.3% compared to sample *L6H10*, with a higher relative density of 0.338. The same applied to the in-plane experimental results, with the graded structures presenting both superior specific stiffness and energy absorption. Ultimately, it was concluded that the structures presenting a density gradient performed better mechanically when compared to regular structures, presenting higher values of specific stiffness and absorbed energy in the out-of-plane and in-plane orientation.

The matching of the FEA results to the experimental results, as well as the force-displacement curves recorded in each scenario, suggests a good correlation between the designed computational model and the observed mechanical behaviour of honeycomb structures, and further confirmed the relevance of the use of Finite Element Method in the structural analysis of cellular structures. This good correlation was further confirmed by comparing the maximum plastic strain observed in the simulated deformed structures, which was located in regions in which failure/fracture was observed in the experimental samples (triple junctions). This fact was better observed in the graded samples due to the added functionality of the structures, with the cells collapsing in certain regions specific to each singular design.

Finally, a failure analysis was also performed on the deformed regular structures via a low-resolution stereomicroscope. Crack initiation and propagation was observed and photographed in various triple junctions, as mentioned above. Additionally, a fracture surface was studied, revealing defects typical of parts produced by additive manufacturing, like some level of solid porosity and the presence of inclusions. These defects, as well as the irregular topography of the cell wall's outer surface, serve as stress concentrators for crack initiation.

In summary:

- Regarding the influence of geometrical parameters, it was concluded that the main influence in the out-of-plane orientation was the apparent area, and in the in-plane orientation was the relative density.
- Comparing between regular and graded structures, the graded structures shower superior results for specific stiffness and specific absorbed energy in both orientations when compared to their regular counterparts. The better mechanically performing geometries were the ones designed with gradient *2*, while samples designed with gradient *3* and a negative R parameter showed promising results in terms of energy absorption in the out-of-plane orientation.
- The relevance of the use of the Finite Element Method in the structural analysis of cellular structures was confirmed, as a satisfactory correlation was identified between the computational model and the real behaviour of the samples, with a relatively accurate matching between numerical and experimental results, both in the deformation analysis and the force-displacement curves (mainly in the in-plane orientation).
- Regarding the final failure analysis, the triple junctions were identified as the main points of plastic deformation initiation and propagation. A level of porosity was observed in the macrostructure of the material, possibly due to the existence of residual humidity during the fabrication process.

5.1 Future Work

In order to further explore this topic and, the potential of honeycomb structures, some suggestions of future work are as follows:

- Further testing and reviewing the out-of-plane experimental compression testing apparatus. Equipping extensometers or a loading cell of higher force might be some possible solutions.

- Perform a deeper mechanical characterization of the used aluminium alloy, in bulk, to obtain important information regarding the plastic behaviour of the material.
- Increasing the displacement rate used in the compression testing, with the intent of studying the energy absorption properties of the designed structures as a function of strain rate, or even feature a study in impact or dynamic crushing testing, applications in which the in-plane mechanical properties of honeycomb structures may prove advantageous.
- Experimentally testing the remaining functionally graded structures to obtain a larger information base, as well as testing the regular samples with cell core height equal to the graded structures (12mm) in the in-plane orientation to assess if this geometric variable impacts the results.
- Expanding the study to other types of geometry for the unit cells, like plateau or lotus.

Bibliography

[1] H. Seitz, W. Rieder, S. Irsen, B. Leukers, and C. Tille, “Three-dimensional printing of porous ceramic scaffolds for bone tissue engineering,” *J Biomed Mater Res B Appl Biomater*, vol. 74B, no. 2, pp. 782–788, Aug. 2005, doi: 10.1002/jbm.b.30291.

[2] L. Yin, J. Doyhamboure--Fouquet, X. Tian, and D. Li, “Design and characterization of radar absorbing structure based on gradient-refractive-index metamaterials,” *Compos B Eng*, vol. 132, pp. 178–187, Jan. 2018, doi: 10.1016/j.compositesb.2017.09.003.

[3] D. Qi, Q. Lu, C. He, Y. Li, W. Wu, and D. Xiao, “Impact energy absorption of functionally graded chiral honeycomb structures,” *Extreme Mech Lett*, vol. 32, p. 100568, Oct. 2019, doi: 10.1016/j.eml.2019.100568.

[4] A. Ajdari, S. Babaee, and A. Vaziri, “Mechanical properties and energy absorption of heterogeneous and functionally graded cellular structures,” *Procedia Eng*, vol. 10, pp. 219–223, 2011, doi: 10.1016/j.proeng.2011.04.039.

[5] T. Fan, “Dynamic crushing behavior of functionally graded honeycomb structures with random defects,” *International Journal of Materials Research*, vol. 107, no. 9, pp. 783–789, Sep. 2016, doi: 10.3139/146.111403.

[6] T. Rua, “Out-of-Plane Compression Behaviour of Honeycomb Structures with Mass Gradient Produced by Additive Manufacturing Technologies,” Masters, Instituto Superior Técnico, Universidade de Lisboa, Lisbon, 2021.

[7] L. J. Gibson and M. F. Ashby, *Cellular Solids: Structure and Properties*. Cambridge University Press, 1997. doi: 10.1017/CBO9781139878326.

[8] D. Bhate, C. A. Penick, L. A. Ferry, and C. Lee, “Classification and selection of cellular materials in mechanical design: Engineering and biomimetic approaches,” *Designs*, vol. 3, no. 1. MDPI AG, pp. 1–31, Mar. 01, 2019. doi: 10.3390/designs3010019.

[9] D. Bhate, “Four questions in cellular material design,” *Materials*, vol. 12, no. 7, 2019, doi: 10.3390/ma12071060.

[10] H. N. G. Wadley, “Multifunctional periodic cellular metals,” *Philosophical Transactions of the Royal Society A: Mathematical, Physical and Engineering Sciences*, vol. 364, no. 1838, pp. 31–68, Jan. 2006, doi: 10.1098/rsta.2005.1697.

[11] F. Zhu, G. Lu, D. Ruan, and Z. Wang, “Plastic Deformation, Failure and Energy Absorption of Sandwich Structures with Metallic Cellular Cores,” 2010.

[12] I. E. Ramirez-Chavez, D. Anderson, R. Sharma, C. Lee, and D. Bhate, “A Classification of Aperiodic Architected Cellular Materials,” *Designs (Basel)*, vol. 6, no. 4, p. 63, Jul. 2022, doi: 10.3390/designs6040063.

[13] M. Helou and S. Kara, “Design, analysis and manufacturing of lattice structures: An overview,” *Int J Comput Integr Manuf*, vol. 31, no. 3, pp. 243–261, 2018, doi: 10.1080/0951192X.2017.1407456.

[14] K. M. Park, K. S. Min, and Y. S. Roh, “Design Optimization of Lattice Structures under Compression: Study of Unit Cell Types and Cell Arrangements,” *Materials*, vol. 15, no. 1, Jan. 2022, doi: 10.3390/ma15010097.

[15] StarGlade, “Asa Libélula,” *Pixabay*. https://pixabay.com/pt/vectors/lib%C3%A9lula-asa-besouro-inseto-inseto-1531038/ (accessed Sep. 01, 2022).

[16] Energy Efficient Solutions, “Open-Cell vs. Closed-Cell Spray Foam,” *Johns Manville*, Oct. 28, 2020. https://www.jm.com/en/blog/2020/october/open-cell-vs--closed-cell-spray-foam/ (accessed Sep. 01, 2022).

[17] T. A. Schaedler and W. B. Carter, “Architected Cellular Materials,” *Annual Review of Materials Research*, vol. 46. Annual Reviews Inc., pp. 187–210, Jul. 01, 2016. doi: 10.1146/annurev-matsci-070115-031624.

[18] G. Stephani, B. Kieback, O. Andersen, and P. Quadbeck, “Cellular Metals for Functional Applications - an Overview,” 2010. [Online]. Available: https://www.researchgate.net/publication/267842500

[19] J. Banhart, “Manufacture, characterisation and application of cellular metals and metal foams,” 2000. [Online]. Available: www.elsevier.com/locate/pmatsci

[20] T. Bitzer, *Honeycomb Technology*. Springer Netherlands, 1997. doi: 10.1007/978-94-011-5856-5.

[21] T. C. Hales, “The honeycomb conjecture,” *Discrete Comput Geom*, vol. 25, no. 1, pp. 1–22, 2001, doi: 10.1007/s004540010071.

[22] F. Morgan, “The Hexagonal Honeycomb Conjecture,” *Trans Am Math Soc*, vol. 351, no. 5, pp. 1753–1763, Jan. 1999, doi: 10.1090/s0002-9947-99-02356-9.

[23] T. Bitzer, *Honeycomb Technology*. Springer Netherlands, 1997. doi: 10.1007/978-94-011-5856-5.

[24] X. Wei, D. Li, and J. Xiong, “Fabrication and mechanical behaviors of an all-composite sandwich structure with a hexagon honeycomb core based on the tailor-folding approach,” *Compos Sci Technol*, vol. 184, Nov. 2019, doi: 10.1016/j.compscitech.2019.107878.

[25] Q. Zhang *et al.*, “Bioinspired engineering of honeycomb structure - Using nature to inspire human innovation,” *Progress in Materials Science*, vol. 74. Elsevier Ltd, pp. 332–400, Jul. 16, 2015. doi: 10.1016/j.pmatsci.2015.05.001.

[26] H. Sunami, E. Ito, M. Tanaka, S. Yamamoto, and M. Shimomura, “Effect of honeycomb film on protein adsorption, cell adhesion and proliferation,” *Colloids Surf A Physicochem Eng Asp*, vol. 284–285, pp. 548–551, Aug. 2006, doi: 10.1016/j.colsurfa.2005.11.041.

[27] M. Afzal, N. Gupta, A. Mallik, K. S. Vishnulal, and P. Sharma, “Experimental analysis of a metal hydride hydrogen storage system with hexagonal honeycomb-based heat transfer enhancements-part B,” *Int J Hydrogen Energy*, vol. 46, no. 24, pp. 13131–13141, Apr. 2021, doi: 10.1016/j.ijhydene.2020.11.275.

[28] J. Qiao and C. Chen, “In-plane crushing of a hierarchical honeycomb,” *Int J Solids Struct*, vol. 85–86, pp. 57–66, May 2016, doi: 10.1016/j.ijsolstr.2016.02.003.

[29] L. J. Gibson, M. F. Ashby, G. S. Schajer, C. I. Robertson, G. S. Schajert, and C. I. R. Ertsoni, “The Mechanics of Two-Dimensional Cellular Materials,” 1982.

[30] J. Zhang and M. F. Ashby, “The out-of-plane properties of honeycombs,” 1992.

[31] S. N. Abhinav and M. Varma Budharaju, “A Review Paper on Origin of Honeycomb Structure and its Sailing Properties,” Aug. 2020. [Online]. Available: www.ijert.org

[32] J. Pflug, I. Verpoest, and D. Vandepitte, “FOLDED HONEYCOMBS Fast and continuous production of the core and a reliable core-skin bond,” Leuven, Jul. 1999.

[33] J. Pflug, B. Vangrimde, I. Verpoest, P. Bratfisch, and D. Vandepitte, “CONTINUOUSLY PRODUCED HONEYCOMB CORES,” Jan. 2003. [Online]. Available: https://www.researchgate.net/publication/291141551

[34] L. Wang and K. Saito, “Honeycomb structures manufactured by a new method and its failure analysis,” in *Journal of Physics: Conference Series*, Jan. 2021, vol. 1733, no. 1. doi: 10.1088/1742-6596/1733/1/012003.

[35] K. Naplocha, A. Dmitruk, P. Mayer, and J. W. Kaczmar, “Design of honeycomb structures produced by investment casting,” *Archives of Foundry Engineering*, vol. 19, no. 4, pp. 76–80, 2019, doi: 10.24425/afe.2019.129633.

[36] L. Tripathi and B. Kumar Behera, “3D woven honeycomb composites: Manufacturing method, structure properties, and applications;,” *Journal of Textile Engineering & Fashion Technology*, vol. 8, no. 3, Jun. 2022, doi: 10.15406/jteft.2022.08.00304.

[37] “ASTM standard F2792 − 12a,” 2012, doi: 10.1520/F2792-12A.

[38] I. Gibson, D. Rosen, B. Stucker, and M. Khorasani, *Additive Manufacturing Technologies*, 3rd ed. Springer, 2021. doi: https://doi.org/10.1007/978-3-030-56127-7.

[39] I. Campbell, D. Bourell, and I. Gibson, “Additive manufacturing: rapid prototyping comes of age,” *Rapid Prototyp J*, vol. 18, no. 4, pp. 255–258, Jun. 2012, doi: 10.1108/13552541211231563.

[40] P. K. Gokuldoss, S. Kolla, and J. Eckert, “Additive manufacturing processes: Selective laser melting, electron beam melting and binder jetting-selection guidelines,” *Materials*, vol. 10, no. 6, 2017, doi: 10.3390/ma10060672.

[41] C. Y. Yap *et al.*, “Review of selective laser melting: Materials and applications,” *Applied Physics Reviews*, vol. 2, no. 4. American Institute of Physics Inc., Dec. 01, 2015. doi: 10.1063/1.4935926.

[42] C. Li, C. H. Fu, Y. B. Guo, and F. Z. Fang, “Fast Prediction and Validation of Part Distortion in Selective Laser Melting,” in *Procedia Manufacturing*, 2015, vol. 1, pp. 355–365. doi: 10.1016/j.promfg.2015.09.042.

[43] M. Drexler, D. Drummer, and K. Wudy, “Interaction between Time Dependent Exposure Strategies and Part Positioning within Selective Laser Melting Process of Plastics,” *International Journal of Recent Contributions from Engineering, Science & IT (iJES)*, vol. 3, no. 1, p. 13, Mar. 2015, doi: 10.3991/ijes.v3i1.4286.

[44] J. Wilkes, Y. C. Hagedorn, W. Meiners, and K. Wissenbach, “Additive manufacturing of ZrO2-Al2O3 ceramic components by selective laser melting,” *Rapid Prototyp J*, vol. 19, no. 1, pp. 51–57, 2013, doi: 10.1108/13552541311292736.

[45] I. Kauppila, “Selective Laser Melting (SLM 3D Printing) – The Ultimate Guide,” *All3DP.Pro*, Jan. 24, 2022. https://all3dp.com/1/selective-laser-melting-guide/ (accessed Jul. 18, 2022).

[46] M. Mohammadi, M. Rajabi, and M. Ghadiri, “Functionally graded materials (FGMs): A review of classifications, fabrication methods and their applications,” *Processing and Application of Ceramics*, vol. 15, no. 4, pp. 319–343, 2021, doi: 10.2298/PAC2104319M.

[47] E. C. N. Silva, M. C. Walters, and G. H. Paulino, “Modeling bamboo as a functionally graded material: lessons for the analysis of affordable materials,” *Journal of Materials Science 2006 41:21*, vol. 41, no. 21, pp. 6991–7004, Nov. 2006, doi: 10.1007/S10853-006-0232-3.

[48] L. H. He and M. v. Swain, “Enamel-A functionally graded natural coating,” *J Dent*, vol. 37, no. 8, pp. 596–603, Aug. 2009, doi: 10.1016/J.JDENT.2009.03.019.

[49] M. Sato, A. Inoue, and H. Shima, “Bamboo-inspired optimal design for functionally graded hollow cylinders,” *PLoS One*, vol. 12, no. 5, p. e0175029, May 2017, doi: 10.1371/JOURNAL.PONE.0175029.

[50] M. Shen and M. B. Bever, “Gradients in polymeric materials,” *Journal of Materials Science 1972 7:7*, vol. 7, no. 7, pp. 741–746, Jul. 1972, doi: 10.1007/BF00549902.

[51] G. E. Knoppers, J. W. Gunnink, J. van den Hout, and W. P. van Vliet, “The Reality of Functionally Graded Material Products,” *International Solid Freeform Fabrication Symposium*, 2004, doi: http://dx.doi.org/10.26153/tsw/5706.

[52] M. Niino and S. Maeda, “Recent Development Status of Functionally Gradient Materials,” *ISIJ International*, vol. 30, no. 9, pp. 699–703, Sep. 1990, doi: 10.2355/ISIJINTERNATIONAL.30.699.

[53] N. K. Sharma and M. Bhandari, “Applications of Functionally Graded Materials (FGMs),” *International Journal of Engineering Research & Technology*, vol. 2, no. 3, Jul. 2018, doi: 10.17577/IJERTCONV2IS03054.

[54] J. Y. Hascoet, P. Muller, and P. Mognol, “Manufacturing of Complex Parts with Continuous Functionally Graded Materials (FGM),” Aug. 2011, doi: 10.26153/TSW/15317.

[55] J. W. Shin and Y. S. Lee, “Dynamic propagation of a weak-discontinuous interface crack between two dissimilar functionally graded layers under anti-plane shear,” *Journal of Mechanical Science and Technology*, vol. 25, no. 10, pp. 2551–2557, Oct. 2011, doi: 10.1007/S12206-011-0723-2.

[56] R. M. Mahamood and E. T. Akinlabi, “Types of Functionally Graded Materials and Their Areas of Application,” in *Functionally Graded Materials*, Springer Science and Business Media Deutschland GmbH, 2017, pp. 9–21. doi: 10.1007/978-3-319-53756-6_2/COVER.

[57] A. Yevtushenko, K. Topczewska, and P. Zamojski, “The Effect of Functionally Graded Materials on Temperature during Frictional Heating: Under Uniform Sliding,” *Materials*, vol. 14, no. 15, p. 4285, Jul. 2021, doi: 10.3390/ma14154285.

[58] Y. Feng, J. Qiao, and L. Li, “Acoustic behavior of composites with gradient impedance,” *Mater Des*, vol. 193, Aug. 2020, doi: 10.1016/J.MATDES.2020.108870.

[59] I. Matuła, G. Dercz, and J. Barczyk, “Titanium/Zirconium functionally graded materials with porosity gradients for potential biomedical applications,” *https://doi.org/10.1080/02670836.2019.1593603*, vol. 36, no. 9, pp. 972–977, Jun. 2019, doi: 10.1080/02670836.2019.1593603.

[60] Y. H. Hsu, I. G. Turner, and A. W. Miles, “Fabrication of porous bioceramics with porosity gradients similar to the bimodal structure of cortical and cancellous bone,” *Journal of Materials Science: Materials in Medicine 2007 18:12*, vol. 18, no. 12, pp. 2251–2256, Jun. 2007, doi: 10.1007/S10856-007-3126-2.

[61] J. Guo, Q. Y. He, Q. S. Mei, X. Huang, G. L. Wu, and O. v. Mishin, “Gradient microstructure, recrystallization and mechanical properties of copper processed by high pressure surface rolling,” *J Mater Sci Technol*, vol. 126, pp. 182–190, Nov. 2022, doi: 10.1016/J.JMST.2022.03.011.

[62] B. Garrido Silva *et al.*, “Functionally graded cellular cores of sandwich panels fabricated by additive manufacturing,” *Proceedings of the Institution of Mechanical Engineers, Part L: Journal of Materials: Design and Applications*, vol. 236, no. 9, pp. 1814–1828, Sep. 2022, doi: 10.1177/14644207221084611.

[63] G. H. Loh, E. Pei, D. Harrison, and M. D. Monzón, “An overview of functionally graded additive manufacturing,” *Addit Manuf*, vol. 23, pp. 34–44, Oct. 2018, doi: 10.1016/j.addma.2018.06.023.

[64] A. Ajdari, P. Canavan, H. Nayeb-Hashemi, and G. Warner, “Mechanical properties of functionally graded 2-D cellular structures: A finite element simulation,” *Materials Science and Engineering: A*, vol. 499, no. 1–2, pp. 434–439, Jan. 2009, doi: 10.1016/j.msea.2008.08.040.

[65] H. Zhou, X. Wang, and Z. Zhao, “High velocity impact mitigation with gradient cellular solids,” *Compos B Eng*, vol. 85, pp. 93–101, Feb. 2016, doi: 10.1016/j.compositesb.2015.09.042.

[66] B. G. M. Silva, “Cellular structures for use in composite panels with a mass distribution gradient produced by additive manufacturing,” Masters, Instituto Superior Técnico, Lisbon, 2021.

[67] O. Rahman, K. Z. Uddin, J. Muthulingam, G. Youssef, C. Shen, and B. Koohbor, “Density-Graded Cellular Solids: Mechanics, Fabrication, and Applications,” *Adv Eng Mater*, vol. 24, no. 1, Jan. 2022, doi: 10.1002/adem.202100646.

[68] R. v. Duraibabu, R. Prithvirajan, M. Sugavaneswaran, and G. Arumaikkannu, “Compression behavior of Functionally Graded Cellular Materials fabricated with FDM,” *Mater Today Proc*, vol. 24, pp. 1035–1041, Jan. 2020, doi: 10.1016/J.MATPR.2020.04.417.

[69] S. Y. Choy, C.-N. Sun, K. F. Leong, and J. Wei, “Compressive properties of functionally graded lattice structures manufactured by selective laser melting,” *Mater Des*, vol. 131, pp. 112–120, Oct. 2017, doi: 10.1016/j.matdes.2017.06.006.

[70] A. Panesar, M. Abdi, D. Hickman, and I. Ashcroft, “Strategies for functionally graded lattice structures derived using topology optimisation for Additive Manufacturing,” *Addit Manuf*, vol. 19, pp. 81–94, Jan. 2018, doi: 10.1016/J.ADDMA.2017.11.008.

[71] C. H. P. Nguyen and Y. Choi, “Multiscale design of functionally graded cellular structures for additive manufacturing using level-set descriptions,” *Structural and Multidisciplinary Optimization*, vol. 64, no. 4, pp. 1983–1995, Oct. 2021, doi: 10.1007/S00158-021-02959-3/FIGURES/18.

[72] Y. Sun, L. Guo, T. Wang, L. Yao, and X. Sun, “Bending strength and failure of single-layer and double-layer sandwich structure with graded truss core,” *Compos Struct*, vol. 226, p. 111204, Oct. 2019, doi: 10.1016/j.compstruct.2019.111204.

[73] X. J. Xu and J. M. Meng, “A model for functionally graded materials,” *Compos B Eng*, vol. 145, pp. 70–80, Jul. 2018, doi: 10.1016/J.COMPOSITESB.2018.03.014.

[74] S. R. G. Bates, I. R. Farrow, and R. S. Trask, “Compressive behaviour of 3D printed thermoplastic polyurethane honeycombs with graded densities,” *Mater Des*, vol. 162, pp. 130–142, Jan. 2019, doi: 10.1016/j.matdes.2018.11.019.

[75] A. Ajdari, H. Nayeb-Hashemi, and A. Vaziri, “Dynamic crushing and energy absorption of regular, irregular and functionally graded cellular structures,” *Int J Solids Struct*, vol. 48, no. 3–4, pp. 506–516, Feb. 2011, doi: 10.1016/J.IJSOLSTR.2010.10.018.

[76] D. Chen, J. Yang, and S. Kitipornchai, “Nonlinear vibration and postbuckling of functionally graded graphene reinforced porous nanocomposite beams,” *Compos Sci Technol*, vol. 142, pp. 235–245, Apr. 2017, doi: 10.1016/J.COMPSCITECH.2017.02.008.

[77] J. Liu, B. Hou, F. Lu, and H. Zhao, “A theoretical study of shock front propagation in the density graded cellular rods,” *Int J Impact Eng*, vol. 80, pp. 133–142, 2015, doi: 10.1016/J.IJIMPENG.2015.02.001.

[78] Y. Wu, L. Sun, P. Yang, J. Fang, and W. Li, “Energy absorption of additively manufactured functionally bi-graded thickness honeycombs subjected to axial loads,” *Thin-Walled Structures*, vol. 164, p. 107810, Jul. 2021, doi: 10.1016/j.tws.2021.107810.

[79] H. Liu, E. T. Zhang, and B. F. Ng, “In-plane dynamic crushing of a novel honeycomb with functionally graded fractal self-similarity,” *Compos Struct*, vol. 270, p. 114106, Aug. 2021, doi: 10.1016/j.compstruct.2021.114106.

[80] H. Liu, E. T. Zhang, G. Wang, and B. F. Ng, “In-plane crushing behavior and energy absorption of a novel graded honeycomb from hierarchical architecture,” *Int J Mech Sci*, vol. 221, p. 107202, May 2022, doi: 10.1016/j.ijmecsci.2022.107202.

[81] J. Votano, M. Parham, and L. Hall, *Hanbook of aluminum Volume 2 alloy production and material manufacturing*. 2004. Accessed: Sep. 22, 2022. [Online]. Available: https://www.routledge.com/Handbook-of-Aluminum-Volume-2-Alloy-Production-and-Materials-Manufacturing/Totten-MacKenzie/p/book/9780824708962

[82] Z. Wang *et al.*, “Selective Laser Melting of Aluminum and Its Alloys,” *Materials*, vol. 13, no. 20, pp. 1–67, Oct. 2020, doi: 10.3390/MA13204564.

[83] Deutsches Institut für Normung, “DIN EN 1706: Aluminium and aluminium alloys - Castings - Chemical composition and mechanical properties,” 1998.

[84] SLM Solutions Group AG, “Al-Alloy AlSi7Mg0,6 Material Data Sheet.”

[85] A. Mauduit, H. Gransac, P. Auguste, S. Pillot, and A. Diószegi, “Study of AlSi7Mg0.6 Alloy by Selective Laser Melting: Mechanical Properties, Microstructure, Heat Treatment,” *Journal of Casting & Materials Engineering*, vol. 3, no. 1, p. 1, 2019, doi: 10.7494/JCME.2019.3.1.1.

[86] A. Miranda, “Desenvolvimento, caracterização e modelação de novos conceitos no projeto de honeycombs usados em painéis compósitos,” Masters, Instituto Superior Técnico, Universidade de Lisboa, Lisbon, 2019.

[87] Aniwaa, “SLM Solutions SLM 125.” https://www.aniwaa.com/product/3d-printers/slm-solutions-slm-125-hl/ (accessed Aug. 12, 2022).

[88] “Classic Metal Plasticity.” http://194.167.201.93/English/SIMACAEMATRefMap/simamat-c-metalplastic.htm (accessed Aug. 25, 2022).

[89] H. Araújo, M. Leite, A. Ribeiro, A. M. Deus, L. Reis, and M. F. Vaz, “Investigating the contribution of geometry on the failure of cellular core structures obtained by additive manufacturing,” *Frattura ed Integrità Strutturale*, vol. 13, no. 49, pp. 478–486, Jun. 2019, doi: 10.3221/IGF-ESIS.49.45.

[90] “Standard test method for flatwise compressive properties of sandwich cores,” *ASTM C365-94*.

[91] “Pre-Configured Method Templates for the BlueHill Universal.” https://www.azom.com/materials-video-details.aspx?VidID=3193 (accessed Aug. 28, 2022).

[92] J. Zhang and M. F. Ashby, “THE OUT-OF-PLANE PROPERTIES OF HONEYCOMBS,” 1992.

[93] K. Kempen, L. Thijs, J. van Humbeeck, and J.-P. Kruth, “Mechanical Properties of AlSi10Mg Produced by Selective Laser Melting,” *Phys Procedia*, vol. 39, pp. 439–446, 2012, doi: 10.1016/j.phpro.2012.10.059.

[94] Z. W. Xu, Q. Wang, X. S. Wang, C. H. Tan, M. H. Guo, and P. B. Gao, “High cycle fatigue performance of AlSi10mg alloy produced by selective laser melting,” *Mechanics of Materials*, vol. 148, p. 103499, Sep. 2020, doi: 10.1016/j.mechmat.2020.103499.

[95] SLM Solutions Group AG, “AlSi7Mg0,6 Powder Material Analysis Certificate,” 2016.

Appendix A: Material's Supplementary Information

The present appendix contains supplementary information regarding the aluminium alloy utilized in the production of the physical samples, with Table A.1 containing the chemical composition of the utilized AlSi7Mg0.6 alloy powder.

Table A.1: Chemical composition of the AlSi7Mg0.6 alloy [95]

Chemical Element	Minimum [$wt\%$]	Actual [$wt\%$]	Maximum [$wt\%$]
Aluminium (Al)	**Balance**	**Balance**	**Balance**
Copper (Cu)	---	<0.01	0.05
Iron (Fe)	---	0.13	0.19
Magnesium (Mg)	0.45	0.47	0.70
Manganese (Mn)	---	<0.01	0.10
Silicon (Si)	6.50	6.65	7.50
Titanium (Ti)	---	0.01	0.25
Zinc (Zn)	---	<0.01	0.07
Others each	---	0.03	0.03
Others total	---	0.10	0.10

Appendix B: Supplementary Information on the samples

The present appendix contains supplementary information regarding the designed samples, more specifically the 3D-CAD models of the regular structures, and photographs and the masses of the physical samples produced via SLM.

B.1 Regular 3D-CAD models

Figure B.1 (a-c) presents de 3D-CAD models of the *L6*, *L8* and *L10* geometries, respectively. As mentioned in sub-chapter 3.2.1, samples were designed with three different core cell heights of 6mm, 10mm and 12mm for each 2D geometry.

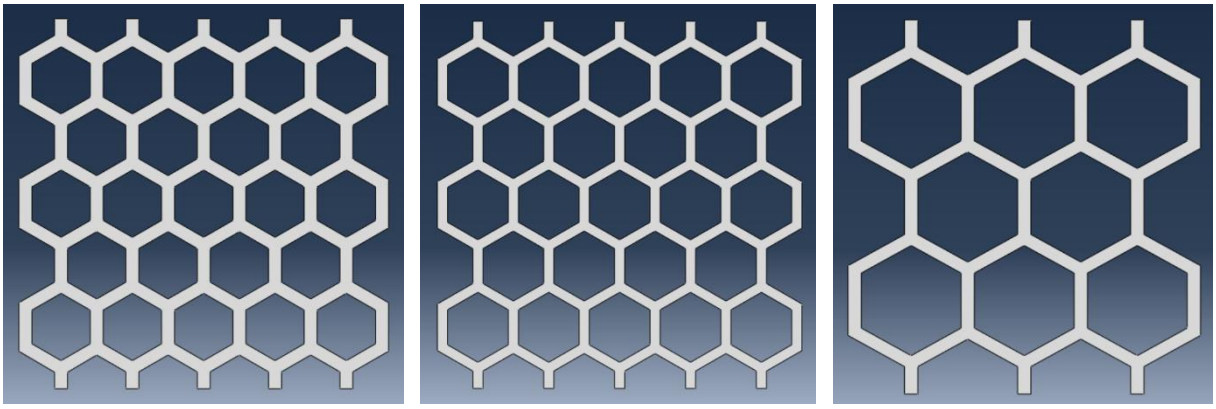

(a) (b) (c)

Figure B.1: 3D-CAD model for structures: (a) L6; (b) L8; (c) L10.

B.2 Physical Samples

B.2.1 Regular Structures

Figure B.2 (a-c) shows the produced samples for the structures of designation *L6*, *L8* and *L10*, respectively. The core height of 10mm was arbitrarily chosen.

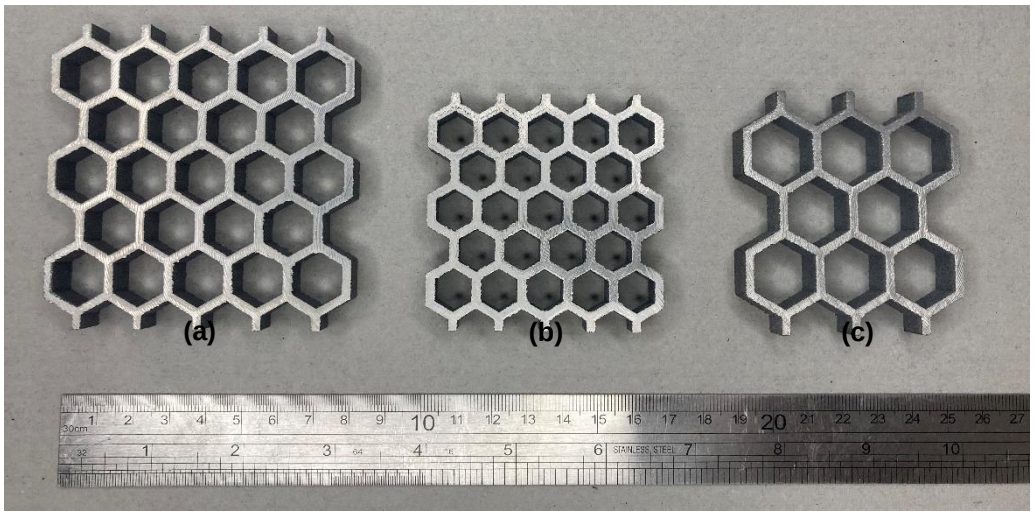

Figure B.2: Physical samples for structures: (a) L8; (b) L6; (c) L10

Table B.1 indicates the respective masses of the post-processed physical regular structures of all geometries.

Table B.1: Mass of post-processed physical regular structures.

Code	Mass [g]
L6H6	26.85
L6H10 (I)	42.96
L6H10 (II)	42.44
L6H10 (III)	42.76
L6H12	49.81
L8H6	34.89
L8H10 (I)	53.23
L8H10 (II)	52.89
L8H10 (III)	54.99
L8H12	64.04
L10H6	17.56
L10H10 (I)	27.42
L10H10 (II)	28.52
L10H10 (III)	27.44
L10H12	32.78

B.2.2 Graded Structures

Figure B.3, B.4 and B.5 show the produced samples for the structures of designation *2D*, *3A(-)* and 3B(+), respectively.

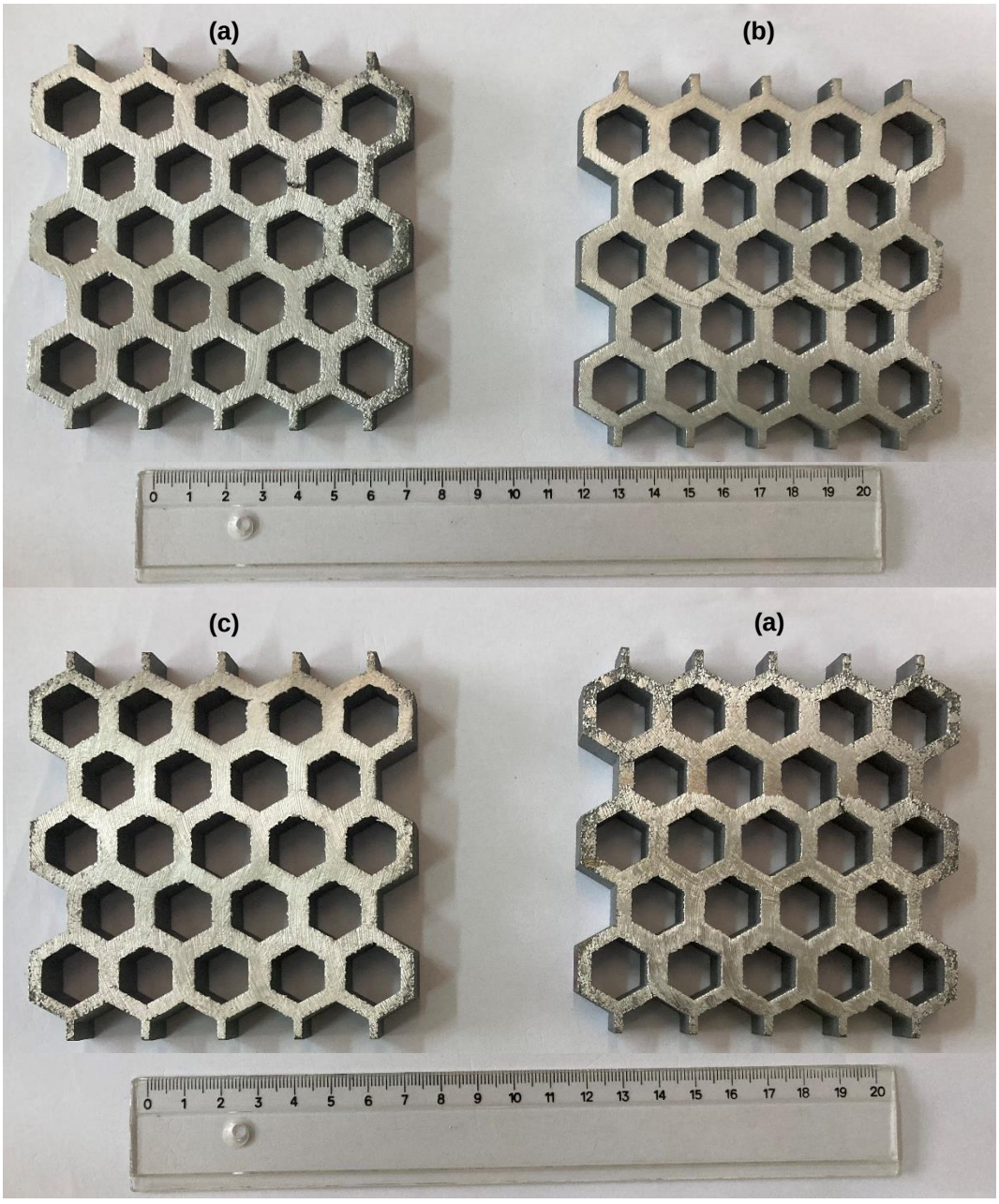

Figure B.3: Physical samples for structures 2D: (a) I; (b) II; (c) III; (d) IV.

It is important to mention that the recorded results were only applied to three samples to maintain the statistics in average results throughout all tested samples, with the chosen ones being samples 2D (I), (II) and (II).

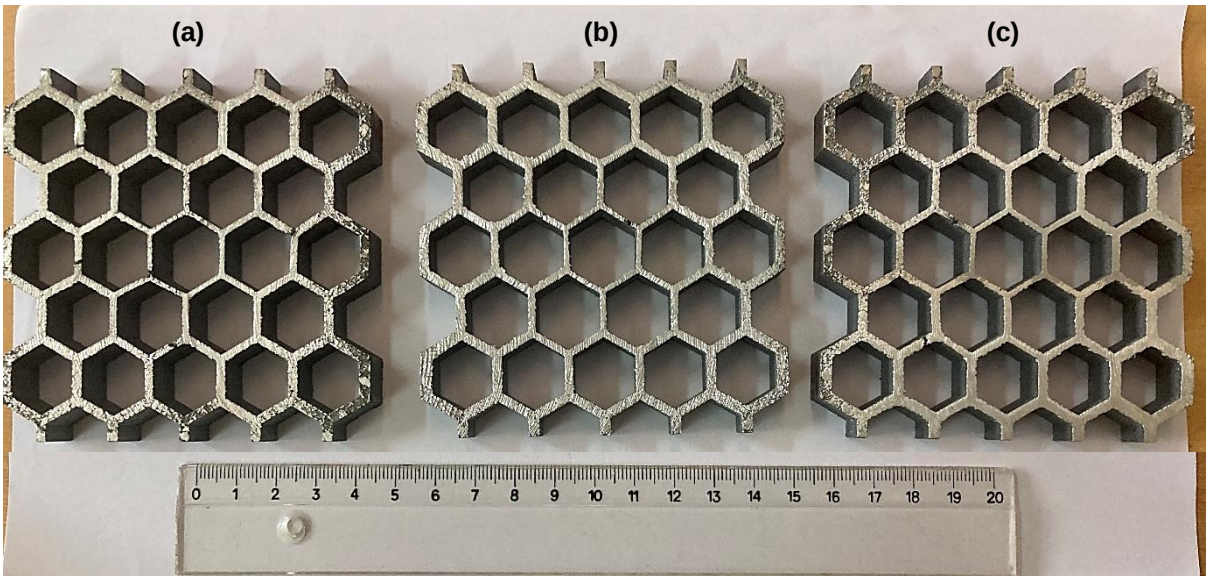

Figure B.4: Physical samples for structures 3A(-): (a) I; (b) II; (c) III.

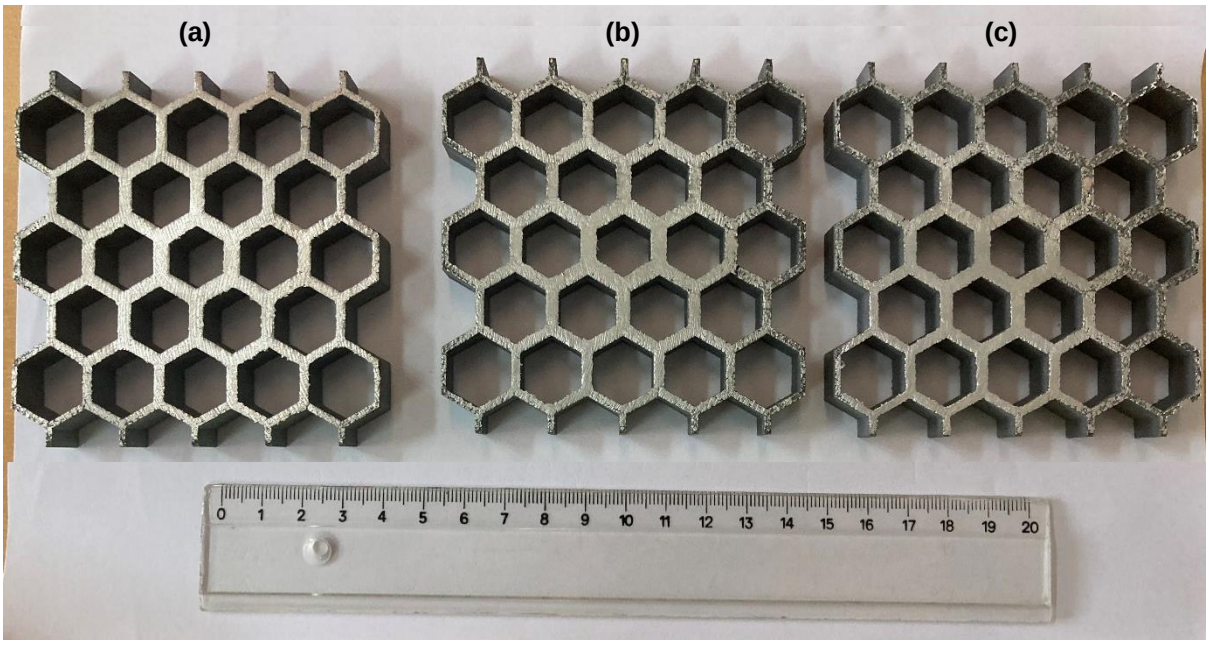

Figure B.5: Physical samples for structures 3B(+): (a) I; (b) II; (c) III.

Table B.2: Mass of post-processed physical graded structures

Code	Mass [g]
2D (I)	129.46
2D (II)	128.06
2D (III)	129.29
2D (IV)	131.91
3A(-) (I)	58.49
3A(-) (II)	58.24
3A(-) (III)	58.88
3B(+) (I)	64.23
3B(+) (II)	65.19
3B(+) (III)	65.22

Appendix C: Convergence Analysis

As mentioned in sub-chapter 3.3.9, a mesh convergence analysis was performed in specific regular and graded structures (*L6H10* and *2D*, respectively). The present appendix consists in the mesh convergence analysis performed for the model 2D, starting with the position of the three nodes in which the average von Mises was recorded (Figure C.1).

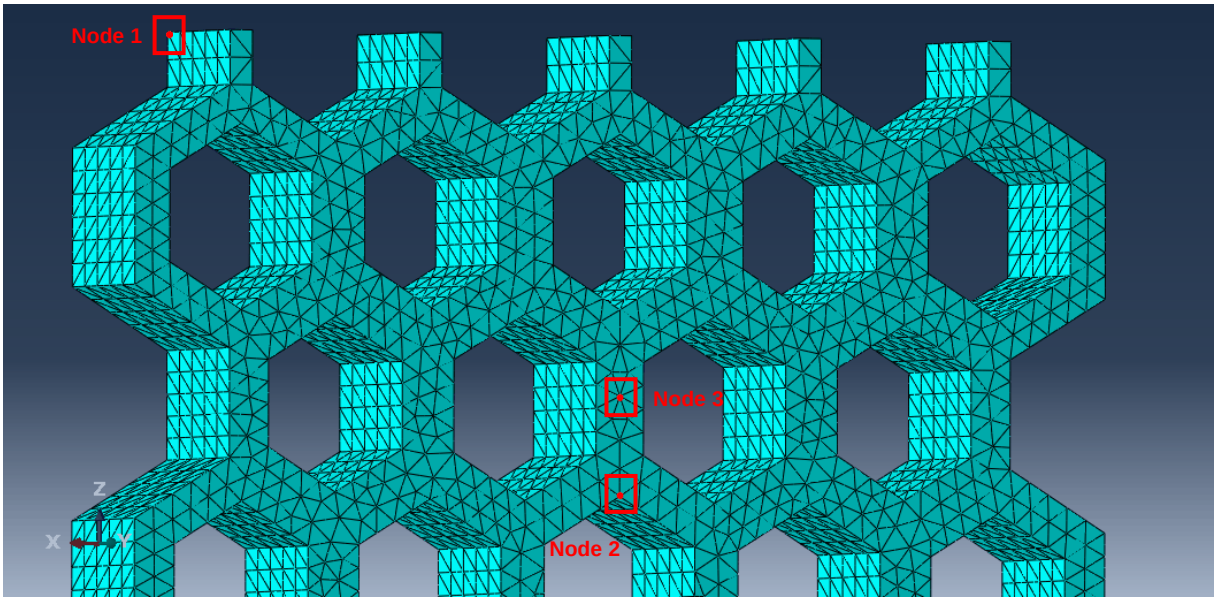

Figure C.1: Position of nodes in which the average von Mises stress was recorded in the convergence analyses.

As in the convergence analysis performed for the regular structure, the deviation of values was calculated via the calculation of the relative error, as seen in Equation C.1, in which $\bar{\sigma}_{M,i}$ is the average von Mises stress obtained in the mesh i, and $\bar{\sigma}_{M,i-1}$ the same but for the previous mesh.

$$Error\ (\%) = \left| \frac{\bar{\sigma}_{M,i} - \bar{\sigma}_{M,i-1}}{\bar{\sigma}_{M,i-1}} \right| \times 100 \qquad \text{(C.1)}$$

Tables C.1 and C.2 show the global size, number of elements and nodes, values for average von Mises stress and subsequent error for the various meshes recorded for the graded structure, with a maximum error set at 5%. Although the error values were kept relatively constant and below 5% in coarser meshes, a turning point was identified with global seed sizes of 1.5mm/1.6mm. Therefore, the analysis concluded that the most appropriate mesh, with acceptable convergence and error percentage, while keeping the simulation time at a reasonable duration would be the one designed with a global seed size of 1.4mm.

Table C.1: Parameters regarding the various meshes simulated for the convergence analysis (sample 2D)

Global seed size [mm]	Number of nodes	Number of elements	Simulation time [s]
3.0	29728	16747	1420
2.6	38632	22192	1262
2.4	48031	27932	1580
2.2	60582	35940	3739
2.0	73769	44145	2991
1.8	102552	62758	3354
1.6	143304	89778	8245
1.5	162691	102061	12000
1.4	208713	132588	13645
1.3	239558	152916	15570

Table C.2: Von Mises stress values and errors obtained regarding the various meshes in the convergence analysis (sample 2D)

Global seed size [mm]	von Mises Stress (Avg: 75%) [MPa]			Error [%]		
	Node 1	Node 2	Node 3	Node 1	Node 2	Node 3
3.0	530.146	342.012	226.084	---	---	---
2.6	527.110	352.594	214.318	0.57	3.09	5.20
2.4	529.770	344.216	228.620	0.50	2.38	6.67
2.2	534.25	353.295	212.134	0.85	2.64	7.21
2.0	522.423	342.722	211.578	2.21	2.99	0.26
1.8	523.652	301.424	209.627	0.24	12.05	0.92
1.6	497.704	328.249	195.776	4.96	8.90	6.61
1.5	459.277	335.015	205.436	7.72	2.06	4.93
1.4	469.107	333.416	203.966	2.14	0.48	0.72
1.3	473.902	341.541	201.559	1.02	2.44	1.18

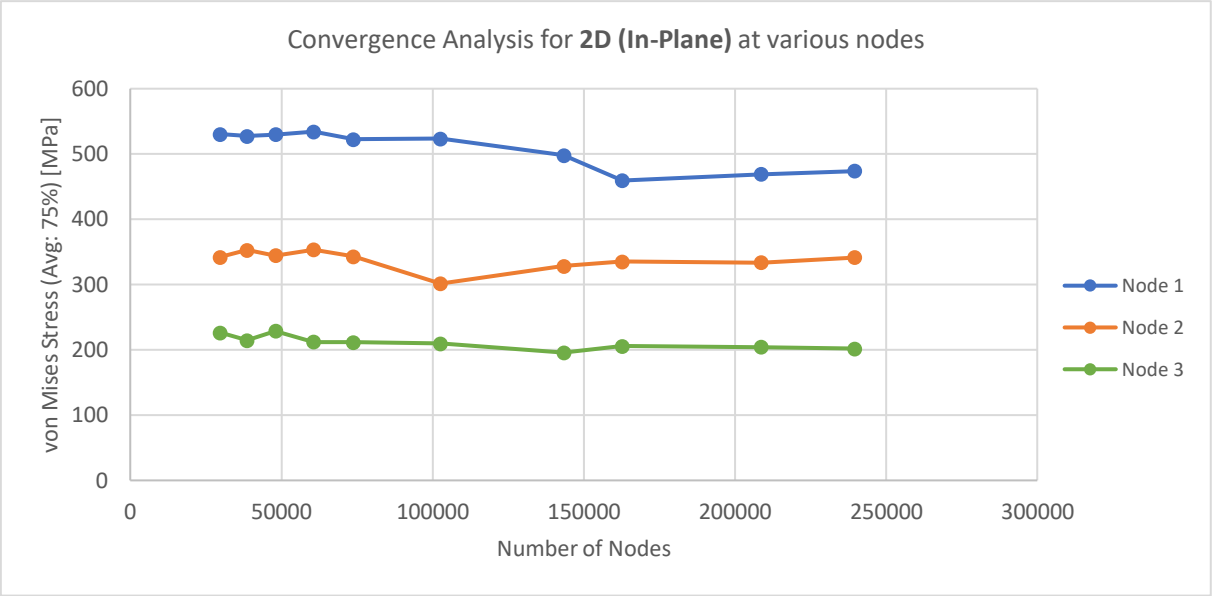

Figure C.2: Convergence analysis plot for sample 2d (In-Plane) at various nodes

Appendix D: Supplementary Results

The present appendix consists in additional plots and charts regarding the mechanical performance of both regular and graded structures.

D.1 Out-of-plane Testing

D.1.1 Regular Structures

Figure D.1 and D.2 presents the variation of the regular structures' specific energy absorption with relative density and apparent area, respectively, for both numerical elastic and elastoplastic scenarios.

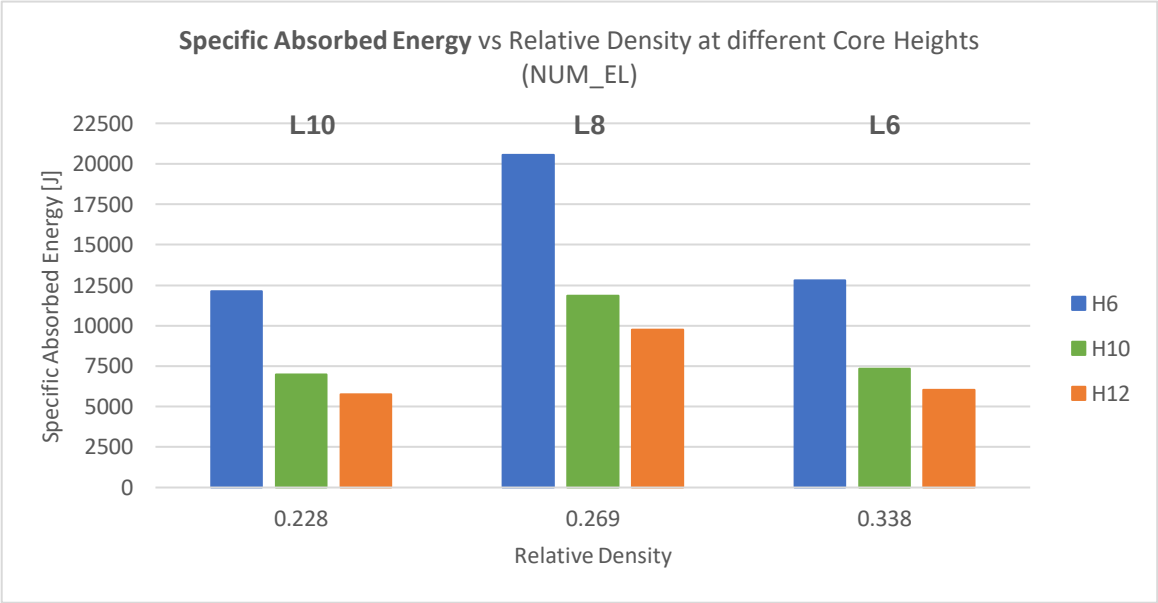

(a)

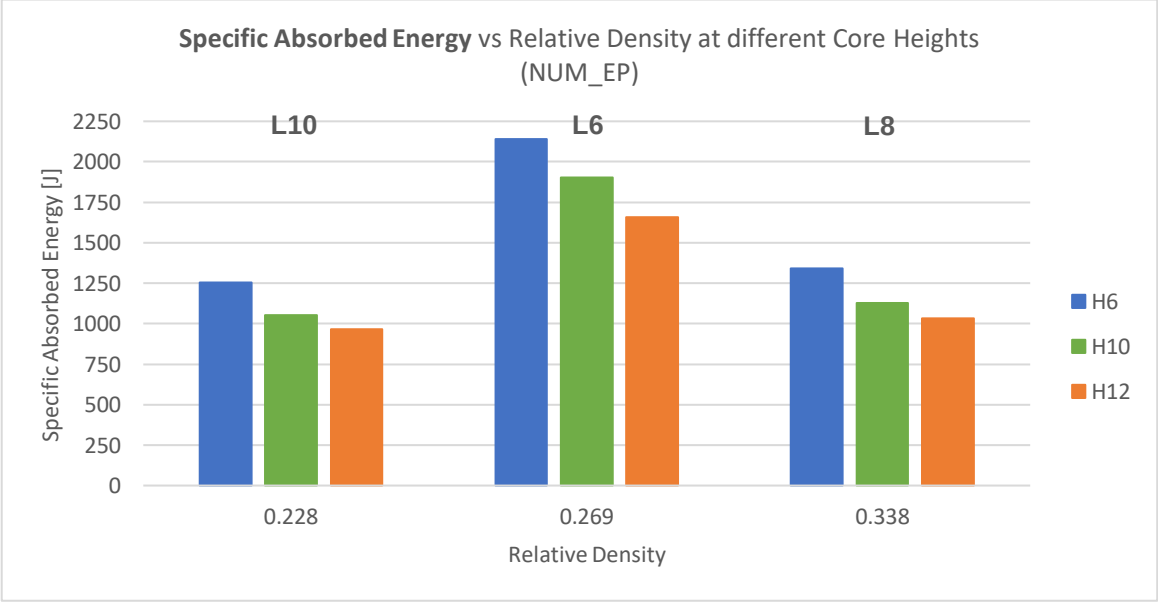

(b)

Figure D.1: Specific absorbed energy vs relative density at different cell core heights and length: (a) NUM_EL; (b) NUM_EP (Out-of-Plane)

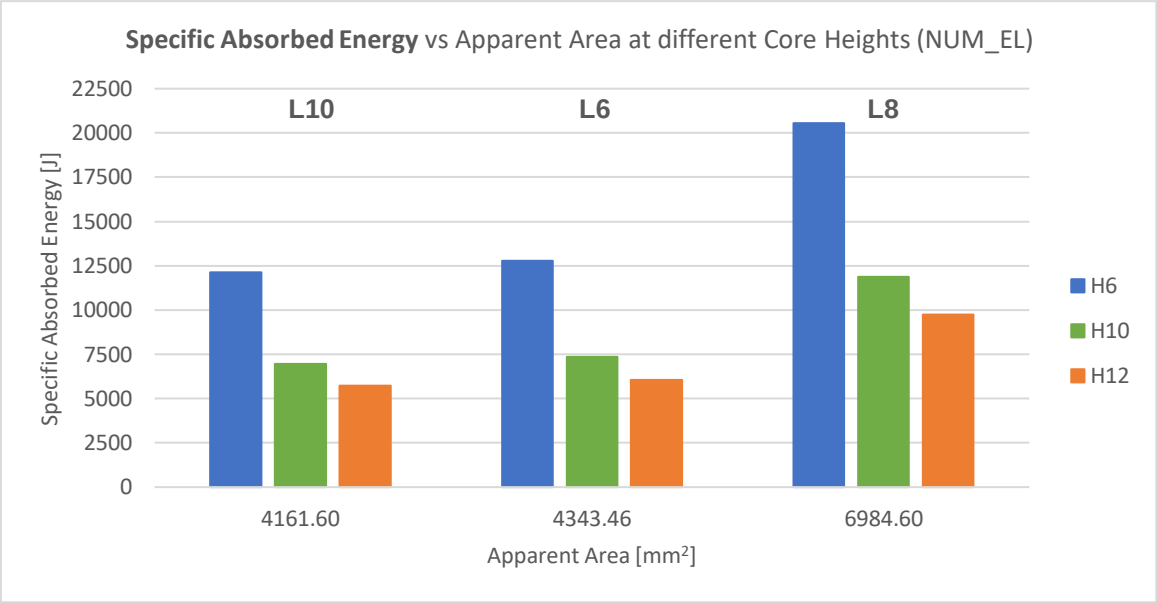

(a)

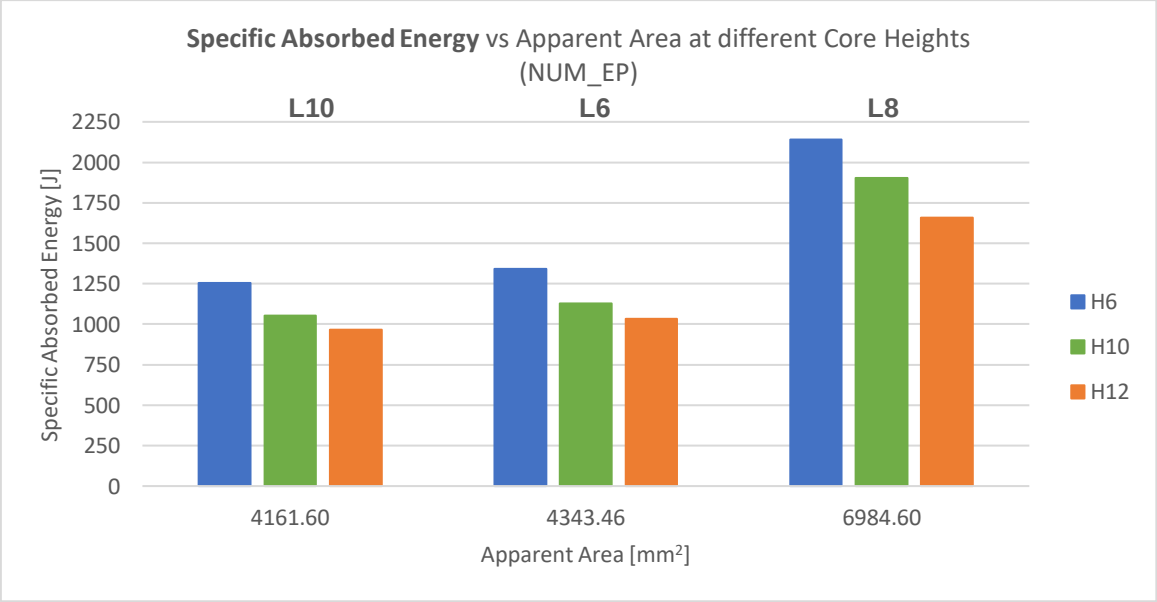

(b)

Figure D.2: Specific absorbed energy vs apparent area at different cell core heights and length: (a) NUM_EL; (b) NUM_EP (Out-of-Plane)

Figure D.3 shows the variation of specific stiffness with apparent area regarding the out-of-plane experimental testing of regular structures while Figure D.4 presents the variation of specific absorbed energy with relative density and apparent area ((a) and (b), respectively).

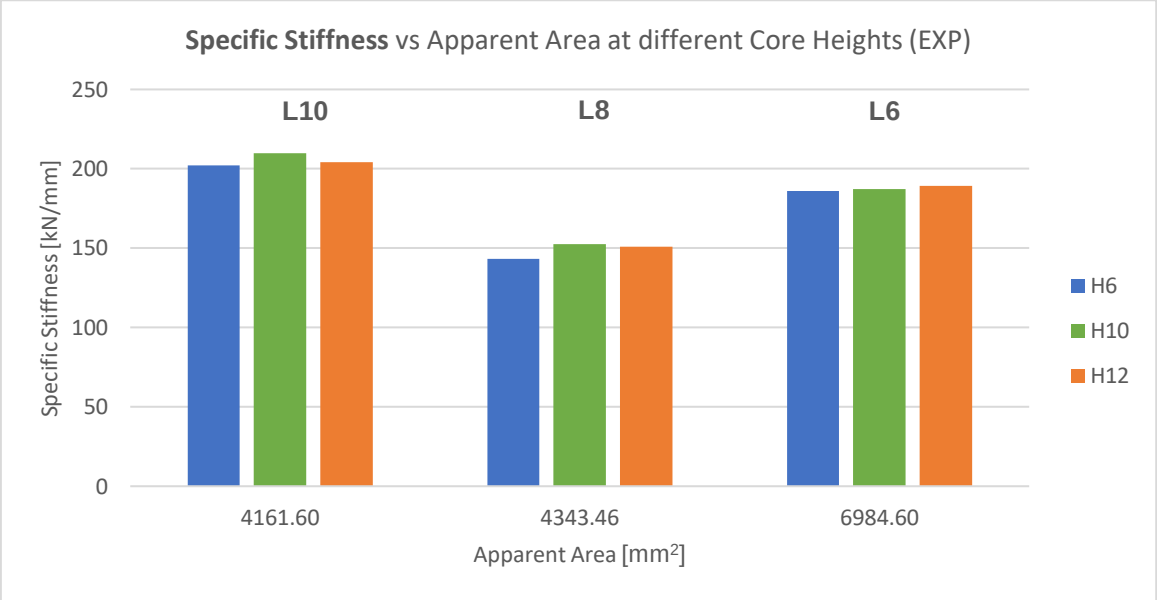

Figure D.3: Specific stiffness vs apparent area at different cell core heights and lengths (out-of-plane EXP)

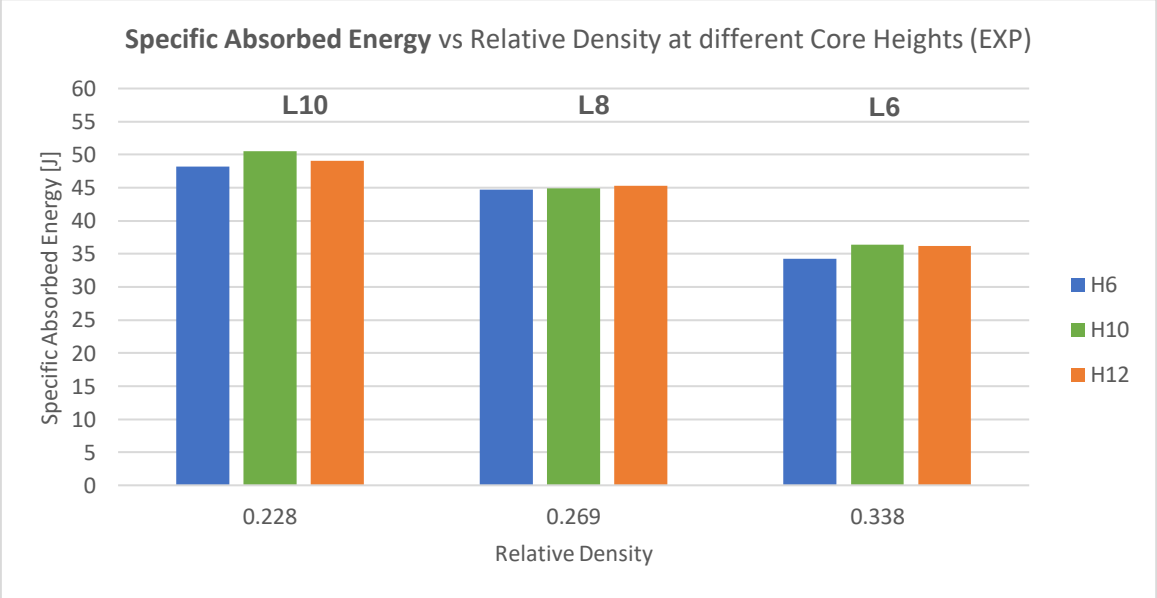

(a)

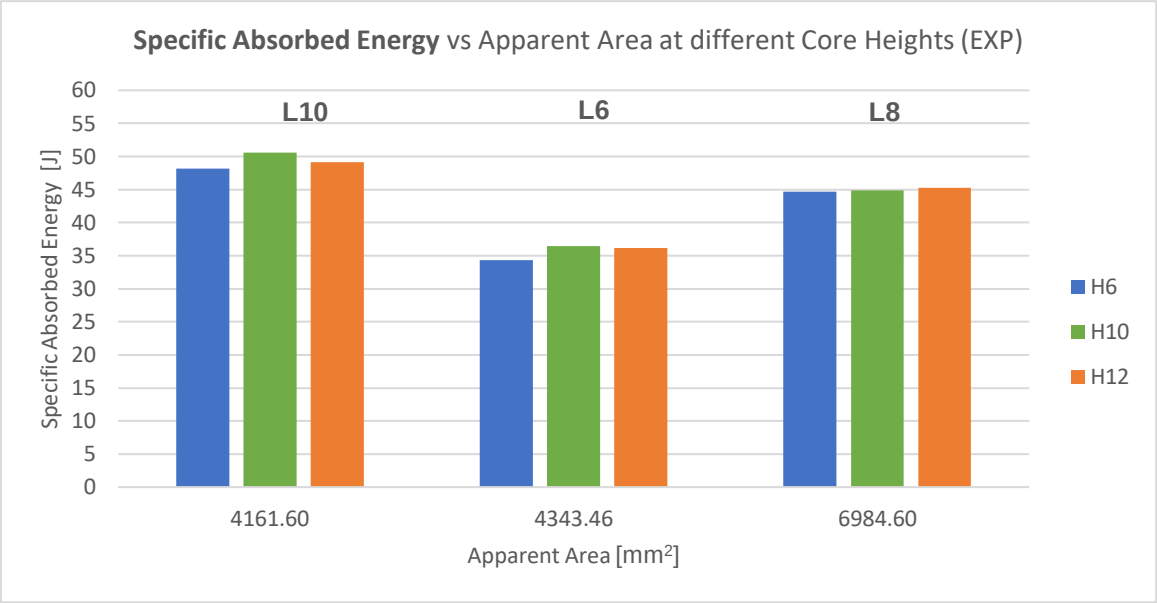

(b)

Figure D.4: Specific absorbed energy vs relative density (a) and apparent area (b) at different cell core heights and length (out-of-plane EXP).

D.1.2 Graded Structures

Figure D.5 displays the numerical force-displacement curves referring to the in-plane simulations regarding the graded structures, with grouping regarding the gradient type.

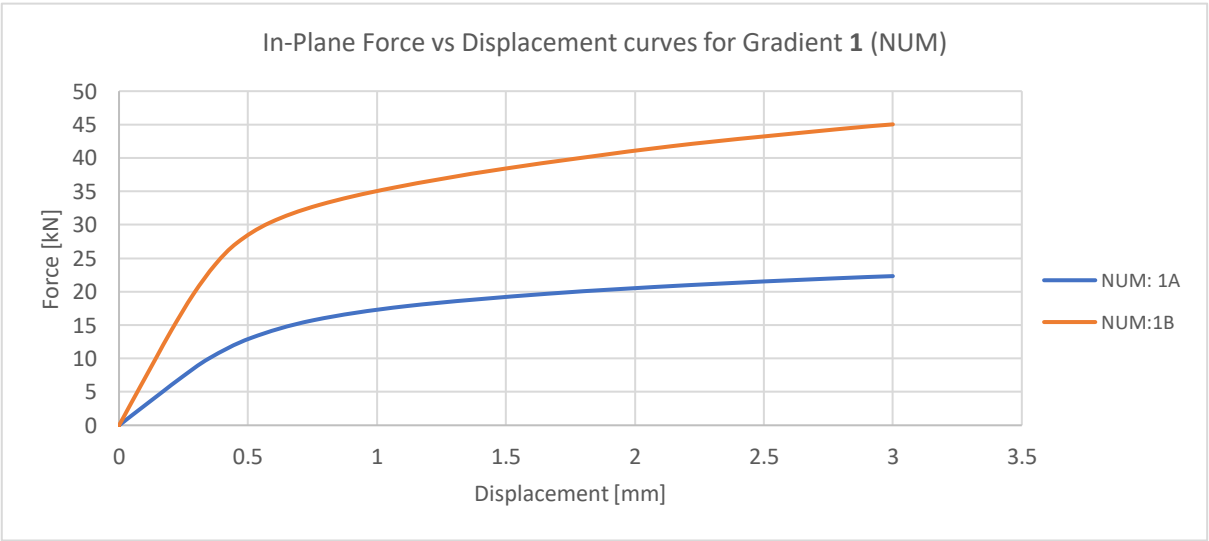

(a)

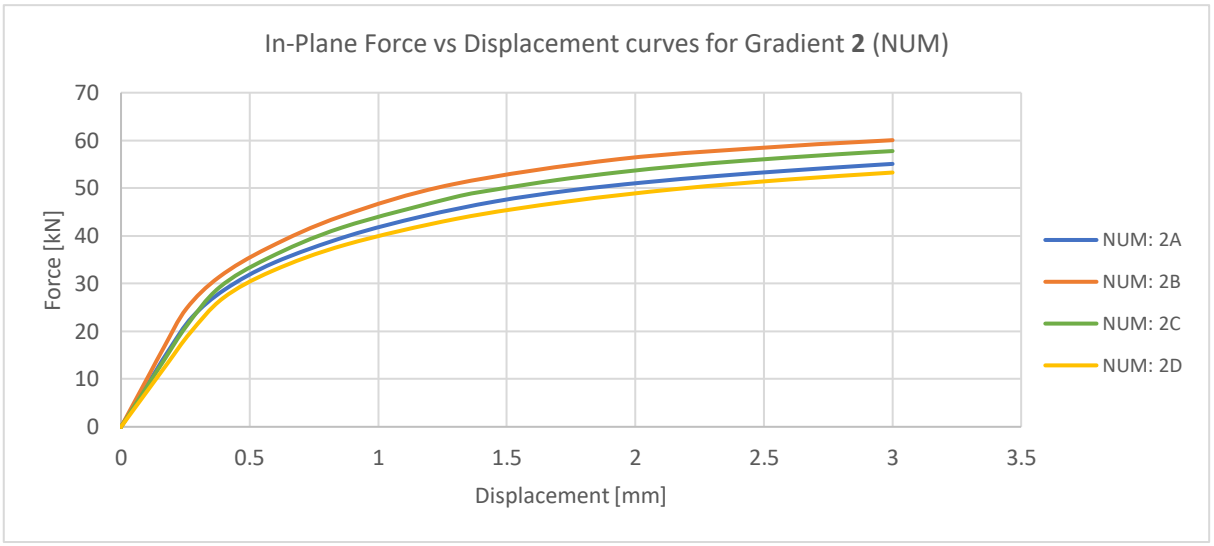

(b)

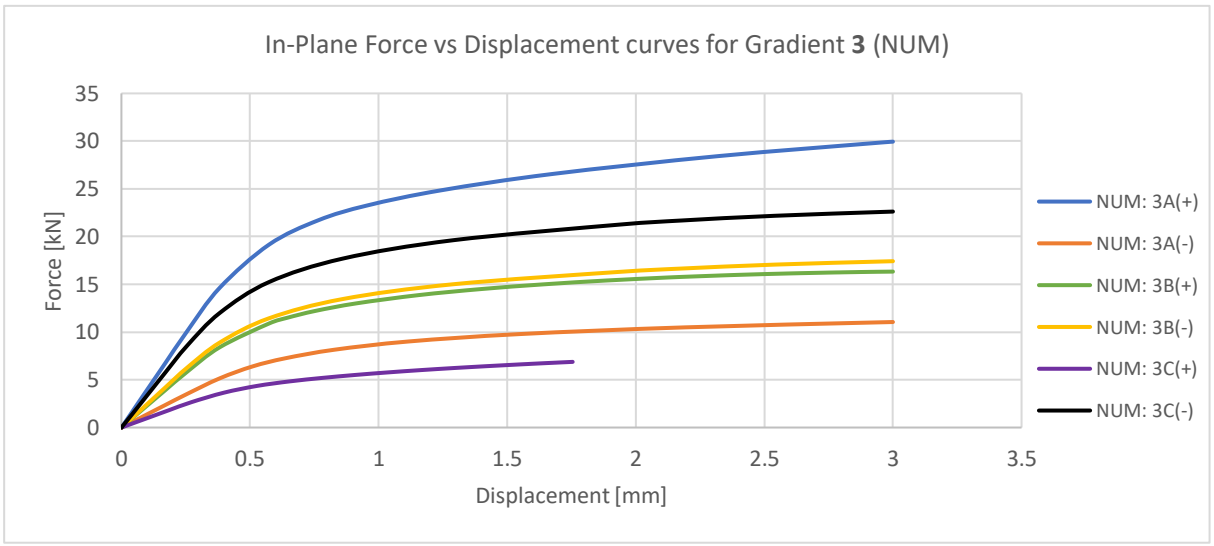

(c)

Figure D.5: In-plane force-displacement curves for structures of different gradient type: (a) Gradient 1; (b) Gradient 2; (c) Gradient 3.